



Master's Thesis in Informatics: Games Engineering

# Evaluation of Rendering Optimizations for Virtual Reality Applications in Vulkan

**Paul Preißner**





Master's Thesis in Informatics: Games Engineering

## **Evaluation of Rendering Optimizations for Virtual Reality Applications in Vulkan**

## **Evaluation von Renderoptimierungen für Virtual Reality Anwendungen in Vulkan**

Author: Paul Preißner  
Supervisor: Prof. Gudrun Klinker, Ph.D.  
Advisor: M.Sc. Sven Liedtke  
Submission Date: February 15 2020



I confirm that this master's thesis in informatics: games engineering is my own work and I have documented all sources and material used.

Garching bei München, February 15 2020

Paul Preißner

## Acknowledgments

My gratitude is expressed towards TUM and its teaching staff for providing an invaluable learning and working environment, towards my fellow students for great memories and towards Mio Mio and Spezi for keeping me glycemic in trying times.

# **Abstract**

Virtual reality (VR) and modern low-level graphics APIs, such as Vulkan, are hot topics in the field of high performance real-time graphics. Especially enterprise VR applications show the need for fast and highly optimized rendering of complex industrial scenes with very high object counts. However, solutions often need to be custom-tailored and the use of middleware is not always an option. Optimizing a Vulkan graphics renderer for high performance VR applications is a significant task. This thesis researches and presents a number of suitable optimization approaches. The goal is to integrate them into an existing renderer intended for enterprise usage, benchmark the respective performance impact in detail and evaluate those results. This thesis likewise includes all research and development documentation of the project, an explanation of successes and failures during the project and finally an outlook on how the findings may be used further.

# **Kurzfassung**

Sowohl Virtual Reality als auch low-level Grafikschnittstellen wie Vulkan sind stark gefragte Themen im Bereich der Echtzeitgrafik. Die Darstellung komplexer und hoch detaillierter Szenen ist besonders im industriellen Umfeld für VR Applikationen eine Grundvoraussetzung. Oftmals werden allerdings spezifisch zugeschnittene Lösungen benötigt, wenn vorgefertigte verfügbare Tools keine Option sind. Daher ist die Optimierung eines Vulkan Grafikrenderers für High Performance VR Anwendungen eine Kernaufgabe. Diese Arbeit untersucht und präsentiert demnach eine Anzahl an passenden Optimierungswegen. Teil des Ziels ist es, eine Auswahl dieser in einen vorhandenen Renderer aus dem industriellen Umfeld zu integrieren, die jeweilige Performance zu im Detail zu messen und auszuwerten. Diese Arbeit beinhaltet ebenso jegliche Forschungs- und Entwicklungsdokumentation des praktischen Projekts und gibt eine Erläuterung der Erfolge und Misserfolge und einen Ausblick darauf, wie die Ergebnisse womöglich einsetzbar sind.

# Contents

<b>Acknowledgments</b>	iii
<b>Abstract</b>	iv
<b>Kurzfassung</b>	v
<b>1 Introduction</b>	1
1.1 The goal . . . . .	2
1.2 Industry collaboration . . . . .	3
1.3 Technical foundation . . . . .	3
<b>2 The RTG Echtzeitgraphik GmbH Tachyon Engine</b>	4
2.1 Render setup . . . . .	4
2.2 Render loop . . . . .	5
2.2.1 VR render loop . . . . .	6
<b>3 Stereo Rendering Optimization - Input reduction</b>	8
3.1 (Hierarchical) Frustum culling . . . . .	8
3.2 Frustum (& distance) culling in Tachyon . . . . .	8
3.3 Superfrustum Culling . . . . .	10
3.3.1 Estimated impact . . . . .	12
3.3.2 Implementation specifics . . . . .	13
3.4 Round Robin Culling . . . . .	14
3.5 Conical Frustum Culling . . . . .	15
3.6 Merging approaches . . . . .	15
<b>4 Stereo Rendering Optimization - Effort reduction</b>	17
4.1 Multiview stereo rendering . . . . .	17
4.1.1 Estimated impact . . . . .	20
4.1.2 Implementation specifics . . . . .	20
4.2 HMD Stencil Mask . . . . .	21
4.2.1 Estimated impact . . . . .	21
4.2.2 Implementation specifics . . . . .	22
4.3 Monoscopic Far-Field Rendering . . . . .	24
4.3.1 Estimated impact . . . . .	26
4.3.2 Far-first approach . . . . .	27
4.3.3 Near-first approach . . . . .	28

4.3.4	Implementation specifics . . . . .	28
4.3.5	rtvklip MFFR failure . . . . .	30
4.3.6	MFFR Variant: Depth Shift . . . . .	31
4.3.7	MFFR Variant: Alternate eye . . . . .	32
4.4	Foveated Rendering . . . . .	32
4.4.1	Fixed versus True Foveated Rendering . . . . .	33
4.4.2	Radial Density Mask . . . . .	33
4.4.3	Relevancy of GPU architecture . . . . .	35
<b>5</b>	<b>Performance testing setup</b>	<b>37</b>
5.1	Benchmark scene . . . . .	37
5.2	Timing code & metrics . . . . .	38
5.3	Compilation parameters . . . . .	39
5.4	System specifications . . . . .	40
<b>6</b>	<b>Performance benchmark results</b>	<b>42</b>
6.1	Individual impact . . . . .	44
6.1.1	Comparison of individual optimizations . . . . .	48
6.2	Combined impact . . . . .	52
6.2.1	Comparison of combined optimizations . . . . .	54
6.3	Viable Combinations Comparison . . . . .	59
6.4	Memory Usage . . . . .	60
<b>7</b>	<b>Outlook</b>	<b>62</b>
<b>List of Figures</b>		<b>63</b>
<b>List of Tables</b>		<b>65</b>
<b>Glossary</b>		<b>66</b>
<b>Bibliography</b>		<b>67</b>

# 1 Introduction

Real-time rendering is not a new research topic. Naturally, developers and researchers have devised shortcuts and optimizations in hardware and software since the first applications in video games, visualization and simulation. There are methods and algorithms for almost any type of hardware, rendering technique and application scope. One more recently resurged trend is VR. The realization of affordable, comfortable and hassle-free VR headsets like the Oculus Rift series, the HTC Vive, Windows Mixed Reality design or the recently launched Valve Index led to a newfound vigor for the technology among consumers. Similarly, businesses as well as scientists are increasingly looking to VR for various fields of research, marketing opportunities and engineering support and more.

However, VR poses challenges and requirements not commonly seen with traditional real-time applications on monoscopic screens. While goals such as stable motion tracking, low latency and high performance rendering are as old as early VR HMDs, this recent resurgence has prompted more active search for possible solutions. Among these requirements is the need for high framerates to give the user a feeling of increased visual fluidity and to avoid motion sickness. VR applications not only need to render at a high framerate, they also need to do so at higher resolutions than common flat screens since the shorter viewing distance and added lens distortion means pixels appear larger to the user. The only way to combat resulting visual aliasing and the so called SDE is to significantly increase pixel count and density.

Similarly to Quílez' opening example in *Efficient Stereo and VR Rendering*[Íñi17], let us assume a traditional console video game running at Full HD resolution and 60 frames per second, which is a common for 8th generation consoles. Meanwhile, the same game running in a VR headset may require resolutions and framerate ranging from 1200 pixels per axis per eye (Figure 1.1) at 90 frames per second for entry level headsets and up to or even exceeding 2000 pixels per axis per eye at 120 frames per second for high end devices like the Pimax 4K. Image warp will commonly require an even higher internal rendering resolution by a factor of around 20% or more. For the entry level headset, this means a resolution increase of roughly 1.6x and a framerate increase of 1.5x for a combined 2.4x power requirement compared to the console baseline, while in the high end case it is roughly a 4.6x resolution and 4x framerate uptick for a combined 9.2x power requirement in comparison.

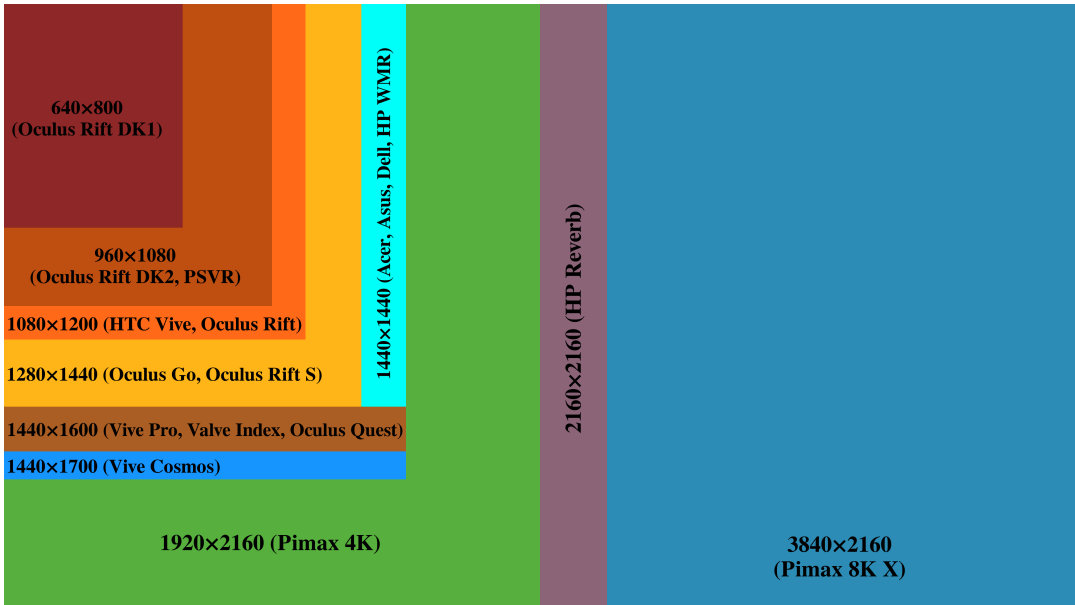


Figure 1.1: Comparison of common HMD resolutions (from [Vei19], V. Mäkelä. 2019)

## 1.1 The goal

While this is very rough napkin math and real applications scale differently due to a multitude of factors, it paints a clear picture: real-time VR rendering necessitates vastly faster rendering than traditional screens. Consequentially, VR rendering should take advantage of as much optimization as possible to attain that goal. There are many established options known to improve performance for various application types, with some of these options being de-facto standard features in popular rendering engines. However, there are a range of optimizations specific to VR or more generally stereoscopic rendering. There is less research and documentation available as of now, due in part to the aforementioned recent rise in popularity and prior lack of interest.

Thus, this paper aims to collect several VR optimizations, implement a subset of them in a real engine and subsequently benchmark and analyse the impact each has on performance. The goal is to have a better collection and understanding of the various possible methods and how much effort may be warranted for each. Firstly an explanation of the software and technical foundation used to implement practical samples is given, following this, optimizations aiming to reduce render *input* will be shown, succeeded by a chapter on optimizations aiming to reduce render *effort*. Finally, an analysis of the performance impact of each implemented approach. For the practical aspect of this thesis, the goal is to enable fast rendering of complex scenes with very large object counts, all while driving VR headsets at high resolution and framerate.

## 1.2 Industry collaboration

This thesis is created in collaboration with RTG Echtzeitgraphik GmbH, an engineering and consulting office based in Garching bei München. RTG Echtzeitgraphik GmbH offers engineering services related to real-time visualization, VR applications and hardware prototyping to enterprise clients from a variety of industry branches such as automotive and industrial logistics[Vol20].

The author of this thesis was employed at RTG Echtzeitgraphik GmbH at the time of writing. This allowed the use of company assets like workstations, a range of VR headsets and relevant literature as well as expertise with regard to related technologies and enterprise requirements for a rendering engine. The thesis, accompanied research efforts and all material created for the purpose of this thesis, however, are the author's own work.



RTG Echtzeitgraphik  
GmbH

## 1.3 Technical foundation

In an effort to represent a realistic use case, an engine with actual production usage target was chosen as opposed to a purely synthetic test vehicle, namely RTG Echtzeitgraphik GmbH's own Tachyon. The engine and its structure is further explained in chapter 2.

The graphics API and library of choice for this thesis then is the Khronos Group's Vulkan. Vulkan is a low level graphics API officially created in 2014 and formally released in early 2016. It promises increased flexibility and reduced overhead compared to prior graphics APIs as well as compatibility with a wide range of hardware architectures and operating systems[The16]. On the flipside, the verbose and low level nature of the API brings increased development effort and means that these promised improvements can only be leveraged with sufficient care and caution by developers.

For the practical goal of this thesis Vulkan promises a good fit. Furthermore, Vulkan is seeing a steady growth in developer interest and industry adoption. But with documentation, resources and API-specific research still being lackluster. This thesis hopes to add useful insights to this pool.

Lastly both Vulkan and the VR optimizations presented here are not just compatible with powerful x86 desktop machines but also with many ARM-based SoCs running Google's Android as well as Apple's iOS, promising prospects for the category of standalone low power VR headsets which are seeing increasing popularity[Ant18][20].

## 2 The RTG Echtzeitgraphik GmbH Tachyon Engine

Rendering optimizations can only be implemented if there actually is a renderer at hand. In order to see how the chosen approaches would perform in an engine intended for productive use and industrial applications, rather than an ad hoc renderer only built for some specific tests, Tachyon (working title) was chosen. Tachyon uses a fully Vulkan based forward renderer (internally rtvklip) with support for multiple viewports of various types, including an OpenVR-based VR path, an optional physically-based shader pipeline, a user interface module, a network module and a physics module with more extensions on the development schedule. The renderer integrates Vulkan version 1.1.85 and up and OpenVR version 1.4.18 and up with support for all major SteamVR headsets at the time of writing, including roomscale tracking of the Valve Index, HTC Vive and Vive Pro, the Windows Mixed Reality series and Oculus Rift series.

### Tachyon asset data types

To speed up asset load primarily for large 3D models or complex instance hierarchies, the engine at the time of writing only supports a custom in-house file format `*.hvr`. This file format is engineered to contain per-processed data arrays that can be directly imported to Tachyon as a single sequential block and require only minimal processing within the engine before startup. Essentially, instead of saving an object or objects and their hierarchies, material information and other resources as flexible and compatible formats such as FBX or OBJ, RTG Echtzeitgraphik GmbH opt to export to the HVR format using in-house exporter plugins. Textures can be imported from a variety of common file formats like PNG, TIFF, Targa or JPEG as the engine uses the third-party OpenImageIO [Gri19] library.

### 2.1 Render setup

As typical for the verbose nature of Vulkan, render initialization starts with the creation of all necessary basic Vulkan resources such as descriptors, descriptor sets, activation of a minimal set of Vulkan extensions and layers and device enumeration. More specific to rtvklip, multiple Vulkan pipelines are active by default:

- a material pipeline offering support for a Phong and a PBR shader as well as geometry and index buffers of arbitrary size
- a skybox pipeline with a simplified skybox shader

- a point cloud pipeline, primarily to allow rendering of LiDAR scan data

To facilitate rendering into multiple viewports, Tachyon uses the concept of render targets. Each render target can reference an arbitrary subset of pipelines and comes with its own set of Vulkan framebuffers, command buffers and render pass and its own virtual camera. Whenever any 3D object is to be loaded, `rtvklip` uses several manager classes to keep track of the various resource types needed for an object. There are managers for geometry, materials, textures and instances among other types. When an object is loaded, the former three hold the respective buffers. When an object is to be rendered, it first needs to be instanced, handled by the latter. An instance references the various geometry and materials of the original object again, but also holds data specific to individual objects in the virtual world, such as transforms or bounding geometry.

The renderer initialization also encompasses VR through OpenVR. Given a valid OpenVR environment and HMD is detected, a special render target is created with a Vulkan renderpass for multiple views and the respective resources. Resources include a framebuffer with one layer for each eye, created with the rendering resolution returned by OpenVR after querying `IVRSystem::GetRecommendedRenderTargetSize()` and using 4x multisampling as is often recommended for VR applications to minimize aliasing without obscene cost (see for example [Vla15] p. 25f, [Por17], [Car16], [18a], [Pet17]).

All run-time relevant vector and matrix math in the renderer and the presented optimization implementations use the free MPL2 licenses Eigen 3.3 math library. Eigen was chosen for its extensive feature set and its special focus on high performance using SIMD vectorization including all current forms of SSE and AVX among others[GJ+10].

## 2.2 Render loop

After all startup and initialization is done, the engine's render loop executes `VKRenderer`'s `Update()` and `RenderFrame()` functions back to back. The flows of these are shown in Figure 2.1 and Figure 2.2, respectively.

`VKRenderer::Update()` first prompts all aforementioned managers to update their databases, buffers and anything else they hold in case they are *dirty*. Then it prompts each render target to update, which may involve camera transformation updates and buffer synchronization, for example. For each render target, the loop will then have the instance manager perform a frustum culling pass, which will for this target save a conservative list of draw call information for objects visible by this target's camera viewpoints. If any of these updates and culling passes set a pipeline or command buffer state invalid, these will be rebuilt accordingly.

`VKRenderer::RenderFrame()` prompts each render target to perform its per-frame rendering operations, be it regular monoscopic output for a traditional viewport or pose tracking and stereoscopic composition for a VR target.

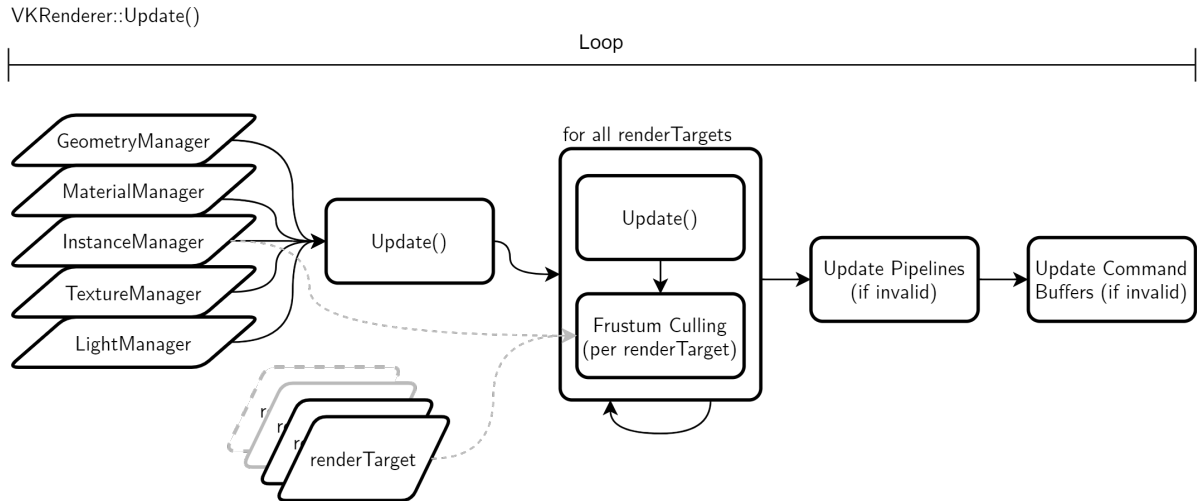


Figure 2.1: Renderer Update function

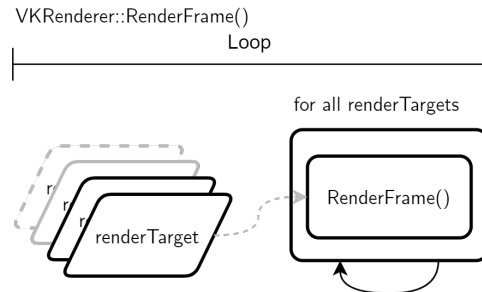


Figure 2.2: Renderer frame render function

### 2.2.1 VR render loop

The VR render target's `RenderFrame()` function is rather straight-forward. As long as the target and compositor are active, it updates the OpenVR device poses and virtual camera transforms. It then renders the stereoscopic views, resolves the multisampling layers into single sample and finally submits both eyes' images to SteamVR, which serves as the chosen OpenVR compatible compositor on Windows systems. Note here, `rtvklib`'s internal VR render target class is also called `OpenVR` unfortunately but is not equivalent to the external OpenVR library. Which of the two is meant in a given sentence is indicated by the formatting as showcased here.

As the VR view essentially moves constantly, its render target needs to update its Vulkan `VkCommandBuffer` every frame. This is done by setting the `mCommandBuffersInvalid` flag which has the renderer call `UpdateCommandBuffers()` which in turn prompts each render target to `RecordCommandBuffers()`. For each of the VR render target's command buffers this is a simple loop through the `RecordDrawCommand()`s of the pipelines assigned to this render target between the Begin and End commands of the command buffer and render pass. The draw com-

mand recording function has the respective pipeline query the `InstanceManager` for its post-culling draw command set and writes the contained entries as `vkCmdDrawIndexedIndirect()` draw calls.

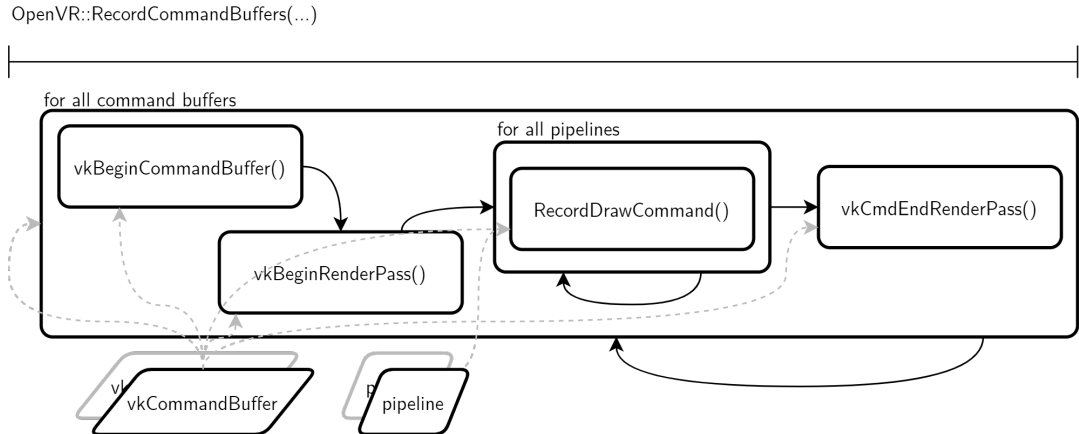


Figure 2.3: VR command buffer recording function

Moreover, as seen in Figure 2.4, the VR render target's `OpenVR::RenderFrame()` render function first updates the API-supplied HMD pose matrices and consequently recalculates its virtual camera parameters. It then submits any given `VkCommandBuffers` assigned to itself, followed by a submission of the multisample resolve command buffer. At the end of the loop iteration it gathers the resulting resolved image textures for each eye and submits them to the VR compositor for presentation inside the headset.

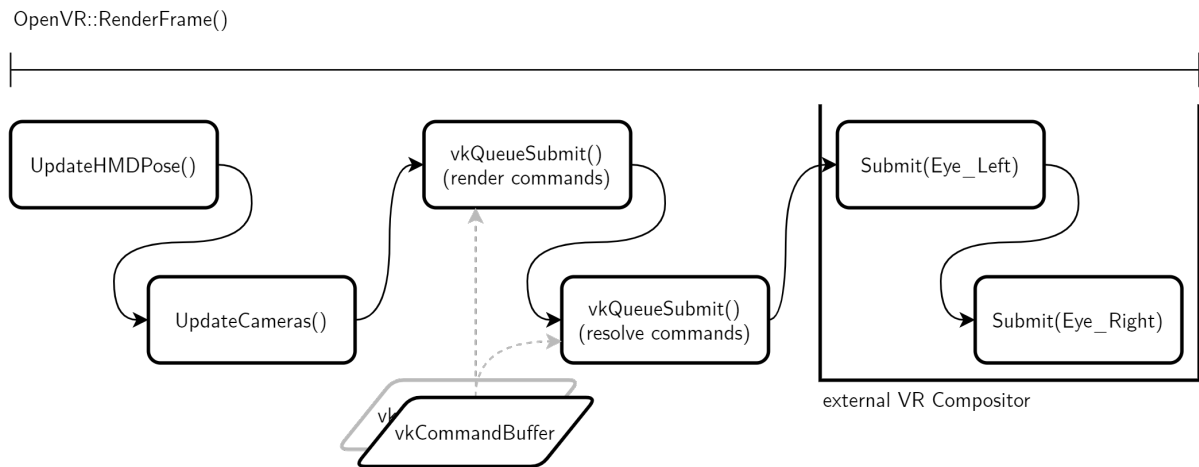


Figure 2.4: VR frame render function

# 3 Stereo Rendering Optimization - Input reduction

When looking at real-time rendering as it is done today - albeit from a strongly simplified perspective - the CPU could be described as an employer and the GPU as an employee. For each frame, the CPU produces certain render tasks and supplies the necessary information such as draw calls, shader parameters, buffers and so forth. The GPU then consumes these tasks and associated items and does the computational brunt to produce the required results. If one wants to speed up this process, there are two major ways. One is to reduce the amount of data put into the pipeline so less data needs to be processed overall, the other way is to increase the efficiency of the processing itself. This first chapter of optimization approaches presents ways of reducing the amount of data or work input. Note here that only a subset of the listed methods was implemented due to time constraints.

## 3.1 (Hierarchical) Frustum culling

The following options build on top of the regular frustum culling concept. In this, the objects in the scene are checked against a camera frustum whether they are inside or outside or intersecting with the surface of the frustum. The checks themselves can be generally optimized in various ways, regardless of stereoscopy. Often, only an object's bounding geometry is checked. Collections of objects can be pre-computed so larger numbers may be discarded at once. An advanced option of culling is to delegate the calculations into a GPU compute shader so potentially less data needs to be transferred from the CPU per frame and much higher vector/matrix calculation is gained in exchange for slower branching. Some modern renderers also do very granular culling like bitmasked checks of precomputed triangle sets, as seen in Ubisoft's Anvil Next engine used in *Assassin's Creed: Origins*[HA15]. Another optional layer of the culling process is to maintain hierarchical container structures for the scene objects so larger numbers can be discarded or included early on. For all those options the goal is the same: to obtain the list or buffer of objects visible by the given camera frustum in the scene.

## 3.2 Frustum (& distance) culling in Tachyon

The frustum culling approach in Tachyon was developed specifically for this thesis as a requirement for Superfrustum culling (section 3.3) and as a sensible general optimization, is fully CPU-based and utilizes pre-computed hierarchical draw buffers. More specifically, at

startup the scene is divided into a coarse grid of `chunks` where each such `chunk` possesses an octree. Also at startup, a thread pool with the double the number of detected hardware threads is created. At asset load time, these octrees are populated with the loaded objects through optimistic size-aware insertion. Each cell of a tree then pre-computes a draw buffer containing a combined draw call for all objects associated with that cell. These buffers can be recomputed at any time, but the operation should be avoided at runtime as it incurs costly CPU to GPU transfers. In a culling pass, first all `chunks` within a certain draw distance radius of the camera are chosen, so there is an additional very primitive distance culling taking place. Then each `chunk` submits a culling call using its tree to the thread pool. Each such call works as follows:

```

pseudo SceneChunk::FrustumCull()
{
    out draw-calls[camfrusta.size];
    for all leftover octree cells
    {
        for all camera frusta
        {
            if cell is valid
                var checkResult = frustumCheck(frustum, cell);
                if checkResult == INSIDE
                {
                    add overall cell draw-call to draw-call list;
                } else if checkResult == INTERSECT
                {
                    add 8 child cells to leftover list;
                    add local cell draw-call to draw-call list;
                }
        }
    }

    for all camera frusta
    {
        unique_lock(cullMutex);
        sort and aggregate draw-call list;
        add draw-call list to per-pipeline draw-call collection;
    }
}

```

Figure 3.1: per scene chunk frustum culling procedure (shortened pseudo code)

In essence, the octree is looped through in a hierarchical fashion until either all remaining subcells of the current hierarchy level are outside of the frustum or no more subcells are left

to check. Any resulting draw-calls are sorted to be memory layout friendly and aggregated into as few calls as possible to reduce invocation cost.

However, one problematic area remains and that is Z ordering. Modern graphics pipelines will perform early Z discard during the fragment stage. If a fragment fails the depth test for a given draw call, meaning its geometry would be occluded by triangles already written to the fragment, the shader will skip any further calculation for this geometry and fragment. For this to take hold in performance improvement, the draw calls need to be issued in a manner where geometry closer to the camera is drawn first. If draws are done in reverse order, the pipeline will draw distant geometry first and subsequent closer geometry at the same fragment will naturally not fail the depth test and overwrite the fragment. Effectively, all prior writes to any such fragment in that frame would be wasted and go unseen. This issue is called overdraw and can significantly deteriorate GPU render times in extreme cases. One such example would be the following, very dense synthetic test scene:

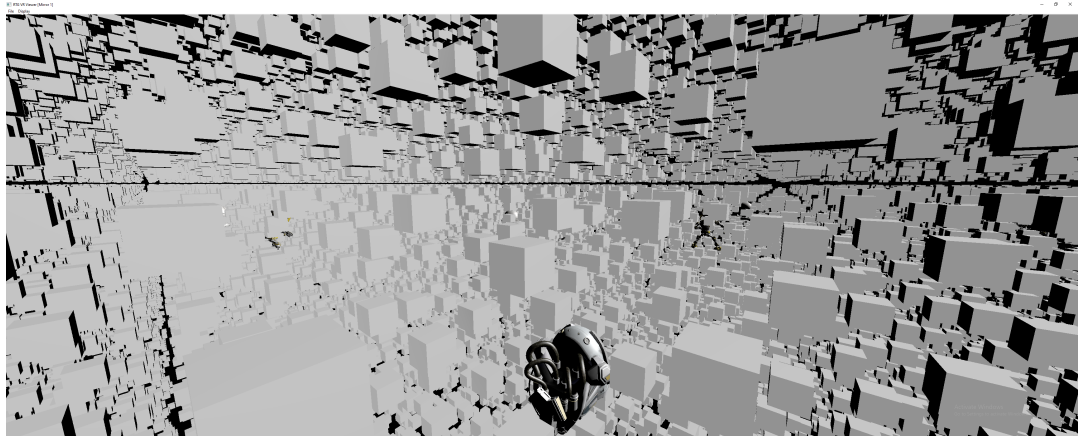


Figure 3.2: Sample scene with high object density, far draw distance and high degree of overdraw when rendered without per-frame Z ordering, screenshot taken of Tachyon's desktop viewport

If the draw calls for each populated octree cell are issued back to front, the overdraw of many dozens if not hundreds of layers can push frametimes upward to the point where the GPU is geometry-bottlenecked in the depth test, while issuing the calls front to back may result in sufficiently low frametimes. At this time, rtvklib does not employ such call reordering, meaning due to the nature of the octree cells' pre-recorded command buffers, overdraw cannot be avoided without a significant rewrite of these pre-recordings.

### 3.3 Superfrustum Culling

The basic idea behind so-called *Superfrustum Culling* is to do regular single frustum culling despite rendering into two cameras, one per eye. The naive way of extending the frustum

concept to a stereoscopic camera is to add a second frustum so there is one per eye, then perform the culling check for both frusta and merge the results.

As is easily visible from Figure 3.3, the spatial proximity of these two frusta leads to a large overlap volume, especially as field of view increases with more advanced headsets. One possible strategy to leverage more performance when culling two eyes is the Superfrustum, assuming the frustum is the common six sided trapezoid. Cass Everitt of Facebook Technologies LLC, formerly Oculus LLC, has suggested this approach and provided computation sketches on his social media back in 2015 [Eve15a](Figure 3.4), and Nick Whiting at Oculus Connect 4 teased it as a future addition to Unreal Engine 4 [Whi17]. The idea is to combine the left and right eye frusta by taking the respective widest outer FOV tangent - usually the left eye's right side and the right eye's left side - and using these as the new side tangents of the superfrustum. Another way to express these is to take the widest half opening angles of each eye and adding them up to a combined opening angle. Similar is done for the top and bottom tangents, although these will usually be nearly identical for the two eyes.

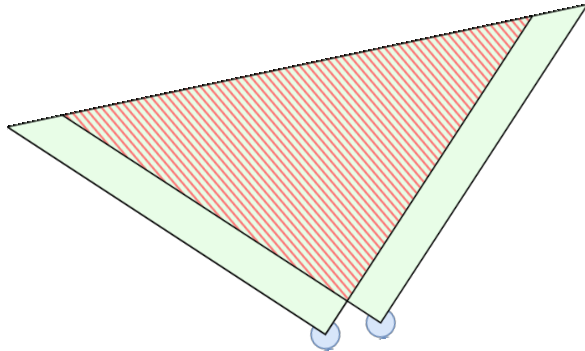


Figure 3.3: Overlap of stereo view frusta (overlap area hatched in red)

A pitfall of the superfrustum is its necessary depth recession. This is easy to visualize when combining the two frusta by extending aforementioned side tangents backwards until they cross. The meeting point of this step is the new origin of the superfrustum, slightly recessed behind the two separate eyes. Vivien Oddou of Silicon Studios offered a generalized way to compute this recession for non-mirrored eye orientation [Odd17](Figure 3.5), while Everitt has extended his sketches by an asymmetry normalization[Eve15b]. Both of these are important to consider as virtual reality headsets can have slightly canted and asymmetrical lenses, either by design or by manufacturing tolerance. Ignoring these two corrections may still result in a sufficient superfrustum if computed conservatively but should be included for fully correct setups. While this superfrustum naturally eliminates all overlap of the naive variant, it in turn includes small false positive regions, notably the triangular void found close to the origin points between the two eye frusta and potential side edge regions in the case of asymmetrical lens orientations. In a typical application, the performance cost of these is negligible.

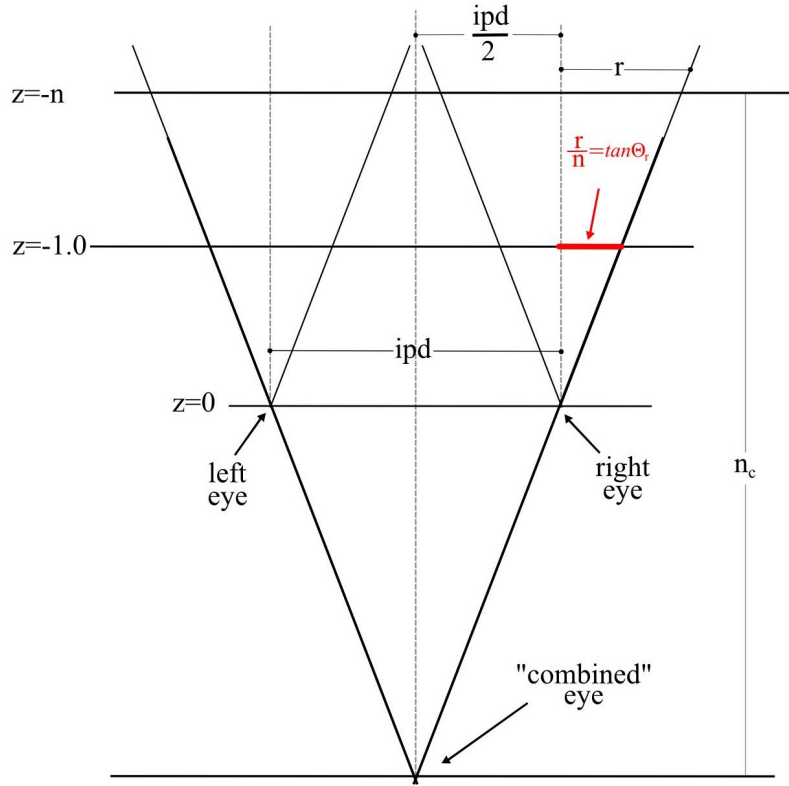


Figure 3.4: Symmetric Superfrustum (cropped to geometric construction) (from [Eve15a], C. Everitt. 2015)

### 3.3.1 Estimated impact

The impact of using a Superfrustum will depend on the type of frustum culling math done and the combination with other techniques.

On its own, with a CPU based culling pass, only an appreciable benefit in CPU rendering time is to be expected, as the number of frustum checks will be reduced by up to 50% and only a single buffer needs to be transferred to the graphics unit. The GPU itself still needs to render each eye separately, including all vertex transformations, pixel shading and so forth. The specific impact in the case of Tachyon is elaborated on in chapter 6.

Superfrustum culling when performed directly on the GPU obviously has great potential to significantly cut down on related compute work, once again to the effect of up to 50% versus a baseline dual frustum culling. An interesting point to consider is whether any of the culling data needs to be synchronized back to the CPU, as, when not, the GPU compute workload will only depend on a single small buffer or pushconstant transfer containing the camera parameters. If, however, the resulting culling set is transferred back to the CPU, for example for preprocessing of the next frame, this transfer will present another speedup limiter.

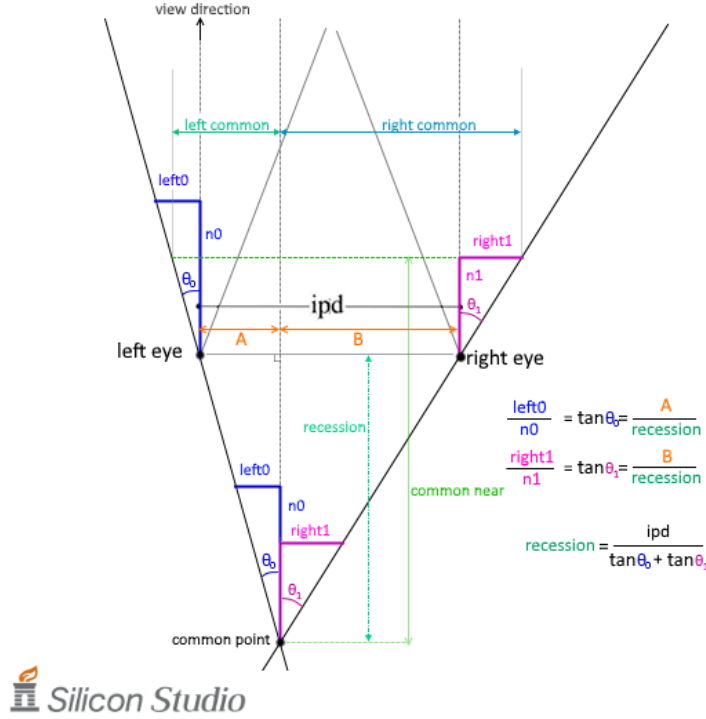


Figure 3.5: Non-mirrored superfrustum recession (from [Odd17], V. Oddou. 2017)

### 3.3.2 Implementation specifics

Facilitating Superfrustum Culling in Tachyon required only straight-forward changes. At creation time of the virtual camera, the superfrustum is computed from the given OpenVR eye parameters following Everitt and Oddou's way. Assuming the two eye projections are asymmetric, they need to be symmetricized. For this, after grabbing each eye's projection matrix from OpenVR for the desired near and far clip distances, the  $M[0][0]$  and  $M[0][2]$  values of each matrix are of interest. These two values represent the OpenGL clipping space's X coordinate's scalars. OpenVR through SteamVR uses the same coordinate layout. At a Z depth of -1, these two scalar terms are entirely dependent on center point and width of the projection cube. Solving them for center and width then gives  $center = \frac{M[0][2]}{M[0][0]}$  and  $width = \frac{2}{M[0][0]}$ . A new symmetric projection then obviously could be constructed from this center and width by taking the center point and stepping "sideways" by half width. The new *right*, or *r* value, for example, will be  $r_{sym} = abs(center) + \frac{width}{2}$ , which if substituted by the matrix dependent fractions comes out to  $abs(\frac{M[0][2]}{M[0][0]}) + \frac{1}{M[0][0]}$ . This can be solved for a new  $M_{sym}[0][0] = \frac{M[0][0]}{abs(M[0][2]) + 1}$  and  $M_{sym}[0][2] = 0$  (see [Eve15b]). In the next step, these new  $M_{sym}[0][0]$  values for both eyes are inserted into the recession math by Oddou[Odd17]. For non-mirrored and asymmetric eyes, a superfrustum recession is simply calculated as  $\frac{ipd}{\tan\theta_0 + \tan\theta_1}$  with  $\theta_i$  being the respective center-to-outside opening angle of each eye. Conveniently with

the previously calculated  $M_{sym}$  values, these tangents of angles are equal to the reciprocal of the respective  $M_{sym}[0][0]$ . As such for the recession we get  $\frac{ipd}{\frac{1}{M_{sym}[0][0]_l} + \frac{1}{M_{sym}[0][0]_r}}$ . The calculated superfrustum recession and new combined field of view angles are saved and used every frame when re-transforming the superfrustum. The frustum transformation uses a simple geometric approach where the camera's world position, forward and up vectors in conjunction with the near and far distance, field of view and aspect ratio are extruded into the six planes of the frustum volume. The per-frame culling pass of Tachyon then naturally only checks against this single frustum and returns a single set of draw commands which are sent to both eyes.

### 3.4 Round Robin Culling

Another culling variant specific to stereoscopy uses the round robin principle. Again, the concept springs from the desire to avoid frusta overlap but instead of combining the frusta, it exploits a common property of current stereoscopy rendering techniques. As modern headsets use circular lens optics and flat displays distorting the displayed image, the framebuffers commonly need to be warped to compensate so the picture looks undistorted to the user. As a result, a lot of the edge data of the image is either considerably pushed together or outside of the visible area of the HMD displays. This conservative property means a virtual eye frustum can be smaller than the technical frustum of that respective eye and false negative discards in these edge regions would go unseen by the user. Assuming both eyes of the headset have similar opening angles and parallel or nearly parallel viewing direction, the overlap of the two frusta would encompass the entire stereo-visible volume. It follows that only culling for one of the eye frusta would already give a sufficient representation of the actually visible scene.

There is still a possibility of missing a few edge cases with this alone. So the extension of the idea to actual round robin assumes another common property of modern VR headsets, namely high refresh rates. Many of these aim for at least 80Hz (Rift S, WMR) ranging up to 144Hz (Index experimental mode) image refresh to give the user a smooth visual sensation. Exactly halving that refresh rate and reprojecting images for two refresh cycles with some pixel interpolation is an established way to still provide an acceptable experience with minor visual artifacting on slower devices as demonstrated by Oculus LLC's Asynchronous Space Warp[BHP16] and SteamVR's reprojection[18b] features. Subsequently, a conceivable compromise is to alternate which frustum is used for culling in a round robin fashion so that even if edge cases include visible false negatives, they only persist for one frame at a time. In the worst case this would manifest as shimmering or flickering at the outer edges of the visible screen area.

Overall this makes Round Robin Culling a viable candidate on systems with very limited culling performance but the tight constraints for sufficiently accurate results make it unfit as a general recommendation.

### 3.5 Conical Frustum Culling

This third alternative culling extension targets the circular shape of HMD lenses for leverage. Coming back to the conservative framebuffer size from the previous section, the lenses lead to a lot of invisible area in the corners of the display. Jonathan Hale attempts to demonstrate the method in his thesis [Hal18] as both a contribution to the graphics middleware *Magnum*[Von19] and a UE4 extension at Vwhite Rabbit[Vhi20] - albeit with limited success. However, his proof of concept shows the validity of the method. The traditional six sided trapezoid frustum is replaced by a cone encompassing a volumetric projection of the view through each respective lens as visualized in Figure 3.6.

Hale examined various types of cone intersection math, including AABB and bounding sphere object checks against a spatially transformed frustum cone and the same checks for spatially inverse-transformed objects against an origin oriented frustum cone. While his results showed cone culling performing worse than traditional frustum culling, he notes optimization was not fully refined and all calculation was done on the CPU. Another note by Hale cautions that depending on the used HMD, a cone frustum may prove *less* accurate than a trapezoid, such as for the Oculus Rift CV1. As some headsets show not a fully circular image through their lenses but rather the entire distorted frame, it may not be possible to fit a cone frustum within the traditional frustum and instead that cone may actually exceed the traditional dimensions and thus cull fewer objects. For appropriate headsets and more geometry-bound GPUs, this method may provide a small relief if using even faster cone intersection math.

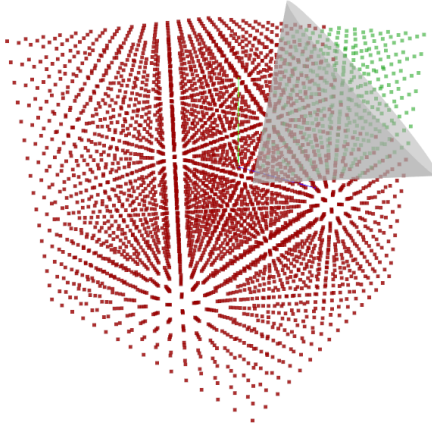


Figure 3.6: Point-cone intersection illustration by Hale (from [Hal18], p. 21, J. Hale. 2018)

### 3.6 Merging approaches

A convenient side effect of these three presented optimizations is that they can in part be merged. For example, it is possible to do Conical Round Robin Frustum Culling in an

effort to slice away as much of the conservative invisible area as possible and reduce the list of drawable objects to an optimistic minimum. It is also possible to construct a Conical Superfrustum aiming to avoid the mentioned edge false positives, albeit only feasible if the display per eye is square-like to avoid adding new false positive volume on other sides.

# 4 Stereo Rendering Optimization - Effort reduction

The following chapter of optimization approaches targets the efficiency of rendering processes on the graphics chip itself. These approaches have little to no impact on CPU performance and tend to exploit and scale mostly with GPU power. Note again that only a subset of the listed methods was implemented due to time constraints.

## 4.1 Multiview stereo rendering

When rendering a stereo image using the naive method of simply going through the entire rendering pipeline once for each viewport, potentially a lot of computation is done twice with little or no change in data or parameters. With the general graphics pipeline (Figure 4.1) in mind, it is clear that for example the vertex stage will see very little change in output as geometry and index buffers are largely the same between multiple stereo viewport passes with only minor shifts in the view matrices. Similarly, the geometry stage is commonly not dependent on specific eye data and as such it would be a waste to process with the same data twice. Once the rasterizer stage of the pipeline is reached, the situation changes as stereo separation means the two images have notably different content and work from one can not realistically be recycled in the other.

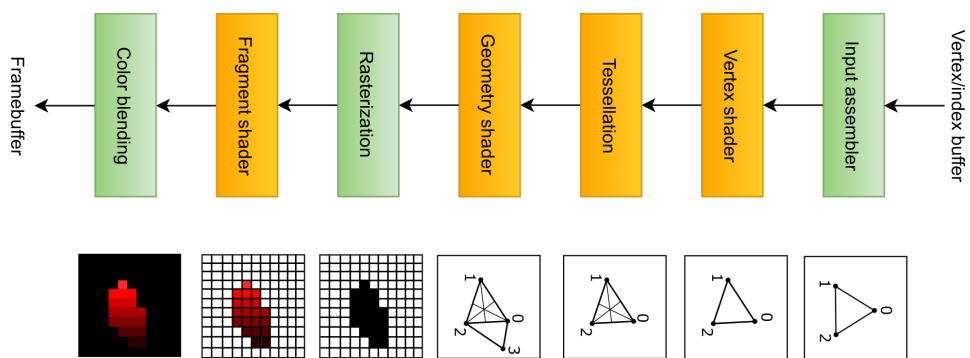


Figure 4.1: Simplified graphics pipeline of a modern GPU (from [Ove], A. Overvoorde)

An optimization exploiting this is called multiview stereo rendering. It very quickly surfaced as an idea after the introduction of the Nvidia Geforce 8 and ATI Radeon HD 2000 series in 2006 and 2007 brought unified shader architectures to the mass market [Lin+08][Som07]. Prior architectures relied on separate vertex and pixel shader units with relatively fixed

capabilities and few ways to share data. Fully programmable shader units then allowed more customizable and efficient pipeline usage necessary for multiview to show any benefit. The lack of mainstream stereoscopic systems prohibited the feature from becoming more important until the official introduction of multiview extensions to graphics APIs like OpenGL ([GL\\_OVR\\_multiview](#)) and Vulkan ([VK\\_KHR\\_Multiview](#), previously [\\_KHX](#) and [\\_NV](#)). The same resurgence saw the idea expanded and further optimized. In more recent vendor specific terms, Nvidia calls it Single Pass Stereo[Can16], Simultaneous Multi-Projection[Smi16] and Multi-View[BS18] rendering and AMD calls it LiquidVR multiview[Gal16][Jez17]. The idea behind all these terms is the same, albeit with detail differences between the different flavors.

The core concept of multiview rendering is to submit all draw commands for a stereoscopic frame in one call instead of two separate passes, which can cut down CPU render and transfer time depending on the type and amount of data pushed to the GPU. Expensive synchronization barriers are essentially halved and all necessary writes are performed in a single go. This is illustrated - albeit strongly simplified - in Figure 4.2, which makes it easily visible where multiview cuts out unnecessary work. As an addition, *hardware* multiview rendering is to only perform those pipeline stages multiple times which actually produce notably different data for each eye, such as the rasterizer and pixel shader stages, while only running the earlier stages with little changes once. The data from stages run only once can then be reused by the multiply run stages with very little extra cost. This expanded technique improves pipeline efficiency and will scale heavily depending on workload. For fragment-heavy applications the benefit will be limited while high vertex or geometry loads tend to scale more optimally. Hardware acceleration requires additional registers and pipeline shortcuts in the chip itself, which constrains it to more modern GPU architectures built with it already in mind. Nvidia can be considered the main drivers behind this, having pushed the technology from parallel geometry projection in Maxwell's Multi-Projection Acceleration to Pascal's SMP adding lens-matched shading to better approximate the lens shape. Finally, to Turing's Multi-View with a doubling of available views and positional independence to support state of the art HMDs with canted displays [BS18].

The small tradeoff is all relevant view data for each viewport having to be handed to the pipeline at once, creating a little higher memory overhead. Additionally, certain buffers such as geometry and indices for the vertex stage need to be uniform across all viewports and can not be altered for each eye as they are processed in a single pass.

Going by the user-maintained Vulkan Hardware Database [Wil20], the major GPU vendors offer multiview support in their architectures as follows:

- Nvidia: hardware multiview from the Pascal generation and newer, software support from Kepler onward
- AMD: software support from Graphics Core Next 1.0 onward
- Intel: software support begins with Generation 9.0 (Skylake/Apollo Lake GT) onward under Windows, Generation 7.0 (Ivy Bridge GT) onward under Linux
- Qualcomm: software support from Adreno 500 onward

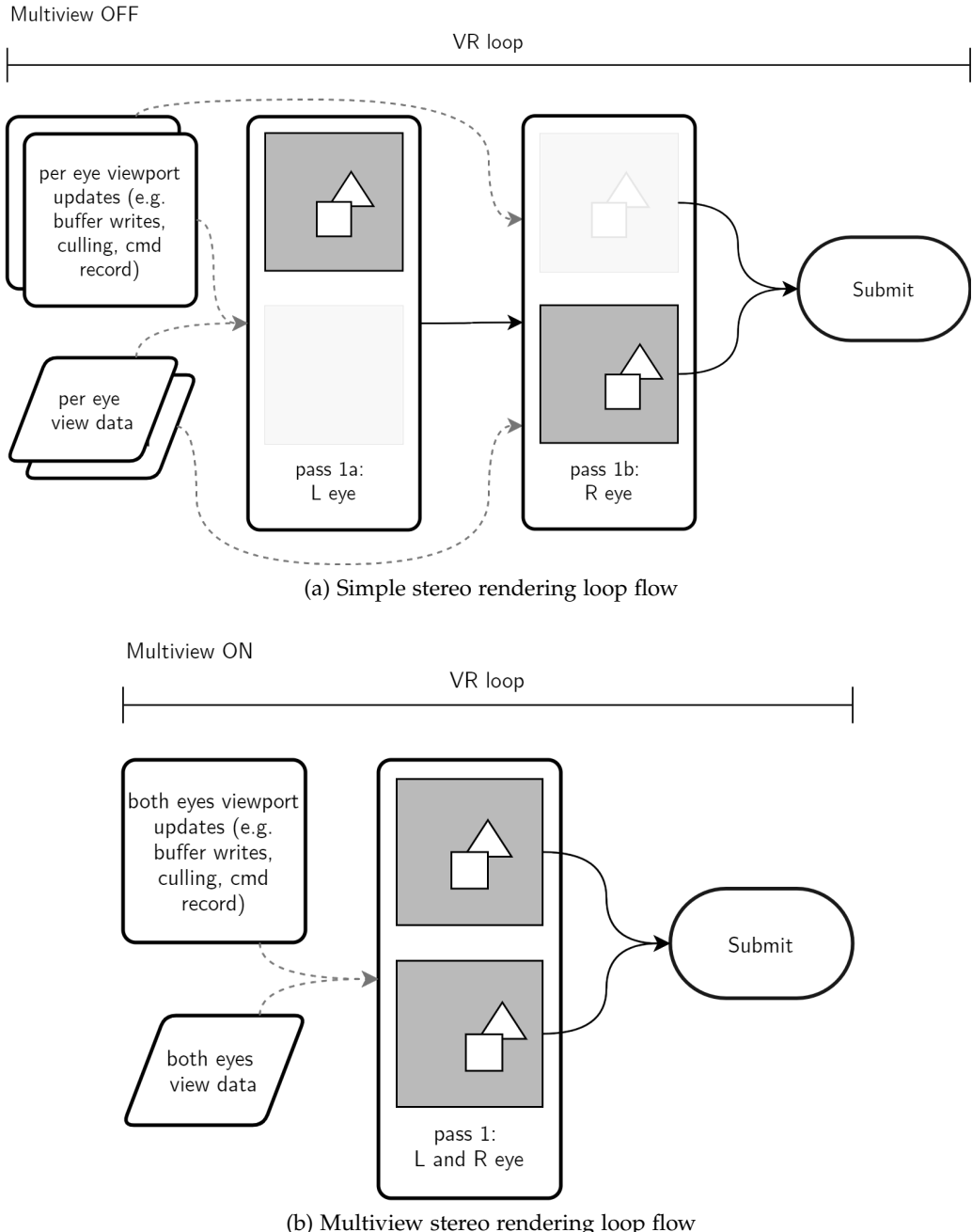


Figure 4.2: Simplified flow of standard stereo versus multiview render loops

- ARM: software support from Bifrost onward, limited support on Midgard
- Imagination: software support from Rogue onward

Note here, while support of the desktop parts is solid and stable, the ARM-based mobile chipsets often have incomplete or unstable drivers [Wil19][JMC18].

For all submitted devices (892 at the time of writing) the database shows support coverage of 54% on Windows systems, 69% on Linux systems and only 23% on Android. This statistic is not very reliable, since an undetermined portion of the submissions contains incomplete or flawed information such as drivers versioned as 0.0.0 or API versions reported as 0.0.1.

#### 4.1.1 Estimated impact

Impact of this extension is highly dependent on the specific workload, the used graphics hardware and the renderer structure.

Independent benchmark numbers are rare to find. In benchmarking the online racing simulation iRacing, Wolfgang Andermahr of ComputerBase GmbH attests a performance increase of between 14-21% when testing on a Nvidia GTX 1060 and GTX 1080 at 5760 by 1080 pixels. While this is not a VR application, it gives a first impression of potential gains when rendering multiple viewports using hardware-accelerated multiview as is the case on these Pascal-based GPUs [And16]. Similarly, Croteam's Karlo Jez shows significant CPU performance gains for software multiview using AMD's LiquidVR suite, reducing CPU frame time in Serious Sam VR from 9ms down to 7ms [Jez17]. He specifically notes that this includes all stages of CPU rendering, even ones that are not connected to multiview, and adds that render command processing itself is halved from 4ms to 2ms by using software multiview. Going further from traditional desktop rendering, Mozilla Corp. reports performance improvement of up to 40% when using the multiview extension for WebGL in a CPU-bound test application [Ser19].

Overall this gives inconsistent performance expectations, but it does provide a trend. It stands to reason that with rising CPU load and increasing number of virtual viewports, multiview rendering offers significant performance improvement in the double digit range.

#### 4.1.2 Implementation specifics

In Vulkan specifically, multiview is enabled through the `VK_KHR_multiview` extension. This extension's availability on the target hardware can be queried and if available, the individual hardware-dependent implementation is abstracted by Vulkan.

In the Tachyon implementation of multiview, the following changes to the render loop are introduced:

- The VR render target adds `VK_KHR_GET_PHYSICAL_DEVICE_PROPERTIES_2` to the required instance extensions and `VK_KHR_MULTIVIEW` to the required device extensions during Vulkan instance and device creation at startup
- the previously separate per-eye VR render passes are merged into a single render pass
- this VR render pass incorporates the multiview pNext extension using a view mask and correlation mask of 0x11, with each of those bits representing one of the eyes
- the Frustum Culling pass combines the two frustum checks with an early accept and outputs a merged set of draw call information

- the second command buffer recording - previously intended for the second eye - in `OpenVR::RecordCommandBuffers()` is cut out as multiview render passes can only take a single unified set of command buffers
- the underlying GLSL shader is modified to pick camera parameters based not only on a given camera index, but also the implicit `gl_viewIndex` as Vulkan multiview uses this integer to index the current viewport

The VR render target's framebuffer, color attachment and depth attachment are already set up as dual-layered buffers which makes them readily compatible with multiview render passes. With these changes, the Tachyon renderer is fully switched over to single pass stereo rendering.

## 4.2 HMD Stencil Mask

Introduced to the mass market with 3Dlabs' Permedia II in 1997 and widely adopted since then, all modern graphics chips support a useful feature called the stencil buffer. This buffer uses low bit integer values - commonly 8 bits per pixel for a depth of 256 [de 14] - which can be read from and written to during the fragment stage, with stencil testing happening after alpha and before depth testing. Sometimes used for certain shadowing operations, the stencil buffer is primarily used for cheap masking efforts.

One such effort was presented by Alex Vlachos at GDC 2015 [Vla15] as a possibility to improve performance in VR applications. Once again pointing at the significant areas of invisible screen space wasted outside the HMD lenses' warping reach (such as in Figure 4.3), the idea here is to write into a per-eye pixel matched stencil buffer a mask corresponding to the shape of the visible screen area. During the fragment stage of a frame render, the stencil test can early discard all masked fragments and thus avoid pixel shader work for all these areas. The operation works exactly as the classic idea of a stencil mask when painting surfaces. Paint will only hit the surface within the cutouts of the stencil. Similarly the graphics chip will only write color and depth values to unmasked fragments.

An alternative way of rendering the stencil mask is to draw it as a mesh into clip space at depth 0 at the start of each stereo render pass. This way masked pixels will fail early Z testing for all further geometry and achieve the same effect as the literal stencil buffer mask. One downside of this is that it has to be done each frame instead of reusing a once drawn mask, but the advantage compared to stencil buffer masking is that no stencil layer is required. As such this alternative way lends itself primarily for applications that otherwise don't need the stencil buffer.

### 4.2.1 Estimated impact

The performance gain naturally scales well with both increased fragment shader bias of the per-frame workload as well as with the HMD's blind areas. In his GDC talk, Valve's Alex Vlachos, showcased gains of 17% lower GPU fill rate for the company's Aperture Labs VR

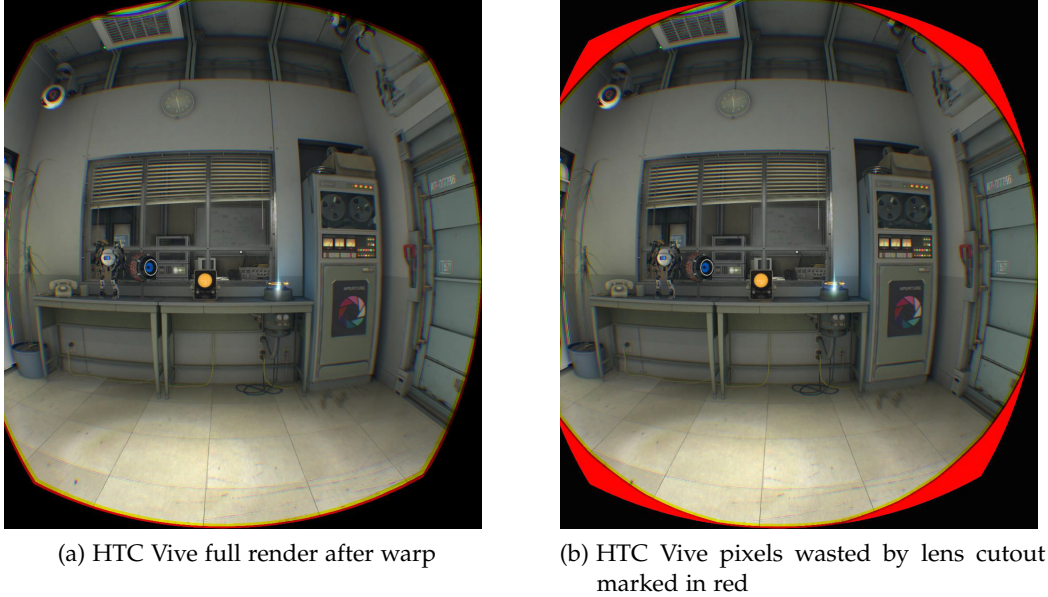


Figure 4.3: Comparison of rendered rectangular right eye frame after warp versus pixels wasted by lens distortion (from [Vla15], pp. 52-54, A. Vlachos. 2015)

showcase scene using an HTC Vive headset ([Vla15], p. 59). Assuming a roughly uniform distribution of objects in the scene and, accordingly, a roughly constant shader workload during use, the relative improvement in fragment render time is directly proportional to the masked percentage of the total framebuffer.

#### 4.2.2 Implementation specifics

The rtvklib stencil masking feature is designed to query the required fitted meshes from OpenVR and render them to the respective eye at startup so the render loop can keep reusing it every frame without additional render load for the mask (see Figure 4.5). An example of the rendered mask is shown in Figure 4.4, displaying the Nsight VS stencil buffer capture when using a Valve Index headset.

Outfitting Tachyon for stencil masking required the addition of the entire stencil stack as the engine does not use the feature in any other capacity. The changes include extending the depth attachment of the OpenVR render pass with the `VK_IMAGE_ASPECT_STENCIL_BIT` so the additional buffer layer is created at startup. The involved Vulkan pipelines need stencil operation states defined in their `VkPipelineDepthStencilCreateInfo`, with the operations set as in Figure 4.6 so the bits are checked against but not modified. Next, the VR render pass needs its color attachment's `stencilLoadOp` set to `VK_ATTACHMENT_LOAD_OP_LOAD` so the renderer knows to load the stencil buffer at the start of the color pass, and the `stencilStoreOp` to `VK_ATTACHMENT_STORE_OP_DONT_CARE` so it can leave the buffer behind after use without saving anything more to it. This is important to make sure the stencil buffer

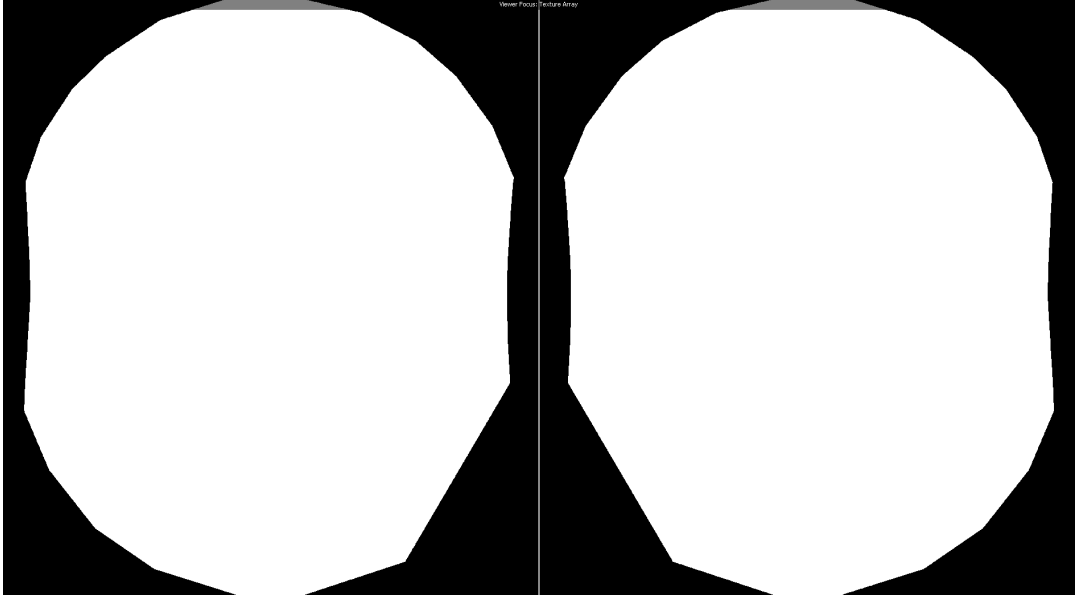


Figure 4.4: Nsight VS capture of stencil buffer as rendered for Valve Index HMD

remains unmodified and expensive writes are avoided.

Rendering the stencil mask itself at startup is done as follows: OpenVR by now has some helper functions for masking built in, such as the `GetHiddenAreaMesh(EVREye eEye)` function that returns a screenspace-normalized list of vertices representing the ideal mask mesh for the current HMD if available to OpenVR. Exceptions apply, as the API does not contain mask definitions for all headsets. As an example, the mesh query returns an empty list for the Oculus Rift CV1 as seen in Figure 4.7. With this in mind, the main benefit is the simplicity of getting a fitted mask for most HMDs instead of either approximating with circular masks or going through the trouble of manually creating fitted meshes for existing and upcoming OpenVR-enabled headsets. For exception cases a fast circular approximation mask may be an adequate compromise.

Tachyon queries OpenVR for the mesh of each eye, converts the vertex lists into a renderer-compatible vertex format and writes out a vertex and index buffer each. At the end of the VR render pass, an ad-hoc command buffer is recorded and submitted to render the two masks into the VR framebuffer's depth attachment's stencil layer. The `VK_IMAGE_ASPECT_STENCIL_BIT` is set to ensure only that layer is written to.

Due to Vulkan's verbose nature, rendering these two masks also requires its own pipeline. The default material and PBR pipelines only do stencil test compares, no writes and they perform color writes and rasterizer face culling, which are all things the stencil mask pipeline should do differently. A separate stencil pipeline is introduced with the stencil operation state set like in Figure 4.8, the color writes masked off and rasterizer culling disabled. Should the need to perform per-frame stencil writes arise, merging the material pipelines and the stencil pipeline may prove beneficial to avoid expensive pipeline re-binds but for the sake of cleaner separation the described setup was used in Tachyon's current implementation.

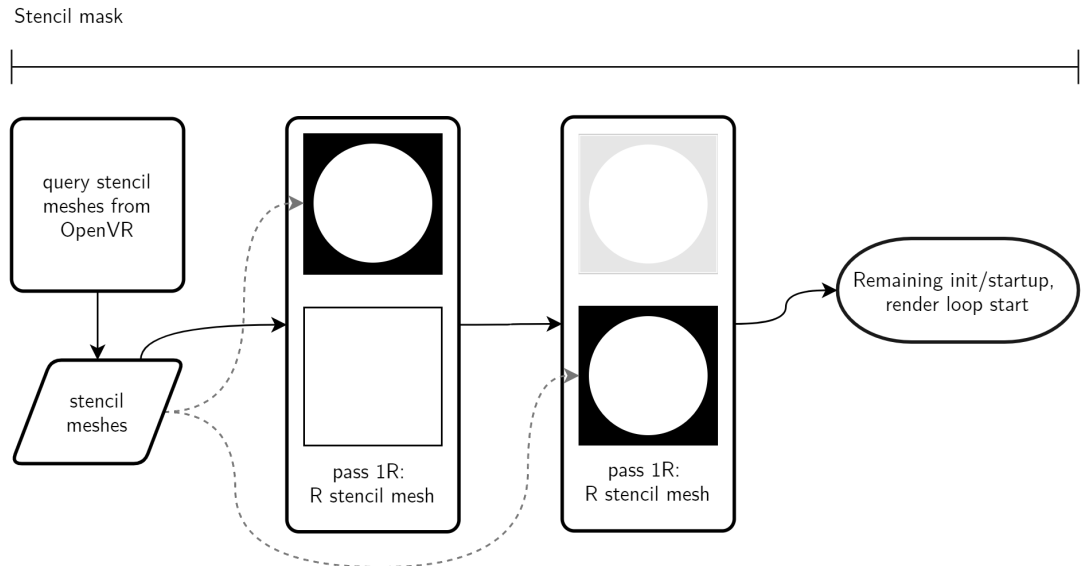


Figure 4.5: HMD stencil mask query and render flow in rtvklib

### 4.3 Monoscopic Far-Field Rendering

Monoscopic Far-Field Rendering (MFFR) is an approach strongly leaning toward an inherent property of many optimizations in the field of rendering and real-time computing in general, which is the property of trading accuracy for speed. MFFR is a topic brought up again soon after Oculus Rift CV1's retail launch by Oculus developers Rémi Palandri and Simon Green at developer keynotes like the ARM GDC 2017 talk[DPV17] and the Oculus Developer Blog as Hybrid Mono Rendering[PG16].

Understanding the concept requires some explanation of the technical and visual background. Depth perception of the human eye relies on the slight spatial distance between both eyes as each eye sees a slightly different angle of a given object. This difference in perceived angle is

```

//stencil op settings for pipelines using
//the stencil mask for comparison
VkStencilOpState stencilOpState = {};
stencilOpState.compareOp = VK_COMPARE_OP_NOT_EQUAL;
stencilOpState.failOp = VK_STENCIL_OP_KEEP;
stencilOpState.depthFailOp = VK_STENCIL_OP_KEEP;
stencilOpState.passOp = VK_STENCIL_OP_KEEP;
stencilOpState.compareMask = 0xff;
stencilOpState.writeMask = 0xff;
stencilOpState.reference = 1;

```

Figure 4.6: Stencil operation flags set for default material Pipeline

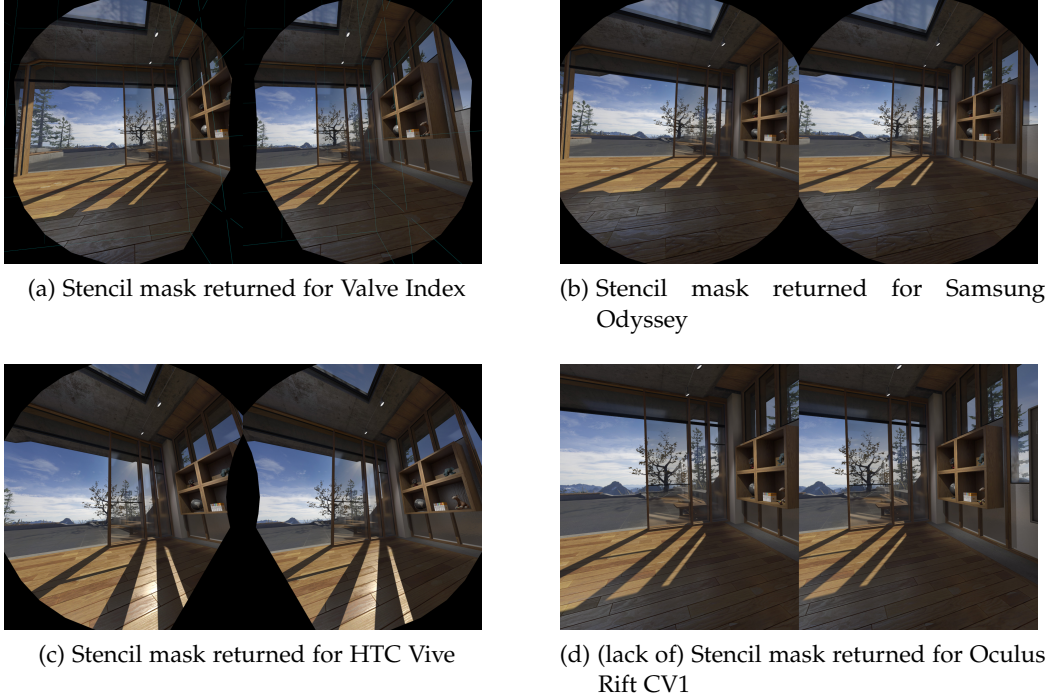


Figure 4.7: Comparison of stencil mask availability (while running SteamVR home)

called stereo separation. Without it, the brain has difficulties determining the depth at which a certain object or surface lies. Regular stereo rendering recreates this separation correctly when rendering the two virtual eyes at their respective spatial offset from the HMD center - given correct projection and view matrices and accurate world scale at least.

However, as distance grows, stereo separation shrinks - the aspect MFFR exploits. In infinity, separation would be infinitely small. Even at more reasonable distances separation is small enough so even with good vision it is hard to properly judge depth unless the object is large. This of course also holds true for rendered stereoscopy, but an additional limit is the pixel density of the output displays. This means that at a certain distance from the virtual camera, stereo separation will shrink to less than a full screen space pixel once projected. If the difference can not physically be displayed by the HMD, it is a waste of resources to still render both eyes.

Mono Far-Field Rendering opts to skip the second view during rendering of the name-giving far field of objects. The hope here is to only render a single view past a certain distance, reducing rendering load without the user noticing the theoretical loss in accuracy. This approach has caveats however. The value at which a field split - the distance at which the stereo rendering is cut off and followed by only mono rendering - will depend on the individual user, their quality of vision and spatial awareness. It will also potentially depend on the resolution of the used headset given the user's vision is good enough to not deteriorate

```
//stencil op settings for the stencil pipeline
VkStencilOpState stencilOpState = {};
stencilOpState.compareOp = VK_COMPARE_OP_ALWAYS;
stencilOpState.failOp = VK_STENCIL_OP_REPLACE;
stencilOpState.depthFailOp = VK_STENCIL_OP_REPLACE;
stencilOpState.passOp = VK_STENCIL_OP_REPLACE;
stencilOpState.compareMask = 0xff;
stencilOpState.writeMask = 0xff;
stencilOpState.reference = 1;
```

Figure 4.8: Stencil operation flags set for stencil mask Pipeline

before that point. Note here, this thesis will not explore these constraints of MFFR further than approximate values used for testing as time does not allow more.

MFFR has been implemented by Oculus LLC and Epic Games Inc in Unreal Engine 4 and was recommended for certain types of pixel-bound mobile VR experiences with very limited GPU power but has been removed from the engine in update 4.20 without further explanation. An odd decision, as UE documentation posts prior to the removal indicated continued optimization efforts such as added compatibility with UE4's multiview path[16a].

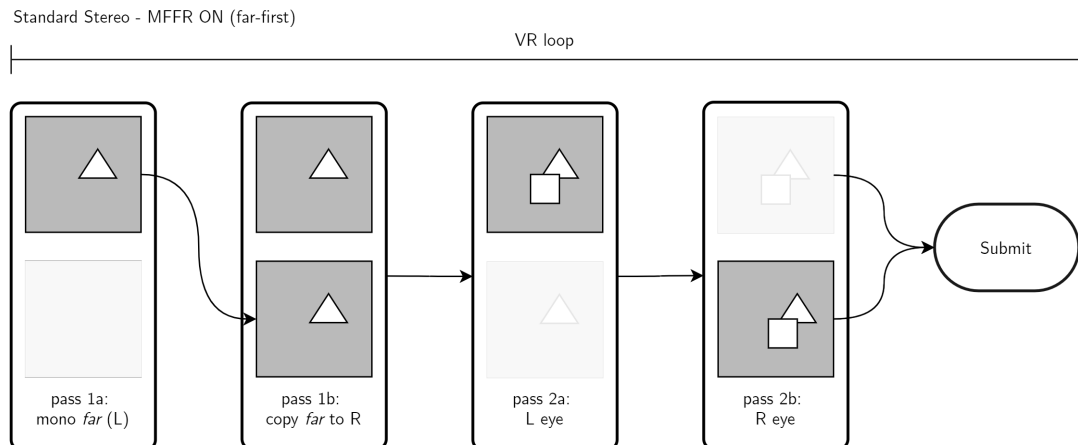


Figure 4.9: Per-frame render pass flow of far-first MFFR;

Each row represents one image buffer, each column represents the process steps the respective buffer is subjected to

### 4.3.1 Estimated impact

The makeup of the scene itself will also affect the effectiveness of the solution. As cautioned by Oculus LLC in their developer reference on Mono Far-Field Rendering [PG16], there is a certain baseline overhead simply for enabling the additional render pass necessary for the

monoscopic image and the associated context switches. Furthermore, only scenes with a significant amount of distant geometry beyond the field split distance will benefit from the optimization, as obviously the second view workload can only be saved for objects originally contained within that second pass.

Going purely by Palandri and Green's blog entry, their forward-rendered UE4 implementation supposedly running on a GearVR device saw frametimes in the Epic SunTemple sample scene drop by 25% and their best-case Unity test scene demonstrated a 49% drop[PG16]. This would indicate that if circumstances allow - meaning pixel-bound forward-rendered large scale scenes - impressive performance gains well upwards of 20% can be expected, while less suitable cases in the worst case will see no change if not minor regression.

#### 4.3.2 Far-first approach

Implementing Mono Far-Field Rendering into Tachyon - or any renderer for that matter - requires care and a number of changes. There are at least two possible ways of doing it, both by way of multiple render passes and with their own respective drawbacks and advantages. One way of implementing MFFR is doing the far pass first in each frame, followed by a near pass, both possibly using the same framebuffer as illustrated in Figure 4.9. At the start of the frame, the framebuffer is cleared - color and depth clear are necessary - after which the far-field command buffers are submitted and executed. This pass can render directly into the buffer of one eye and copy color and depth buffer to the other eye. Finally, the near-field command buffers are submitted and render their values into the buffers already containing the far field information. For this case, one extra step needs to be performed. As the projection matrix normally projects the world as seen by the camera into a uni-cube with each axis being length 1 going from 0 to 1 and this same uni-cube is used for both depth value calculation and projection clipping (triangle discard via clip space evaluation), the two passes can not share the same uni-cube. Ways around this would be to either use regular full-depth projection matrices and clear the depth buffer before the near pass or to scale both passes' projection matrices by 0.5 and translate the far projection by 0.5 so the uni-cube is shared between the two fields without overlap.

If neither is done, the effective depth values of far-pass objects will be closer than they should be and possibly closer than those of near-pass objects, leading to some near-field objects being drawn behind far ones. The depth buffer clear option has the benefit of utilizing full projection precision and correct triangle clipping. The matrix squashing option avoids an extra clear but means vertices otherwise clipped outside of the uni-cube are pulled into the uni-cube and not skipped.

The overall advantage of this far-first approach is it yields a full precision far-field depth buffer which may be useful for stereo interpolation as briefly described in the subsection 4.3.6. The disadvantage is early Z discard cannot be fully effective as all far geometry is rendered first even if opaque geometry close to the camera would later obstruct it. Whether the benefits of lower split distance coupled with interpolation can outweigh the additional cost of overdraw heavily depends on the scene and how much geometry is contained within the far volume. The goal of this approach is to reduce memory operations and locality to a minimum and

avoid more costly compositing methods.

### 4.3.3 Near-first approach

The alternative to rendering the far pass first is to render the stereo near volume at the start of each frame as illustrated in Figure 4.10. A key difference to the former approach is the first pass needing to flag the stencil buffer pixel when an opaque fragment is within the uni-cube and a color value is written. After the stereo pass, each eye contains a binary stencil mask of the near-field occluded screen areas. In the next step, the far pass can then execute regularly except with stencil testing enabled. This sequence has no direct need for depth buffer clearing or uni-cube sharing. However, the constraint is the far pass also needing to sample from left to right eye separately as a straight buffer copy cannot work anymore. The advantage of this approach over far-first is early Z discard takes full effect and stencil masking reducing the leftover render area even more. The downside is the need to perform additional stencil writes every frame and potentially costly sampling operations.

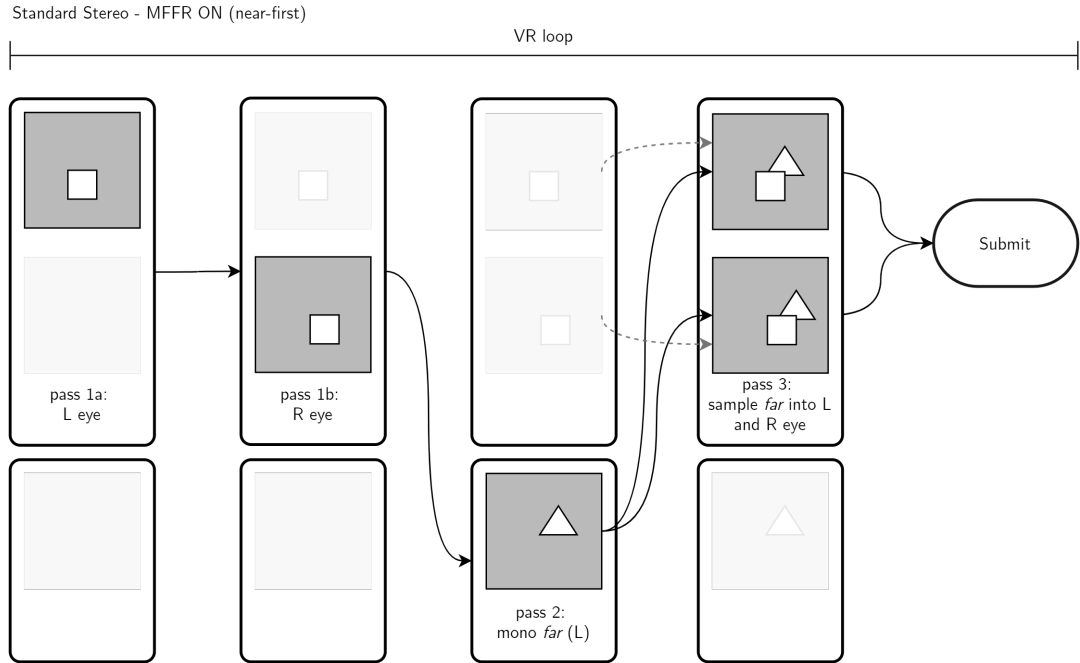


Figure 4.10: Per-frame render pass flow of near-first MFFR;

Each row represents one image buffer, each column represents the process steps the respective buffer is subjected to

### 4.3.4 Implementation specifics

In this thesis, the plan is to do far-first MFFR, albeit the measured results are not favorable. In the first step of each VR frame, a monoscopic render pass renders the far clip volume's color

and depth values into the index 0 layer of the framebuffer. The next step is to copy that layer to index 1 as well. In the final step the regular stereoscopic render commands are executed with reduced near field clip volume, including clearing the depth buffer at the start of the stereo pass to avoid the uni-cube issue. While the general approach is mostly straight-forward and both described ways are possible, implementing either in a Vulkan renderer is no trivial task and requires the following changes to rtvklib:

- for the virtual camera, a field split distance parameter is introduced and an additional frustum is added; the stereo frustums cover the volume from near plane to split plane while the far field frustum covers split plane to far plane
- the frustum culling procedure is altered to write the far frustum's resulting draw commands into a separate set instead of merging them into one (as would happen for regular multifrustum culling in Tachyon)
- at initialization time of the VR render target an additional render pass is created for monoscopy with the main difference - compared to the regular VR render pass - being the removal of the multiview extension
- an additional set of Vulkan `VkCommandBuffers` is added, into which the draw commands of the far frustum cull set are to be recorded
- an additional set of `VkSemaphores` is added to synchronize the two render passes and create them in `CreateSyncObjects()` during initialization
- an additional `VkCommandBuffer` for the layer copy operation is added
- at initialization time of the VR render target this copy command buffer is pre-recorded so it can be reused every frame; this recording includes transitioning the layout of both the color and depth image from `VK_IMAGE_LAYOUT_TRANSFER_SRC_OPTIMAL` to `VK_IMAGE_LAYOUT_GENERAL`, `vkCmdCopyImage(...)` both images' layer 0 to layer 1 and then transitioning the layouts in reverse again
- in the per-frame recording procedure of the VR render target, `RecordCommandBuffers(...)`, the entire structure of begin and end of command buffers and render pass and per-pipeline `RecordDrawCommand(...)` calls is duplicated with the monoscopy render pass and far field command buffers set; afterward the prior regular stereo recording still takes place
- in the render target's `RenderFrame(...)` function the far field command buffer and layer copy command buffer submission is inserted before the regular stereo submits; the mono submit is set to wait on `mRenderCompleteSemaphores` and signal `mFarfieldCompleteSemaphores`, while the stereo submit is only set to wait on the latter
- in VR render target's camera setup, the far field frustum projection matrix is constructed as outlined in [Lap17] pp. 515-519 - albeit transposed as Tachyon still retains the OpenGL matrix format for a few matrix types

- an additional set of camera data struct and camera index is added
- in the render target's `UpdateCameras()` call, the far field volume's view projection matrix is updated by transforming aforementioned projection matrix by the current HMD pose and the updated matrix is written to the camera data buffer on the GPU

#### 4.3.5 rtvklib MFFR failure

Some issues with this implementation prevail and make it unfit for productive deployment in Tachyon. For one, while the projection matrix itself uses the correct parameters, view matrix transformation used for the far field remains incorrect, so head movement leads to incorrect projection distortion effects on the horizontal axis. While the lack of pure separation at little to no sideways tilt may be acceptable and not easily noticed with a correct view matrix, tilting the head means more severe separation mismatch as the spatial disconnect is expanded from being mostly horizontal to being horizontal and vertical, clearly visible in Figure 4.12. Fixing this disparity would require translating the far field image of each eye to conform more closely to the expected overall stereo shift. Vitally, this visual distortion does not affect performance measurements presented in chapter 6 as the used internal culling frustum is computed from the virtual camera's world position and direction in any given frame and not subject to incorrect projection transformation. Subsequently, submitted draws and render passes are correct and executed in the described order, as exemplified by the Nvidia Nsight VS debug timeline in Figure 4.11.

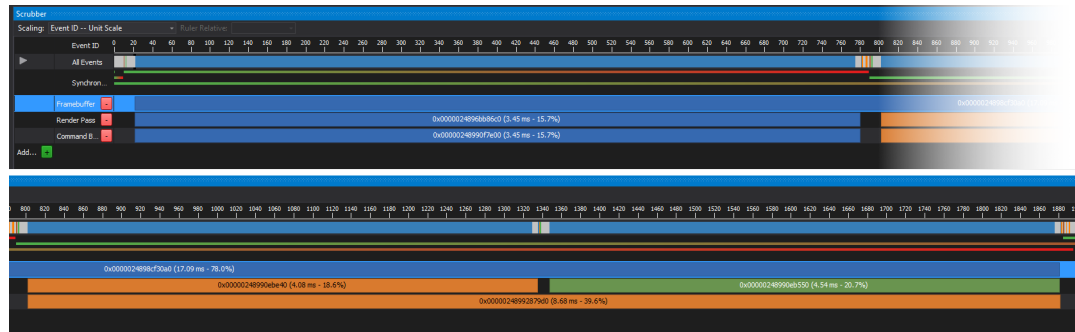


Figure 4.11: Draw submission and render pass binding timeline of a typical rtvklib MFFR frame, captured in Nsight VS. (Split after far-field render pass and stacked vertically for better page fit)

On the "Render Pass" row, the blue pass denotes the far-field pass, orange is the left eye and green is the right eye. Far and near are each synchronized by a `VkSemaphore`.

Secondly, Vulkan render passes discard fragments at their end by default if depth testing is enabled and the depth value of said fragment equals 1.0 (and is thus on the far plane). This means any color values written by the far pass and not overwritten by the near pass are discarded right at the end of the stereo pass and before presentation. A workaround for this

is to clear the depth buffer at the start of the stereo pass not to 1.0 but to 0.999999, which is the closest value an IEEE-754 float can reach below 1.0 (22 of 23 mantissa bits set to 1). With this tweak, color values were composited together without any visible loss at the near field's split plane, even if it technically entails a depth clamp in that last mantissa bit.

Lastly, and most importantly, performance simply is not up to par. On the i7 and RTX2080 test system (**WS-Big**, see chapter 5), enabling MFFR with a sufficiently far split distance yielded a 34% performance loss. The culprit for this is most likely two-fold. One factor is the detrimental Z ordering of the submitted draw commands since much of the far field color buffer is overdrawn by the near pass and thus counts as wasted effort. The other factor is the lack of parallelism due to the use of a shared framebuffer. The two render passes need to be synchronized to run in order and cannot be scheduled on parallel thread warps to increase GPU utilization and thus performance. What's puzzling in this scenario is that Palandri et al. in their Oculus blog entry[PG16] saw a clear performance uplift in a Unity sample scene with seemingly very similar MFFR construction.

As such, the rtvklb MFFR implementation as presented here remains beneficial only in theory and will require further work to result in real performance gain.

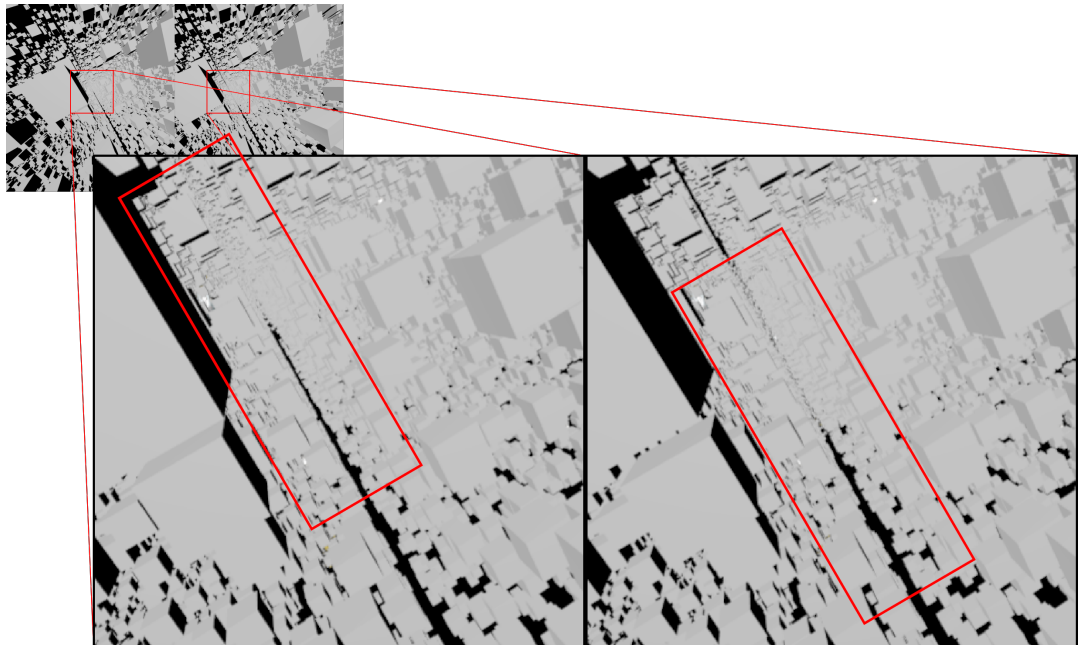


Figure 4.12: Incorrect monoscopic far field distortion (notice the thin center line of distant geometry shifted up and left in the Left Eye image, but shifted down and right in the Right Eye image)

#### 4.3.6 MFFR Variant: Depth Shift

In its basic version MFFR as described in section 4.3 completely foregoes separation beyond the split distance and as such the split distance has to be set relatively far back to minimize

the visual inaccuracy. Naturally, an attempt to try and reduce that split distance closer to the camera is by artificially and cheaply increasing that accuracy again. One such way is to use the data already contained in the framebuffer's depth layer during rendering. As stereo separation is mostly dependent on depth, given the object itself and its properties are known, an improvement is to approximate small amounts of separation based on that depth buffer. Instead of simply copying or sampling the far image to both eyes after the far field pass, one can do an additional sampling or post-processing pass which includes slightly shifting pixels according to the depth value of the respective given fragment.

This interpolation should allow pulling the field split distance closer to the camera and save some stereo render time, but it is unclear whether the savings outweigh the additional processing cost and this thesis does not explore MFFR beyond the base variant.

#### 4.3.7 MFFR Variant: Alternate eye

Another possible way of pulling in the split distance value while retaining approximated separation comes back to the VR property of high framerate as explained in earlier chapters like the Round Robin Culling (section 3.4). Assuming high framerate and refresh rate, the mono render pass could be called with the camera parameters not custom calculated as a middle point between the two eyes but alternating between left and right eye parameters each frame. This way, each alternating eye would be correctly projected every other frame and incorrect data would likewise only persist for one frame at a time in each eye. If this eye-alternating MFFR were to be combined with interpolation of the respective incorrect eye, the perceived inaccuracy (seen as flickering as the visual information is only incorrect every other frame) may be further reduced. Candidates for this are a simple frame interpolation or a single frame temporal reconstruction, although a single previous frame may not be enough for stable results.

Once again this thesis does not encompass this additional option and thus it is unknown how far the split distance could be pulled in and whether related savings would outweigh interpolation cost. Just as with Round Robin Culling, the same potential artifacts and issues are present here.

### 4.4 Foveated Rendering

This technique lends its name from the fovea centralis, a spot in the center of the primate retina, responsible for sharp central vision of the eye. The regions around it gradually lose visual sharpness as they contain fewer and fewer cone cells. Foveated rendering in its various forms builds on this limitation of the human photoreceptive system. For example, as described in the Oculus Go optimization guide by Palandri et al.[PGP18] the image produced by a VR renderer is warped by the VR compositor to closely match the spherical shape of the lenses and the distorted field of view they create. This warping means that toward the edge of the frame, more pixels are compressed into a given angle of vision than in the center, effectively leading to much higher pixel density for peripheral regions. Conversely, the

peripheral vision of the human eye is usually significantly less sharp than the aforementioned foveal vision. Therefore the outer rim of the rendered image can be rendered at much lower pixel density without sacrificing a humanly noticeable amount of detail if the HMD can even physically display this density. Exactly that is the concept of foveated rendering, it decreases resolution of the edge regions of the image while rendering the central area at full resolution. However, there is one big constraint. The foveal vision of the user and the artificial foveal center of the image need to match up, otherwise a user may easily notice the lowered pixel density. To accurately match these two focus points, the user's eye movements need to be tracked and the supposed focus center of the image adjusted accordingly.

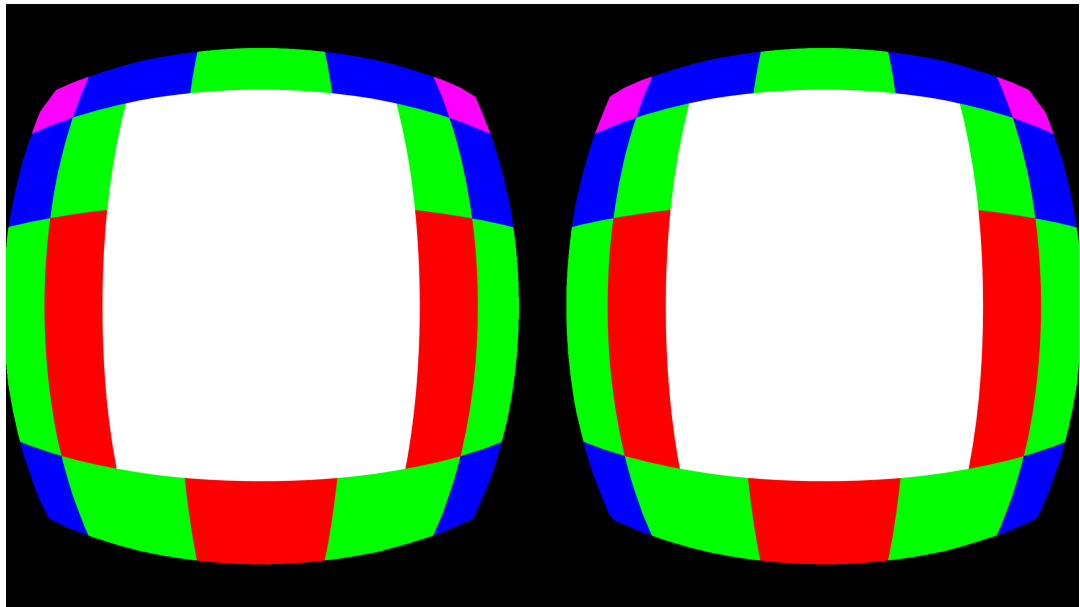
#### 4.4.1 Fixed versus True Foveated Rendering

Eye tracking can be foregone in theory, assuming the headset's field of view is low enough to physically discourage a wide range of eye movement and instead rely on head rotation. Additionally, the opening angle of the foveated region should be wider so eye movement on a small scale is still without consequence for the perceived image quality. The resolution of peripheral areas may not be reduced as much as with so-called *true* foveated rendering so even when the user briefly looks at such an area, the perceived loss is not as distracting. This compromised form of the technique is commonly called Fixed Foveated Rendering, for example available on Oculus Go ( 4.13a).

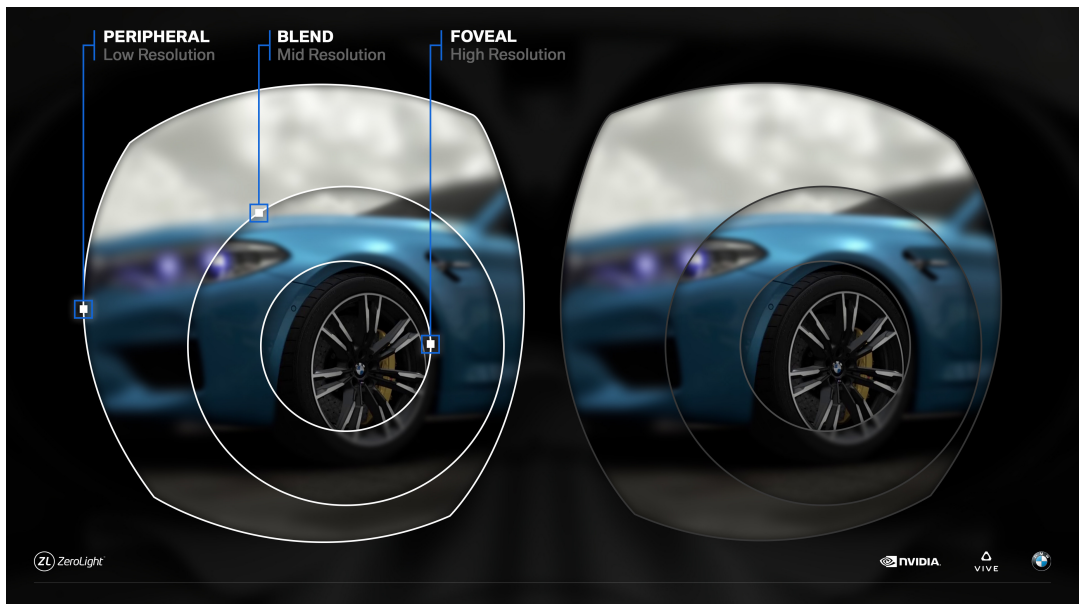
Given eye tracking of some adequate sort is available, true foveated rendering can be performed in which in each frame the current focus position of each eye is queried and the virtual view matrix adjusted accordingly. This makes the rendering setup more complex as the high pixel density area can shift to any location within the image but it allows for a tighter foveal angle and lower peripheral resolution as it is much less likely - if not entirely impossible due to limits or occasional mistakes by the tracker - for the user to focus on any such low density frame data. See ZeroLight Limited's Nvidia VRS based approach in 4.13b.

#### 4.4.2 Radial Density Mask

A somewhat related technique is called radial density masking as shown by Valve's Alex Vlachos in his talk at GDC 2016 [Vla16]. The goal is the same as with foveated rendering but the approach is different to better exploit traditional GPU architectures. Instead of reducing the theoretical rendering resolution of the peripheral ring, a mask is overlaid. The mask has the render pipeline skip a certain pattern of pixels in that ring. This can either be done by marking a checkerboard pattern of pixels in the stencil buffer so the pixel shader fails the stencil test on them - coming back to section 4.2 - to get a pixel perfect mask, or by overlaying a masking mesh right at the near plane of the render volume so the respective fragments are discarded during early Z tests. The latter would allow to approximately match a relative area reduction target but may not be pixel perfect depending on internal frame resolution. The resulting checkerboard area can then be interpolated and filtered to reconstruct the missing information. Vlachos claims gains of up to 15% for the Valve Aperture Robot Repair demo scene, but warns that reconstruction cost needs to be kept lower than mask savings.



(a) Oculus Go Fixed Foveated Rendering map (colored tiles decrease in resolution outward) (from [PGP18], R. Palandri et al., 2018)



(b) Dynamic Foveated Rendering using Nvidia Variable Rate Shading on HTC Vive Pro Eye (from [19], 2019)

Figure 4.13: Foveated rendering examples

### Adaptive resolution

The described methods of fixed/true foveated rendering and radial density masking can be combined further with another - by now almost universally used - optimization compromise:

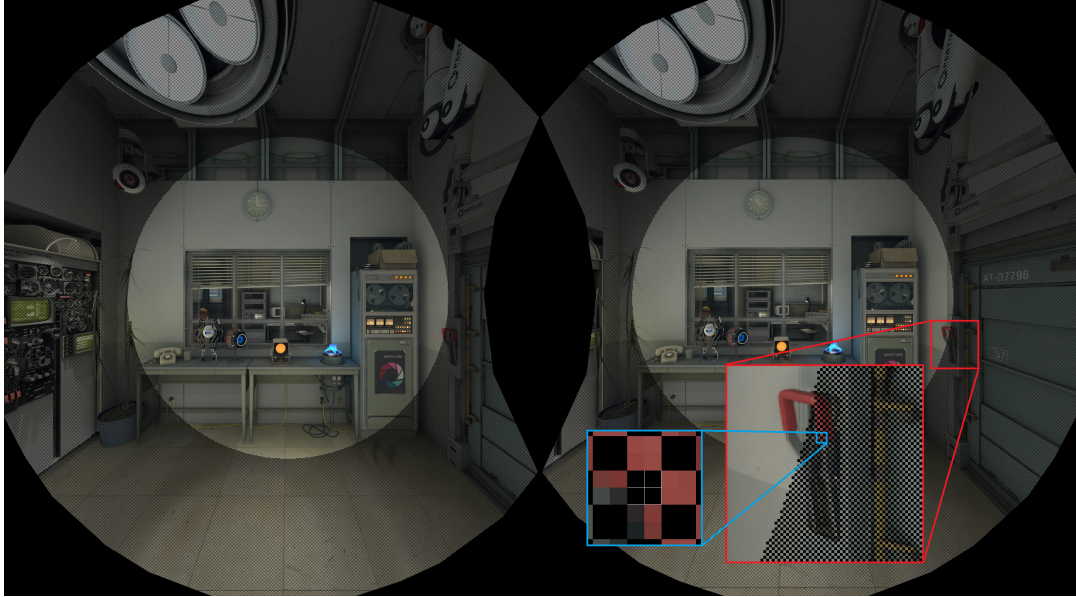


Figure 4.14: Radial Density Masking (2x2 px checkerboard) (from [Vla16], p. 22, A. Vlachos. 2016)

dynamic resolution scaling. While monitoring GPU load or frametimes and framepacing, the resolution of not just the central fovea but the peripheral regions too can be reduced or increased within given bounds. This can stabilize performance at the cost of some visual quality in the outer regions or - at the other end of the spectrum - alleviate some of the quality reduction if the available power overhead allows.

#### 4.4.3 Relevancy of GPU architecture

The previous sections describe various methods but the choice which of them is ideal for a given engine depends a lot on the target hardware. Foveated rendering relies on splitting the frame into several rectangular sub-frames and rendering them at differing internal resolution. Thus, it is only suited for GPU architectures supporting or better yet being built as so-called tile based renderers. Tile based GPUs such as Qualcomm's Adreno line and most other low power mobile SoCs compute the frame parallelly in a number of set tiles. On the other hand traditional GPUs execute render commands only on a frame as one entire unit, called immediate-mode rendering, albeit with possibly many more compute units at once. These tile based architectures naturally make it very simple to render tiles outside the foveal center at lower resolution without additional overhead, with the fovea circle being better approximated the higher the tile count is.

Older, traditional architectures like those found in many Nvidia and AMD desktop graphics chipsets are rarely built as tile renderers and may only support this tiling in software. Recent architectures starting with Nvidia's Maxwell and AMD's Graphics Core Next 1.0 support a hybrid form of tile based rendering, for example Maxwell still uses an immediate-mode

pipeline but uses a tile-based rasterizer buffering 16x16 or 32x32 pixel tiles to improve cache locality and overall shading efficiency[Kan16]. Graphics APIs can abstract these into more easily exploitable form. Such low-level optimized and accelerated solutions exist in Vulkan and DirectX12 alike, most notably Nvidia’s Multi-Res Shading[16b] and AMD’s LiquidVR MultiRes[Gal16]. On those, rendering frame regions at different resolutions requires internally splitting a frame into multiple viewports with a subsequent composition pass. This sequential process incurs additional overhead as it requires broadcasting geometry information to all these viewports, which is not possible in an efficient way on all GPU architectures as it relies on similar functionality as multiview (section 4.1) except with significantly more target viewports. The radial density mask approach may be more suitable for such traditional GPUs as it manages to render multiple resolutions within a single render pass by leveraging fragment discard features. This masking will necessitate an interpolation pass to blend away the masked pixels, while foveated rendering can technically skip further interpolation. Filtering the low resolution perifoveal pixels is recommended to reduce aliasing.

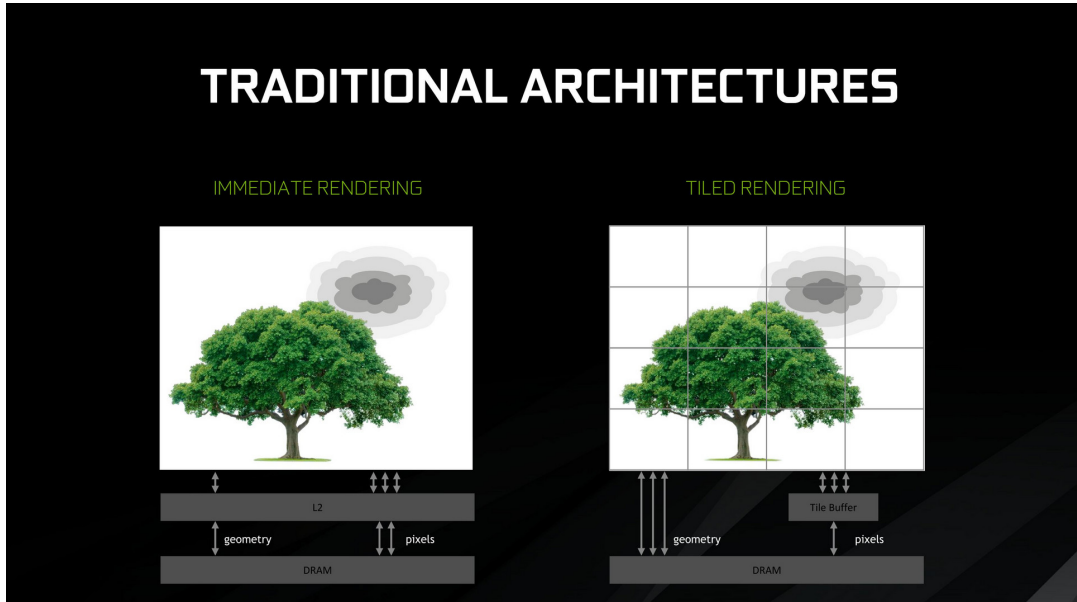


Figure 4.15: Traditional immediate-mode rendering versus tile-based rendering at Nvidia GDC 2017 Editors Day presentation (from [Ngo17], A. Ngo, 2017)

# 5 Performance testing setup

As can be gathered from the previous chapters, the optimizations implemented in Tachyon for this thesis are

- Superfrustum Culling
- (vendor agnostic) Multiview Stereo Rendering
- HMD-matched Stencil Mask
- Monoscopic Far-Field Rendering

While expectations for the first three items were optimistic, it shall be noted again that MFFR unfortunately turned out unsuccessful, which will reflect in this following chapter.

## 5.1 Benchmark scene

In order to properly assess how each of these implementations fares at run-time and how it impacts performance of the engine, a series of benchmarks were conducted. To ensure repeatability of the benchmark, a synthetic test scene was constructed, aimed to stress the tested systems to a degree not likely found in many real scenarios. While this may seem counterintuitive, it paints a worst-case picture of performance to be expected and how the tested methods hold up.

This test scene is built as follows: the scene dimensions are set up as 32 by 32 `chunks`, each `chunk` sized 80 units on each axis. This gives an overall scene volume of 2560 by 80 by 2560 units. This seems strongly skewed towards lateral expansion rather than vertical, chosen primarily due to the expected productive use being industrial scenes covering large factory floors but not necessarily very vertical setups. Another reason is that the Tachyon scene `chunk` system currently does not allow stacking of `chunks` and as such an adequate compromise between scene scale and octree scale had to be chosen. Filling this test scene is a selection of objects, the geometries namely being a primitive cube and three high polycount objects, a robot called "Robi", a material showcase sphere and a PBR showcase helmet. While such condensed high detail polygon amounts are not an ideal showcase, they provide enough geometry load for a synthetic test. As culling is done not per object but per octree cell, the distribution of geometry within small spaces is a lesser issue and the overall distribution achieved here is consistent enough for tangible testing. These objects are placed in the scene by iterating through a counter for each axis and placing an object instance at each new count. To determine the instance position, the three axis counts at that moment are multiplied by a

spacing of 3.6 and a entropy value is added to each axis. This entropy value is combined as `x = sinf(sinf(x) + cosf(y) + tanf(z)), y = cosf(sinf(y) + cosf(z) + tanf(x)), z = sinf(cosf(sinf(z) + cosf(x) + tanf(y)))`. Adding this artificial entropy makes the scene look more chaotic but is still deterministic and repeatable. By default the placed object is a primitive cube, but at every intersection of  $x+z$ ,  $y-z$  and  $z$  counts valued 11, one high polycount instance is placed, with the chosen type being modulo-index-incremented over the available high polycount types. This placement setup is done with target counts of 711 for the X and Z and 22 for the Y axis respectively. This utilizes the scene height as much as possible and results in a total instance count of 11.121.462, a respectable number even for detailed industrial applications. In a flythrough in the 2D mirror viewport, the scene looks as shown in Figure 5.1.

Still in the interest of repeatability, the head-tracked headset pose is disabled for these tests in favor of a scripted on-rails camera pose that follows a simple circular pattern for its virtual position and another one for rotation, both based on the sine and cosine of the number of frames completed since the first rendered frame. This gives a simple and arbitrarily repeatable pattern resulting in the same camera position and angle at the same frame count for each run, obviously making it much easier to match measurements.

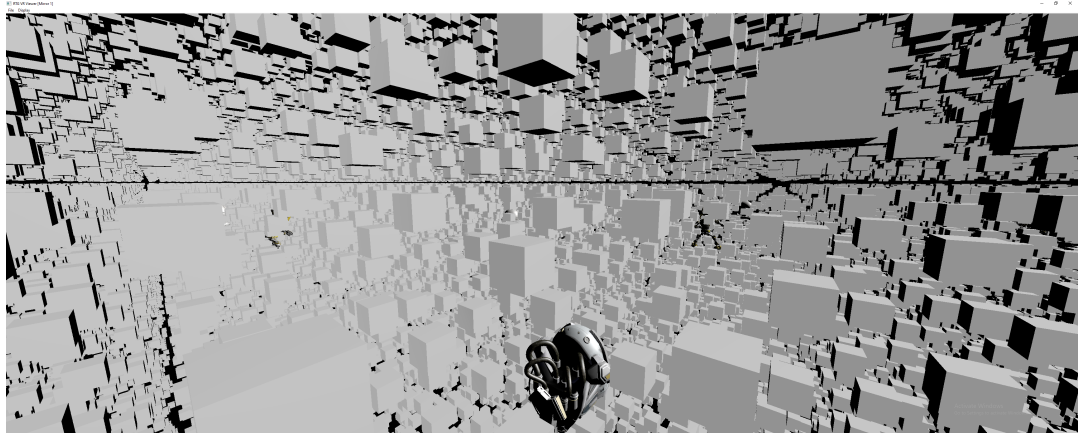


Figure 5.1: Sample scene with high object density, far draw distance and high degree of overdraw when rendered without per-frame Z ordering, screenshot taken of Tachyon's desktop viewport (repetition of Figure 3.2)

## 5.2 Timing code & metrics

To get an accurate idea of how the computational effort within a frame changes and is split up over its several steps, `STL::chrono high_resolution_clock` timings calls were used in strategic places. For each frame, the measured metrics are:

- total frame-time (microseconds)
- CPU-only time (microseconds)

- Culling-only time (microseconds)
- GPU-only time (microseconds)
- number of draw calls submitted
- number of triangles submitted through draw calls

Times are measured by calculating elapsed counts between start and end time points of the respective function call. GPU-only time is measured by artificially placing a `VkQueueWaitIdle(graphicsQueue)` at the end of the `VKRenderer::RenderFrame` procedure. At first glance this seems counter-productive as it prevents frames from overlapping resource usage, but this is where synthetic repeatability becomes relevant.

To guarantee runs with different optimizations enabled can be compared to each other, the render loop is modified to follow aforementioned camera pattern and save the current frame number with each data point. This obviously flies in the face of desired real-world decoupling of motion from framerate and overlapping execution, but it ensures identical workload per frame for each tested configuration. Additionally, the camera pattern and timings loops are tuned to run exactly twice in exactly 5400 frames each for 10 loops. The resulting 54000 samples of frame data for each configuration are then filtered to exclude the worst outliers and the 10 loops are averaged into one representative set of 5400 data points. The very first frame of the averaged data sets is removed as the very first frame of the first loop after program start includes all initialization commands and major buffer transfers and thus results in an outlier frame time an order of magnitude higher than the remaining 53999 frames of each run.

However in the interest of real-world scaling, a later section will also briefly explore average frametimes for a selection of configurations without these limits in place.

Lastly, and this part is crucial, the `Submit()` calls to SteamVR are disabled for the testing runs as these calls otherwise force vertical refresh synchronization (Figure 5.2), completely distorting actual performance numbers. While this means during benchmarking there is no output to the connected HMD, the internal rendering loop still uses all of the HMD's rendering parameters and more importantly renders as many frames as it can without a framerate cap or refresh synchronization, exactly the behavior we need for accurate measurements.

### 5.3 Compilation parameters

Naturally productive deployment would go for fastest possible optimization and as such the tested configurations were all compiled with `-O2` in Release mode using Microsoft Visual Studio 2015 and its v140 MSVC toolset. To further eliminate potential slowdown from branching or data tracking, each of the 16 permutations of enabled optimizations is not done simply through `if` statements or `switch` cases, but through preprocessor defines. These defines are `SUPERFRUSTUM_ON`, `MULTIVIEW_ON`, `STENCILMASK_ON`, `MFFR_ON`. Similarly, benchmark timing code is enabled via the `BENCHMARK_MEASURE`, `BENCHMARK_CHUNKINFO` and `BENCHMARK_CAMRAILS` flags.

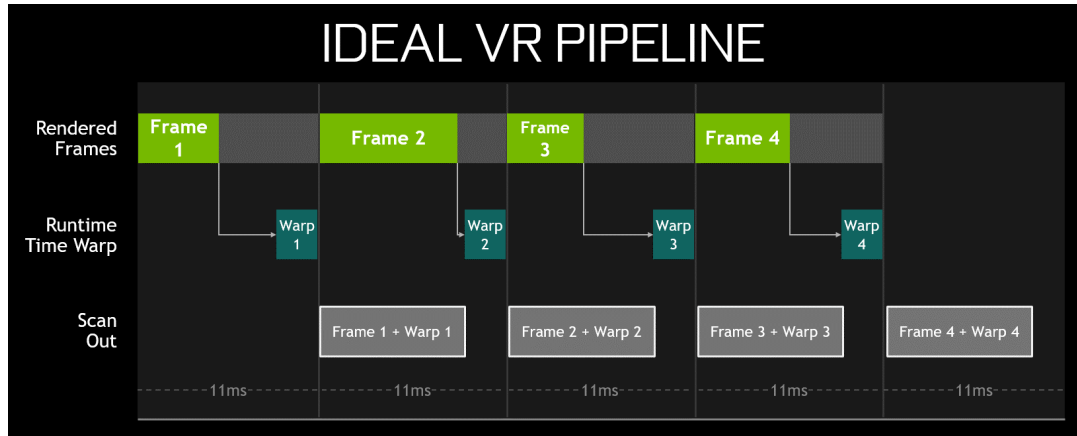


Figure 5.2: Virtual Reality Pipeline as imagined by Nvidia (from [Cle17], p. 35, S. Cleveland. 2017)

As a sidenote here, *all* configurations were tested with distance culling (`DISTANCECULLING_ON`, draw distance 320 units) and frustum culling (`FRUSTUMCULLING_ON`) enabled as running the massive 11.1 million instance scene without these in place would realistically bring any test machine near a grinding halt. It also seems unrealistic to run any scene with advanced VR optimizations enabled but leave such simple measures disabled. Demonstrably, these culling methods are also not posing as dangerous bottlenecks to the tested configurations as the baseline measurement details will show.

## 5.4 System specifications

Two test machines were used to test functionality of the optimizations and to perform measurements on. The first machine, further titled **WS-Big**, is specified as:

- CPU: Intel Core i7 6700 (4c8t Skylake, 4x3.4GHz base, 4.0GHz boost)
- RAM: 2x16GB DDR4-2400/15
- GPU: Nvidia GeForce RTX 2080 Founders Edition (2944 Turing cores at 1800MHz core, 8GB GDDR6 at 1750MHz) - driver version 432.00
- Storage: Samsung SSD 840 Evo 500GB
- OS: Microsoft Windows 10 Pro x64 1809

The second machine, further titled **WS-Small**, is specified as:

- CPU: AMD Ryzen 5 1600 12nm (6c12t Zen+, 6x3.2GHz base, 3.7GHz boost)
- RAM: 2x8GB DDR4-3066/14

- GPU: Hewlett-Packard Radeon RX 580 (2304 Polaris cores at 1200MHz, 4GB GDDR5 at 1750MHz) - driver version 20.1.3
- Storage: ADATA SSD SX6000 Pro 500GB
- OS: Microsoft Windows 10 Pro x64 1909

Furthermore, the following virtual reality headsets were available with the respective internal per-eye resolution setting and in the respective capacity:

- Valve Index (2016x2240 pixels) - **WS-Big** performance measurements, functionality verification
- HTC Vive (1512x1680 pixels) - **WS-Big** functionality verification
- HTC Vive Pro (2016x2240 pixels) - **WS-Big** functionality verification
- Oculus Rift CV1 (1344x1600 pixels) - **WS-Big & WS-Small** functionality verification
- Samsung Odyssey (1449x1797 pixels) - **WS-Small** functionality verification

To ensure repeatability and level the field as much as possible, the CPU of each system is locked to a fixed clock multiplier and thus operating frequency. For the i7 6700 and its lack of unlocked multiplier this is achieved by setting minimum and maximum processor state in Windows to 100 and 99% respectively, which effectively disables singlecore turbo boost and speedshift and fixates the frequency at the allcore boost multiplier of 37x for 3.7GHz allcore. For the Ryzen 5 1600 a more reliable method is available, that being manually overriding the CPU multiplier within the mainboard UEFI, in this case to a fixed value of 38x for 3.8GHz across all 12 processor threads.

Keeping GPU clock speeds at the same level for all test runs is harder to achieve as all modern graphics cards employ some version of dynamic boosting algorithms based on temperature, power target, voltage target and usage. The Radeon RX 580 is set to target a maximum of 1200MHz boost frequency via a VBIOS modification that disables higher automatic boost, and during core load it maintains this target stable unless the power target of 100 Watts is exceeded. For Nvidia graphics cards later than 2014's Maxwell 2 architecture, such a firmware mod is unfortunately not possible. There is, however, one way of reaching a mostly stable core frequency. To achieve this, the card needs to be pre-heated using any application generating GPU load. To prime **WS-Big**'s RTX 2080, SteamVR Home is idled for 30 minutes before any test runs are performed, resulting in an equilibrium of 70°C at 1905MHz core frequency. This temperature and frequency is maintained for the entirety of each test run as the 210 Watts power target of the card is never exceeded.

## 6 Performance benchmark results

Testing each combination of *ON* and *OFF* states of the four optimizations logically yields 16 permutations. This chapter aims to show the metrics declared in section 5.2 for each permutation and explore causes and implications for those permutations that would reasonably be employed in an application. The following results are measured on **WS-Big** unless otherwise specified. Figures and tables may refer to Multiview as *MVIEW*, to Stencil Masking as *SMASK*, to Superfrustum Culling as *SFRUST* and to Monoscopic Far-Field Rendering as *MFFR*.

The plot of draw call count submissions during the test run looks as Figure 6.1 and is identical for every subsequent test using the respective optimization due to the synthetic construction of the benchmark. Thus any otherwise observed performance impact barring error margins stems from changes in execution approach owing to active optimizations. Draw call lists in *rtvklip* are built during frustum culling and as such should only change with the number of frusta used, meaning there are differences in draw call count expected between Superfrustum *ON* and *OFF* and MFFR *ON* and *OFF*. Superfrustum roughly halves draw call count compared to baseline which is expected considering each eye uses the same draw call list instead of separate and slightly different lists. MFFR differences are explored in section 6.1 as they do not follow expectations.

### Baseline

To get a frame of reference for any potential performance improvement - or degradation - a baseline measurement is necessary, meaning a set of data points with all four optimizations set to *OFF*. This baseline as measured on **WS-Big** is shown in Figure 6.2). While these performance numbers were recorded, the sensors of the RTX 2080 and i7 6700 were monitored using the tool *HWINFO64*. For the duration of the baseline test, this tool attests utilization averages of 80% for the GPU core, 37% memory capacity, 32% for the GPU memory controller and 20% for the PCIe bus link. For the CPU an overall average utilization of 49% with each of the 8 threads averaging between 30-40% was seen. RAM usage from asset load at program start up until termination reported 5.4GB for the application by itself.

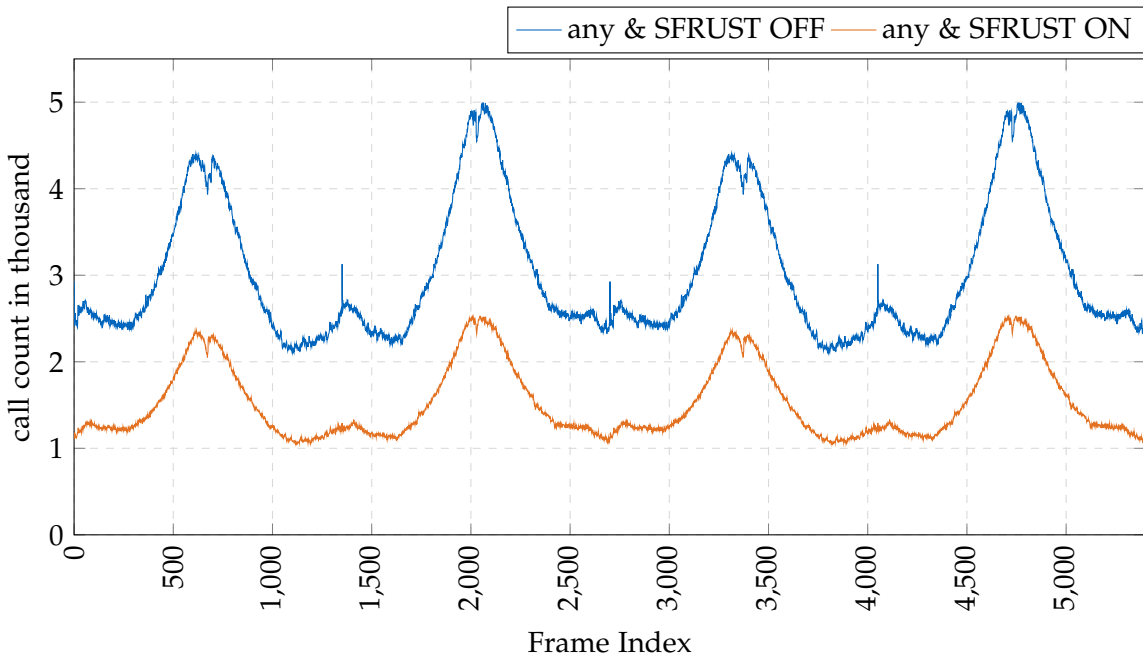


Figure 6.1: draw call count per frame

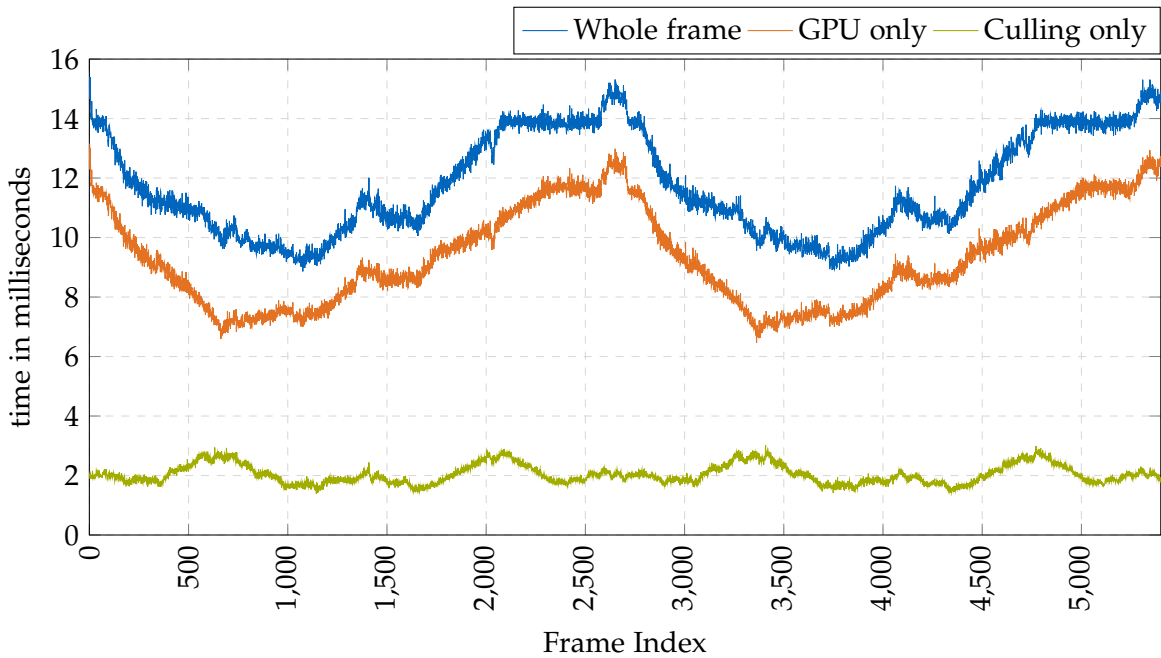


Figure 6.2: baseline/all OFF performance (10 run average)

## 6.1 Individual impact

Looking at the performance of each individual optimization by itself gives an idea of potential bottlenecks and a good reference for each metric to refer back to in the comparisons and more detailed discussion in subsection 6.1.1.

Starting with Stencil Mask performance in Figure 6.3, no particular outliers can be noticed. On the contrary, the GPU- and frametime lines appear even a little smoother, specifically around frames 2100-2300 and 5300 onward, suggesting the worst frametimes of the baseline plot are primarily pixel shader bound.

Continuing with Superfrustum performance in Figure 6.4, no particular outliers can be noticed again.

Stereo Multiview performance in Figure 6.5 hints at significant performance savings as overall frametimes are noticeably lower and framepacing tighter than in the baseline.

Finally Monoscopic Far-Field Rendering returns the problematic numbers in Figure 6.6 as already hinted at in subsection 4.3.5. It is immediately evident that MFFR has severe issues with both overall performance and framepacing alike. In regular intervals of about 700 frames, GPU times rapidly fluctuate between 7 and 20 milliseconds for about 700 frames and then remain at high levels around 15 to 20 milliseconds again. The brief dips down below 10 milliseconds would be the expected performance of MFFR given the large number of far-field geometry in the test scene. This would suggest much higher shader load than the baseline configuration and is in line with the discussed overdraw issue, but does not explain the observed fluctuations completely. Unexpectedly, even culling time irregularly spikes upward over the time of the benchmark loop. This comes as a surprise and indicates the rtvklb frustum culling implementation suffers from a yet unexplored difficulty when handling that additional frustum. Once draw call count for MFFR is included as a comparison (Figure 6.7), it is clear that the steep variation directly correlates with the number of draw calls issued in a given frame. The only feasible explanation at this time is that the culling procedure incorrectly constructs the result sets leading to significant changes in per-frame load in these ranges. This does not, however, explain the higher overall frametimes outside of these fluctuations, which instead are most likely attributed to the enforced sequential synchronization of the used far-first MFFR approach. This hypothesis is supported by power draw sensor monitoring in HWiINFO64 during MFFR runs, which saw the figure at only around 140-150 Watts compared to the 170-180 Watts observed in all other tests despite all tests consistently reporting back with 80-81% GPU core usage. Considering these performance issues persist in every configuration including MFFR ON and negates any otherwise gained savings in these cases, all 8 of these MFFR configurations are omitted from further analysis. HWiINFO64 monitoring values for most of the presented configurations proved uneventful and mostly followed baseline numbers within error. There are two exceptions to this, however. While baseline monitoring sat at 20% average bus load, any case with MFFR enabled saw a drop of about 3-4 percentage points in this metric, any case with Multiview enabled saw another 8 percentage point bus load reduction. Additionally, the two cases with both MFFR and Superfrustum active but Stencil Masking disabled saw yet another drop of 4 percentage points. In other words, enabling Multiview usually resulted in 12% bus load and enabling

MFFR as well resulted in a low 8% bus load. While tangentially interesting, these numbers do not translate well into performance predictions for other systems and applications as too many system-specific factors affect bus load.

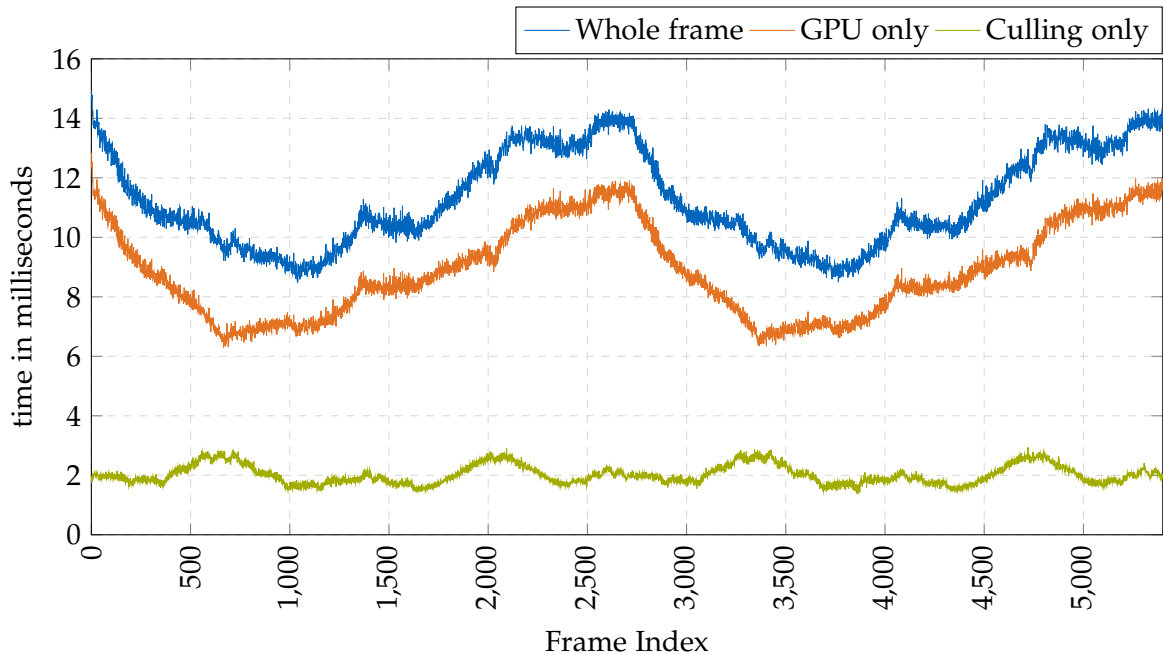


Figure 6.3: SMASK ON performance (10 run average)

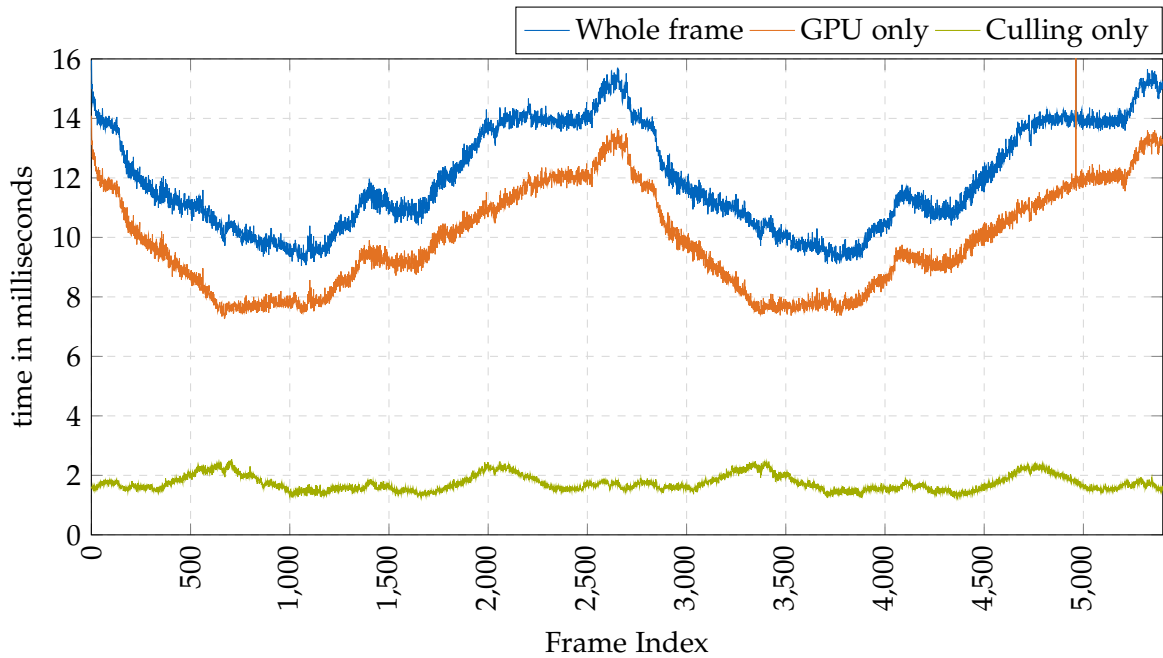


Figure 6.4: SFRUST ON performance (10 run average)

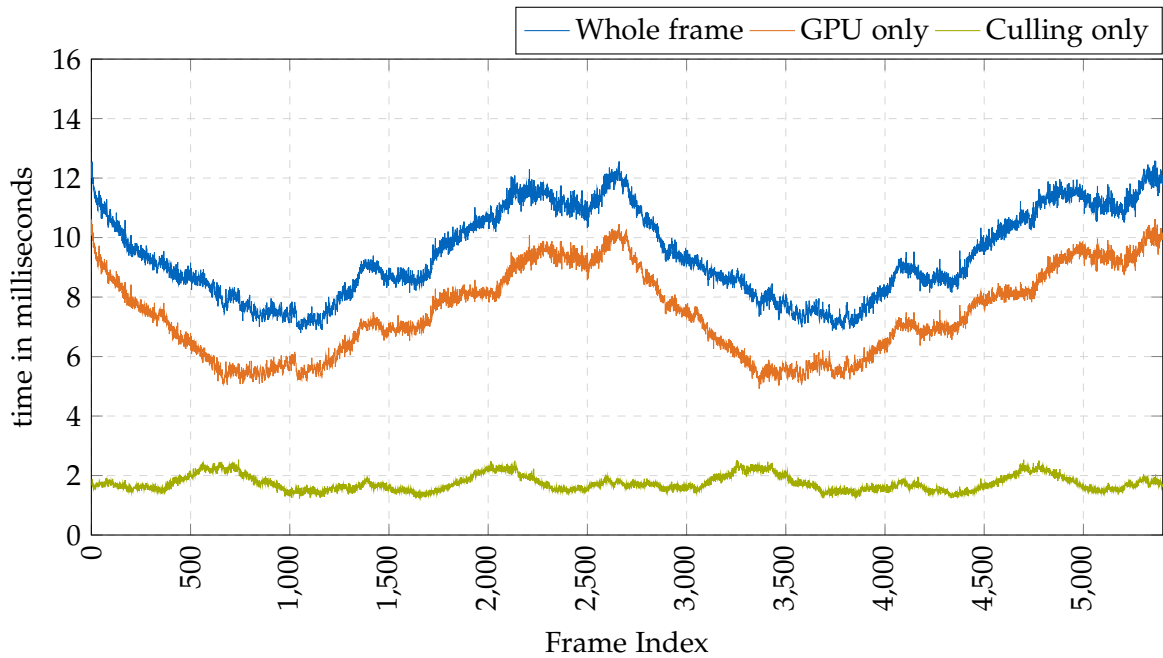


Figure 6.5: MVIEW ON performance (10 run average)

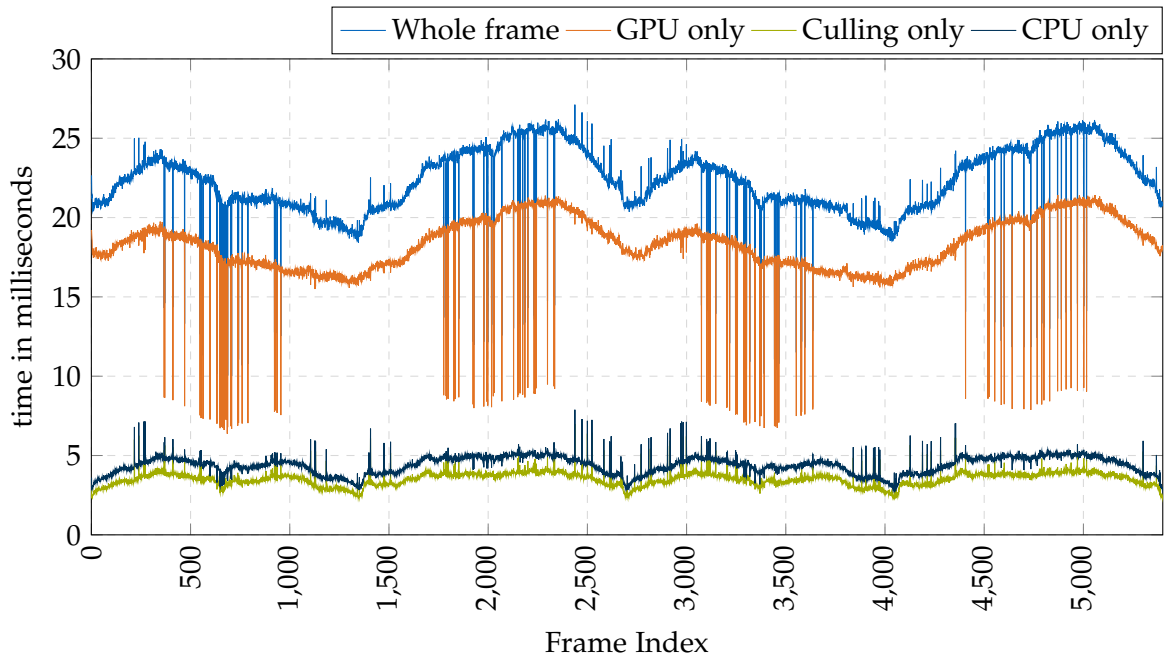


Figure 6.6: MFFR ON performance (10 run average)

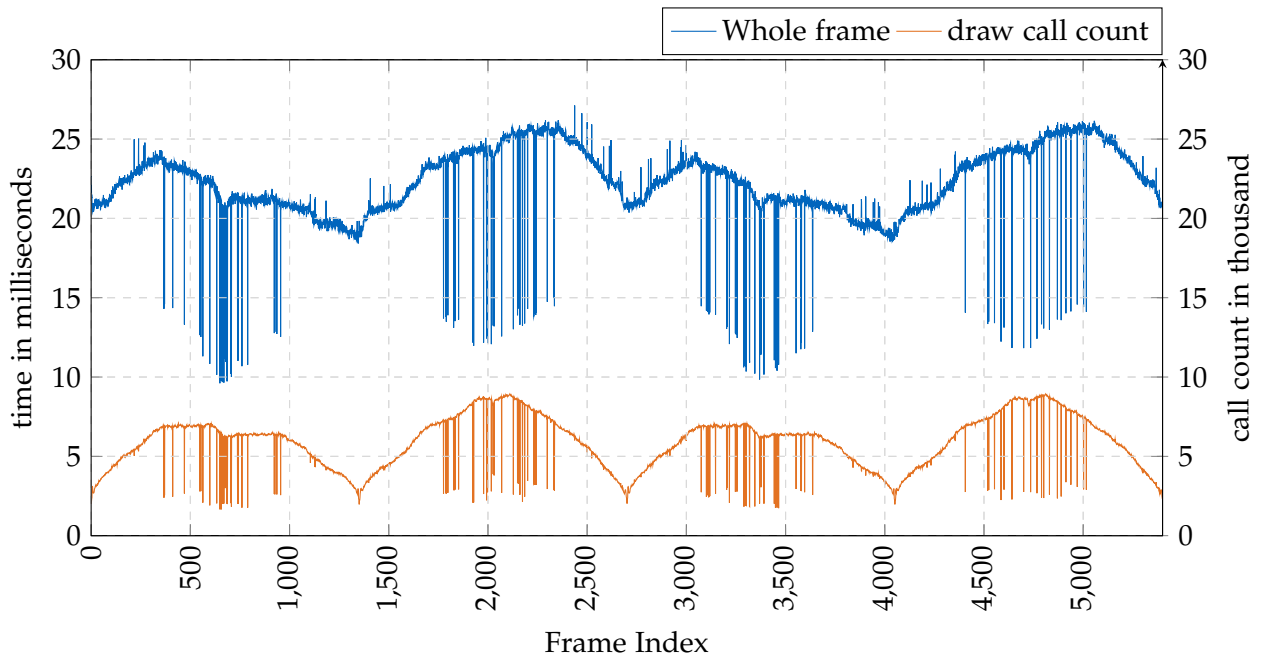


Figure 6.7: MFFR ON whole frame vs draw call count

### 6.1.1 Comparison of individual optimizations

Comparing the individual impacts per metric in one plot each gives a better idea of relative improvements or deterioration. First off, overall frametimes (Figure 6.8) clearly showcase the significant boost gotten when using Stereo Multiview, a 19.2% reduction in median frametime and 19.7% in average frametime as per the numbers in Table 6.1. Stencil Masking shows an appreciable albeit small performance gain as well, due to the particularly optimized fitment of the provided Valve Index mask. Here the median and average gains come out to 4.5% and 4.3%, respectively. The Superfrustum optimization results in a minor performance loss compared to baseline which seems counterintuitive at first. It becomes logical considering that with each eye still rendering individually, each eye now renders a higher load than with separate eye-fitted frusta. As such a Superfrustum the culling time reduction (Figure 6.10) afforded by the Superfrustum is negated by the increased GPU load (Figure 6.11). An overall reduction including Superfrustum use can only be expected when combining its use with Stereo Multiview rendering so the per-eye surplus in draw calls is again negated by a reduction in command submission time. An interesting effect on CPU and cull time can be observed for the Superfrustum and Multiview cases. While a CPU load reduction for Multiview is expected as it cuts down on command submissions, it is unexpected that it performs any better in cull time. But as Figure 6.10 clearly shows, Multiview leads to similar cull time savings as the Superfrustum. A retrospective look at the culling procedure of `rtvklip` delivers an explanation. In an effort to fairly optimize dual frusta culling for Multiview rendering, the two eye frusta both write their resulting calls into the same output set. To avoid duplicate entries in that set and because it seemed illogical to check both frusta, when an `INSIDE` or `INTERSECT` frustum check for the first frustum is returned, the cell's draw command is added to the output set and as the second frustum's check would not change this command, it is not performed. Inadvertently this means the implemented Multiview path performs a form of frustum culling that approaches Superfrustum performance when the eye frusta have a high percentage of overlap. In addition the tested system's Nvidia RTX 2080 graphics card supports hardware accelerated geometry reprojection for multiview rendering, which noticeably cuts down GPU render time in the test scene with its generous numbers of 3D objects present. On a purely software based multiview GPU, only the reduction in overall CPU time is expected as depicted in Figure 6.12 which still shows non-culling CPU time - in this case comprised mostly of command buffer building and command submission - is almost halved. Effectively this means Multiview performs better here than all other individual optimizations not just in GPU time but also in CPU time and is almost on par with the Superfrustum in cull time.

As a sidenote, Table 6.1 demonstrates that the presented benchmark data includes little skew as median and arithmetic mean values show no large differences and verifies again that the plotted frame data has no major outliers for any cases not involving MFFR.

Table 6.1: Median and average (arithmetic mean) timings for frametime, gpu-time and cull-time for baseline and individual optimizations in milliseconds (rounded to two decimal places)

Config	frame		gpu		cull	
	median	avg	median	avg	median	avg
baseline	11.29	11.75	9.06	9.36	1.97	2.04
SMASK	10.78	11.24	8.63	8.88	1.95	2.02
SFRUST	11.49	11.96	9.59	9.88	1.67	1.74
MVIEW	9.12	9.43	7.31	7.46	1.68	1.74

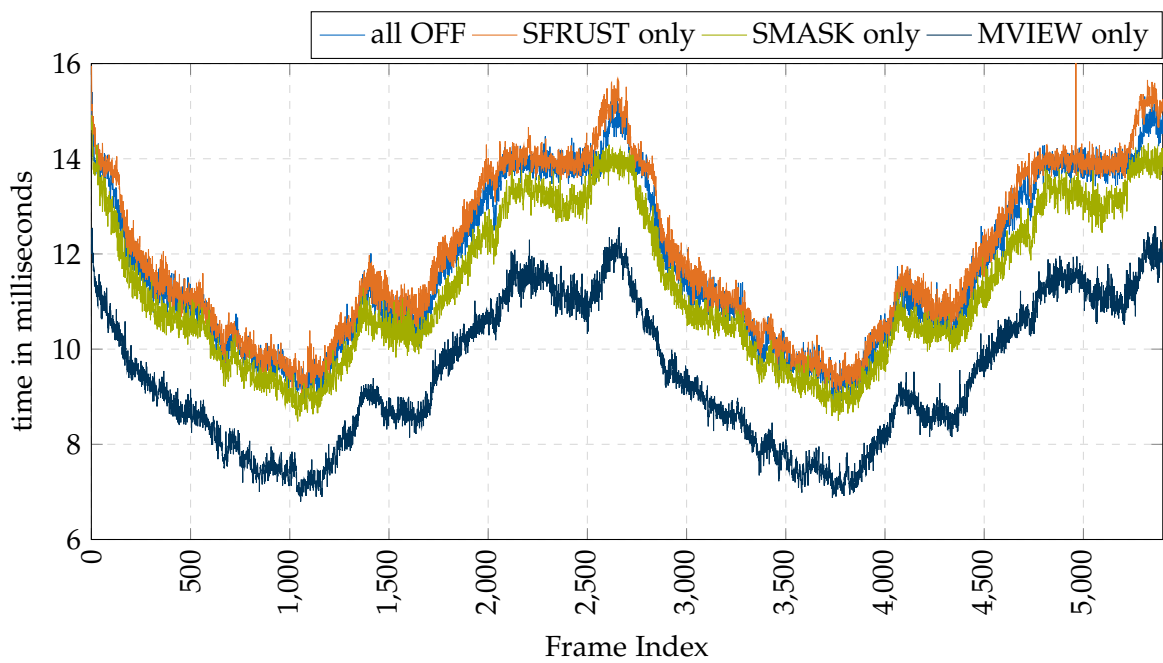


Figure 6.8: comparison (Whole frame time)

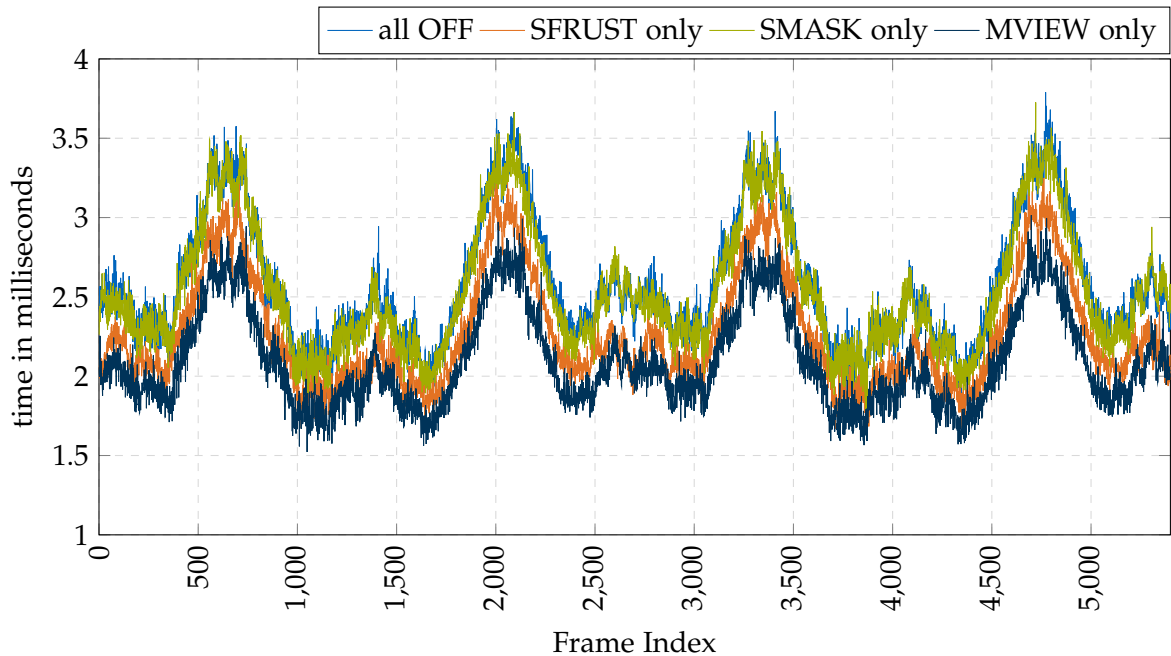


Figure 6.9: comparison (CPU time)

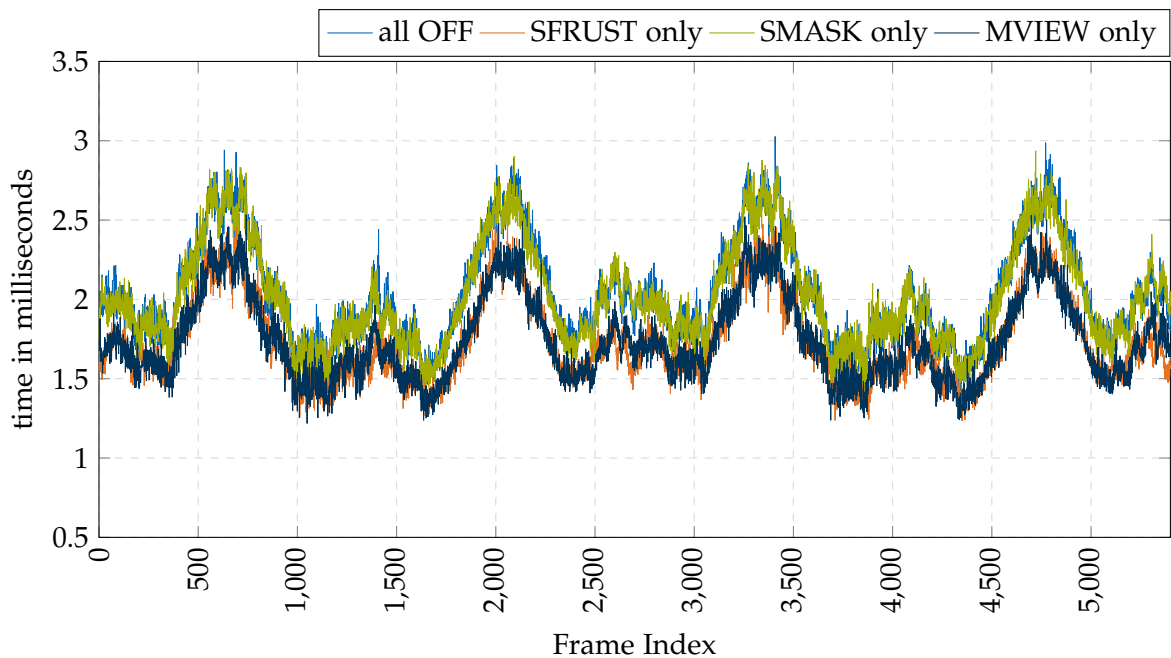


Figure 6.10: comparison (Cull time)

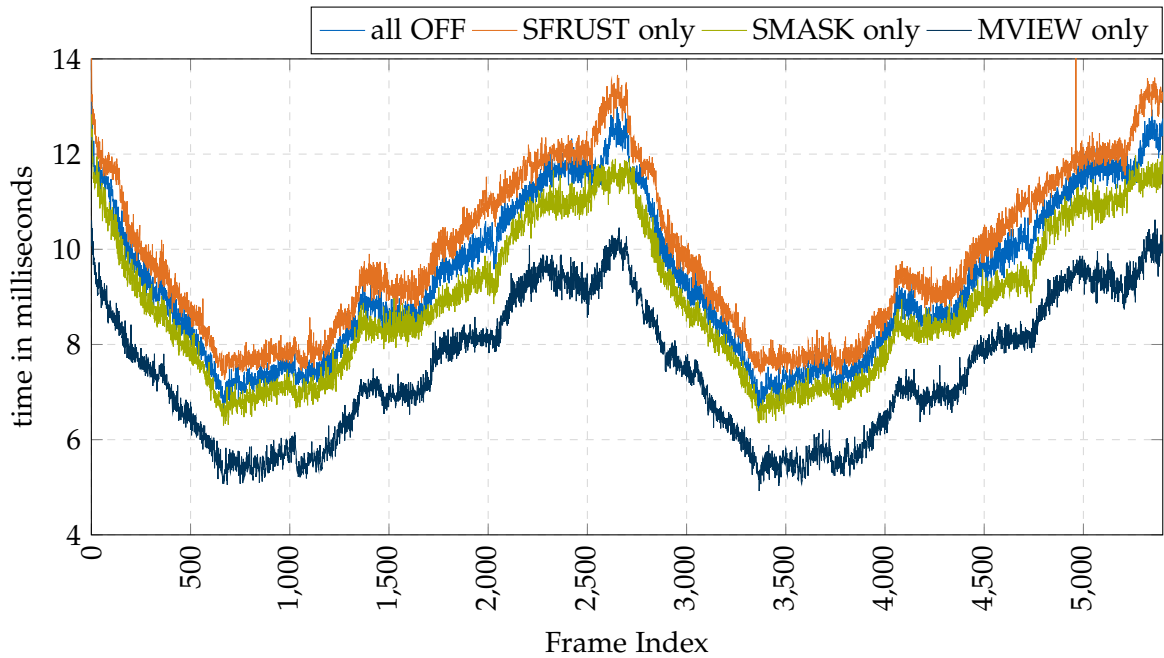


Figure 6.11: comparison (GPU time)

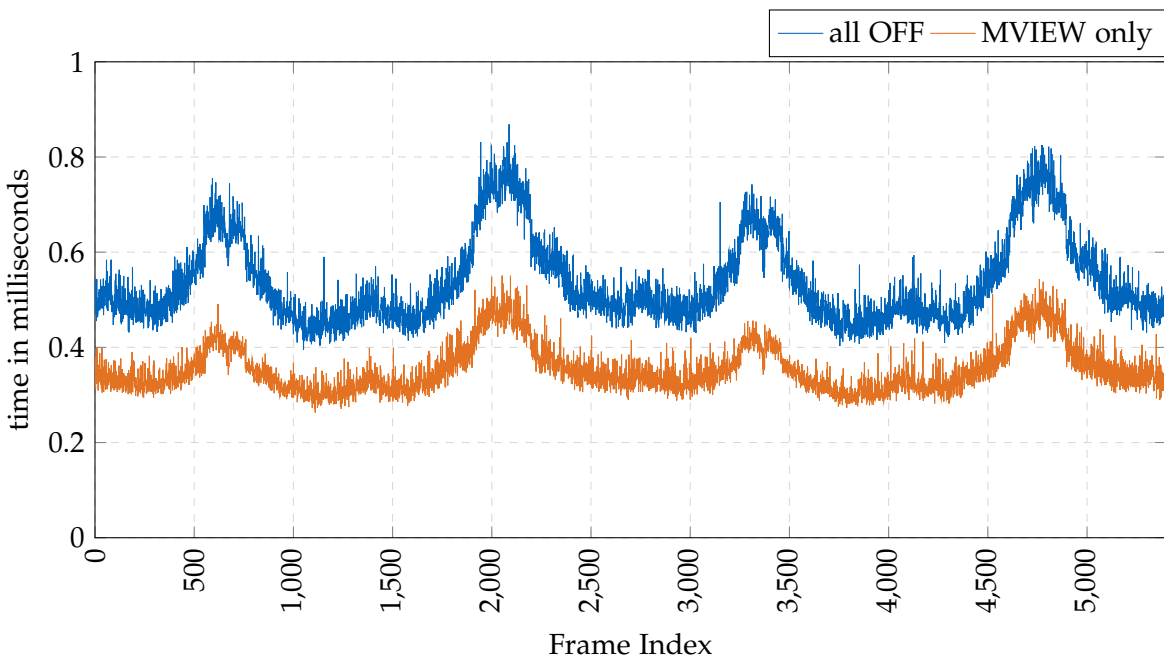


Figure 6.12: baseline vs MVIEW (CPU sans cull time)

## 6.2 Combined impact

Next, the possible combination of multiple optimizations is examined. Similar to the individual benchmarks, Stencil Masking tightens framepacing by a small margin (Figure 6.13 & Figure 6.14) while Superfrustum use cancels out its CPU gains. Unless, that is, the Superfrustum is combined with Multiview rendering in Figure 6.15, in which case it results in a minor reduction in cull time barely beating Multiview's own multi-frustum optimization. The two configurations of Stereo Multiview with Stencil Masking and either Superfrustum *ON* or *OFF* (Figure 6.14 & Figure 6.16) showcase the greatest promise in overall frame time and GPU render time.

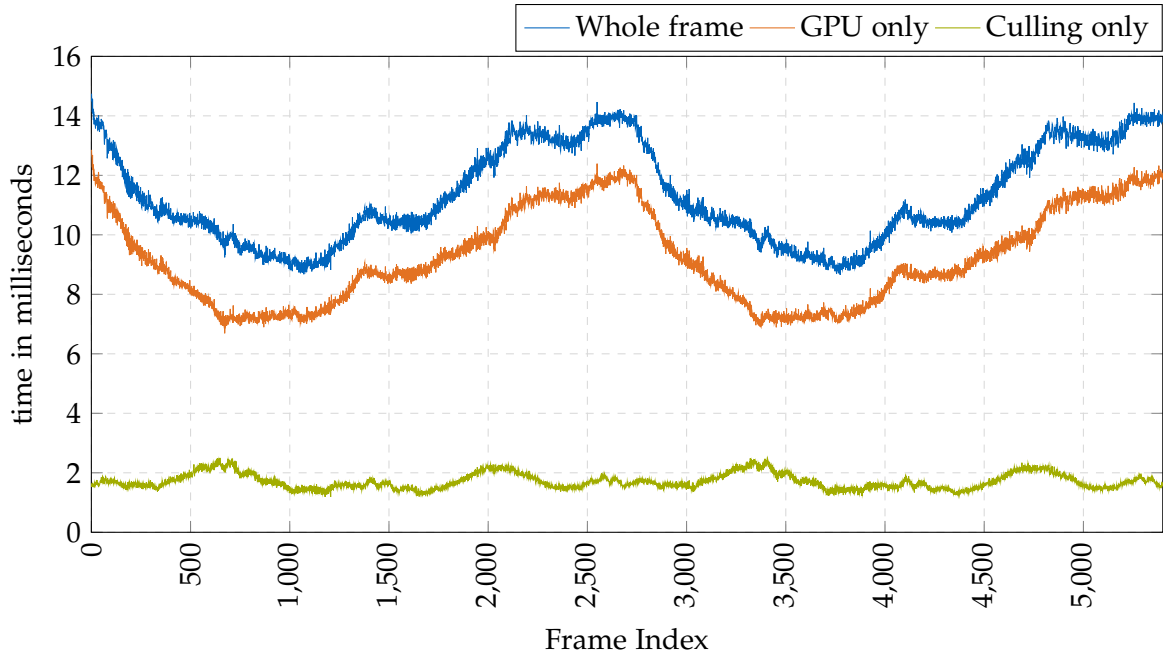


Figure 6.13: SMASK & SFRUST ON performance (10 run average)

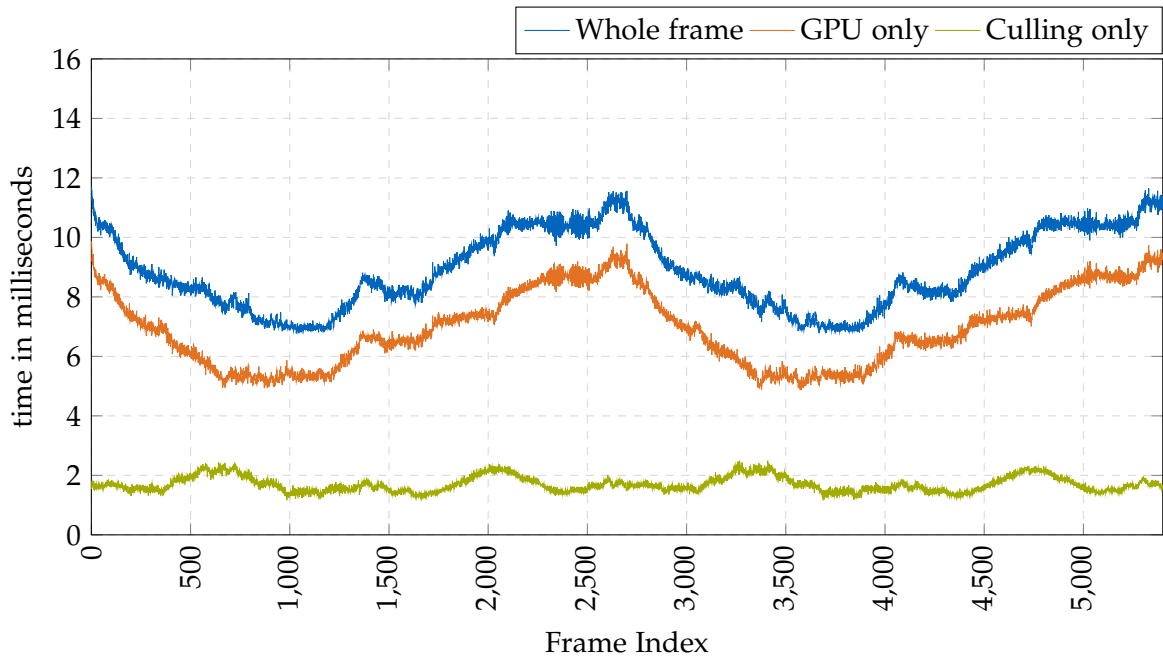


Figure 6.14: SMASK & MVIEW ON performance (10 run average)

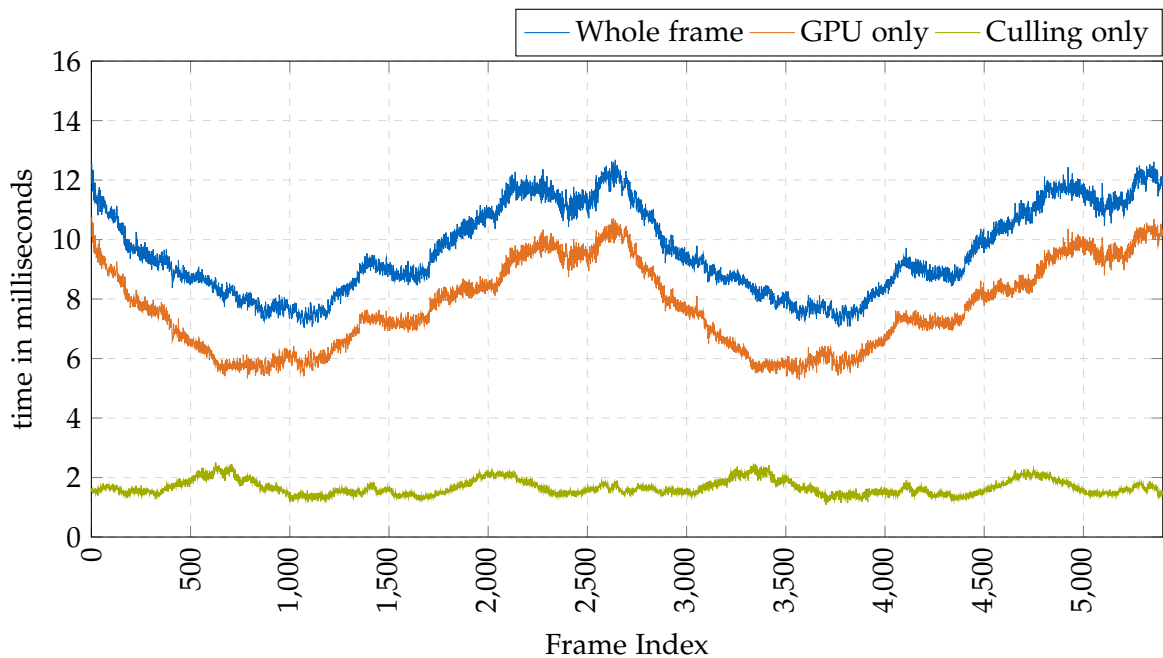


Figure 6.15: SFRUST & MVIEW ON performance (10 run average)

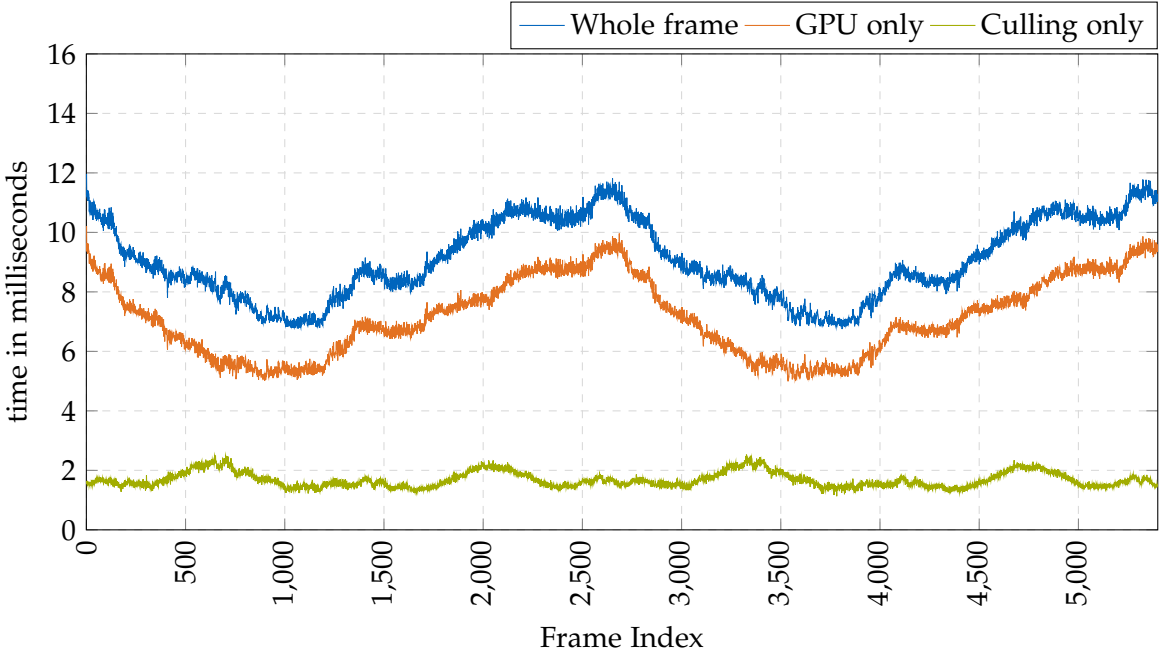


Figure 6.16: SMASK & SFRUST & MVIEW ON performance (10 run average)

### 6.2.1 Comparison of combined optimizations

To get an even better understanding of how each of these four configurations stack up against each other and against the baseline, another set of comparison plots is examined. Due to the established negative impact on GPU times of Superfrustum use without Multiview rendering, the combination of Stencil Masking and Superfrustum just barely outperforms the baseline overall (Figure 6.17), by a lower margin (median 4.3% and avg 3.8% vs 4.5% and 4.3%) than Stencil Masking on its own. Any combination involving Stereo Multiview leads to significant improvement as expected. Interestingly, however, combining Multiview with the Superfrustum performs worse compared to just Multiview on its own by a small margin (Figure 6.21).

When it comes to best overall performance, the combinations of Multiview with Stencil Masking and of Multiview with Stencil Masking and Superfrustum are close together, but the former surprisingly comes out ahead by a small margin. It appears the small amount of blind volume of the Superfrustum compared to the separate frusta affords a small advantage in cull time but trades it for a minor increase in GPU rendering load. CPU time benchmarks in Figure 6.18 mirror the results already seen for the individual impacts with Superfrustum improving on the baseline by a noticeable margin and any Multiview configuration extending this lead even more. Cull time also shows a similar story to subsection 6.1.1 with Superfrustum and Multiview configurations being effectively on par, underlined by the near-identical cull time medians/averages in Table 6.2. The combination of Superfrustum with Multiview yields another minuscule cull time improvement but once more trades it for increased GPU

rendering load as seen in Figure 6.20.

As such, the configuration of Stereo Multiview *ON*, Stencil Masking *ON*, Superfrustum *OFF* and MFFR *OFF* performs the best on the used machine with a median frametime reduction of 23.7% and average reduction of 24.4%. Expressed inversely as framerate, this equals a boost from 88.57fps median and 85.11fps average to 116.14fps (+31.1%) and 112.61fps (+32.3%) respectively.

Considering all these results, the most viable optimizations to employ are as follows:

- Stencil Masking (SMASK) lends itself as a quickly implemented and lightweight way of gaining a moderate pixel shader performance boost, only requiring a single 8 bit framebuffer layer per eye at most
- Stereo Multiview (MVIEW), while reliant on GPU and API support and thus only available on more recent architectures - and only accelerated in hardware on very modern chipsets such as the RTX 2080 used here - , can yield significant gains with little to no other significant tradeoff
- Stereo Multiview and Stencil Masking naturally promises to be a synergetic combination of approaches with no major downside
- Stereo Multiview and Superfrustum (SFRUST) Culling can be combined for good results, but may only scale favorably if the target system is constrained in culling performance so the savings afforded by the Superfrustum outweigh the slight increase in GPU load
- Combining all three of these optimizations is subject to the same restriction as Multiview plus Superfrustum but the addition of Stencil Masking in this case can regain if not overcome the Superfrustum GPU performance loss

Other optimization combinations presented up to this point are either non-sensical such as Superfrustum Culling without Multiview acceleration which results in too high a loss in GPU performance or are functionally defective in the case of MFFR combinations in the state implemented for this thesis. However, further work and improvement on the latter is expected to return positive gains given adequate virtual environments.

Table 6.2: Median and average (arithmetic mean) timings for frametime, gpu-time and cull-time for baseline and combined optimizations in milliseconds (rounded to two decimal places)

Config	frame		gpu		cull	
	median	avg	median	avg	median	avg
baseline	11.29	11.75	9.06	9.36	1.97	2.04
SMASK & SFRUST	10.80	11.30	8.93	9.25	1.66	1.72
SMASK & MVIEW	8.61	8.88	6.84	6.95	1.65	1.70
SFRUST & MVIEW	9.30	9.62	7.54	7.72	1.60	1.66
SMASK & SFRUST & MVIEW	8.80	9.07	7.05	7.15	1.62	1.69

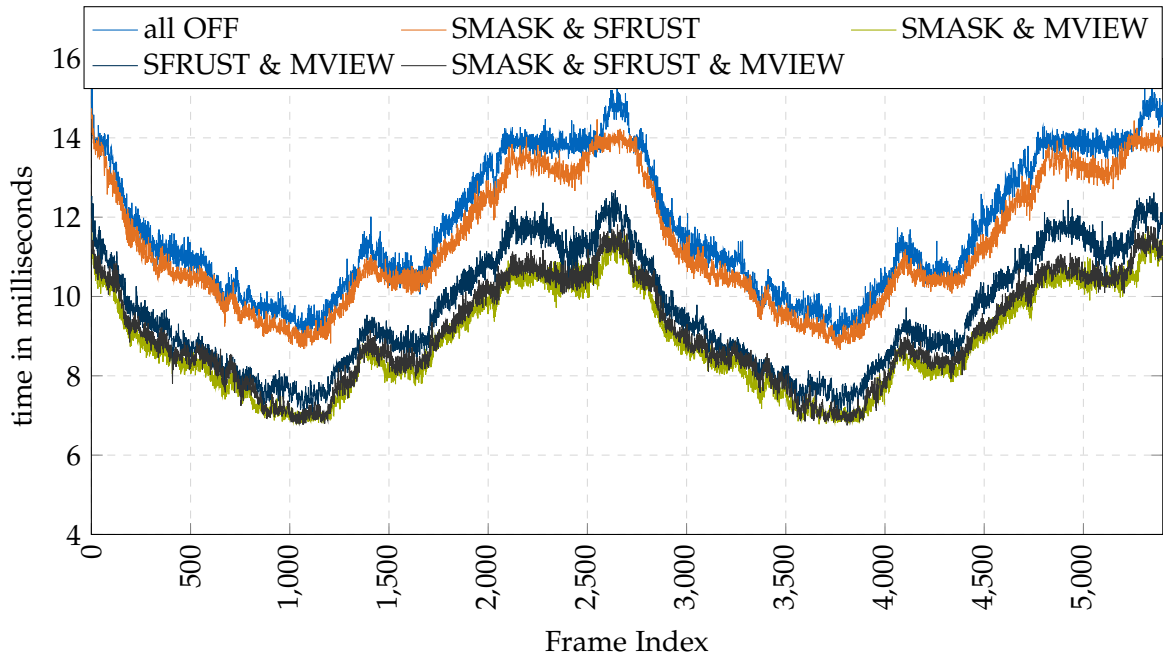


Figure 6.17: comparison (Whole frame time)

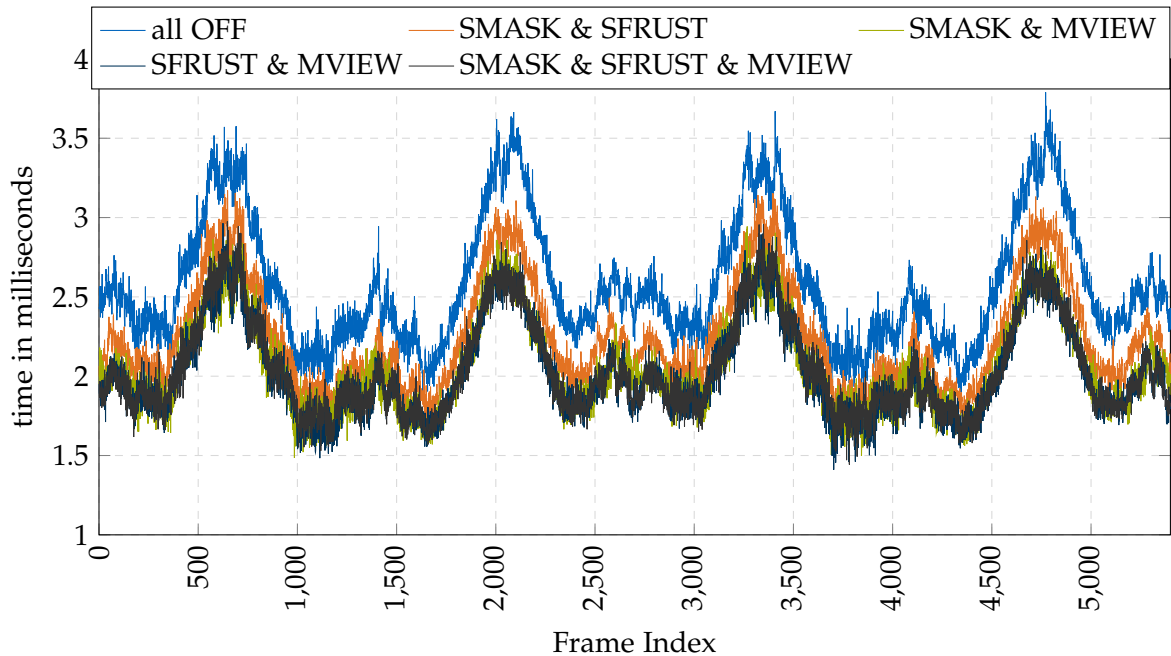


Figure 6.18: comparison (CPU time)

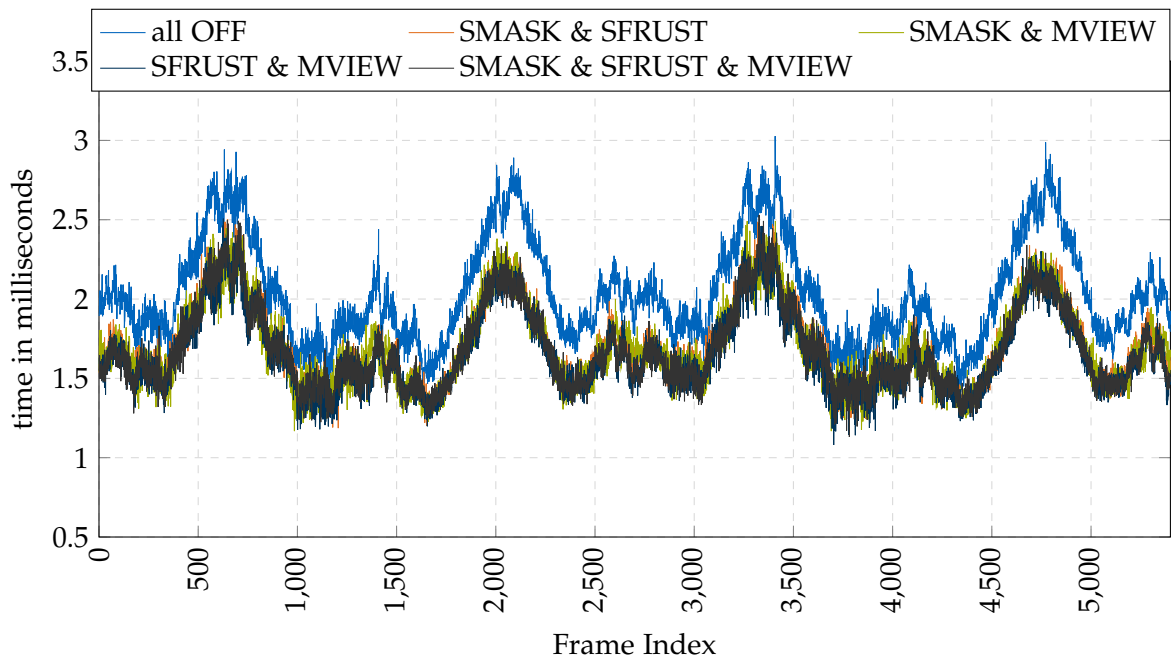


Figure 6.19: comparison (Cull time)

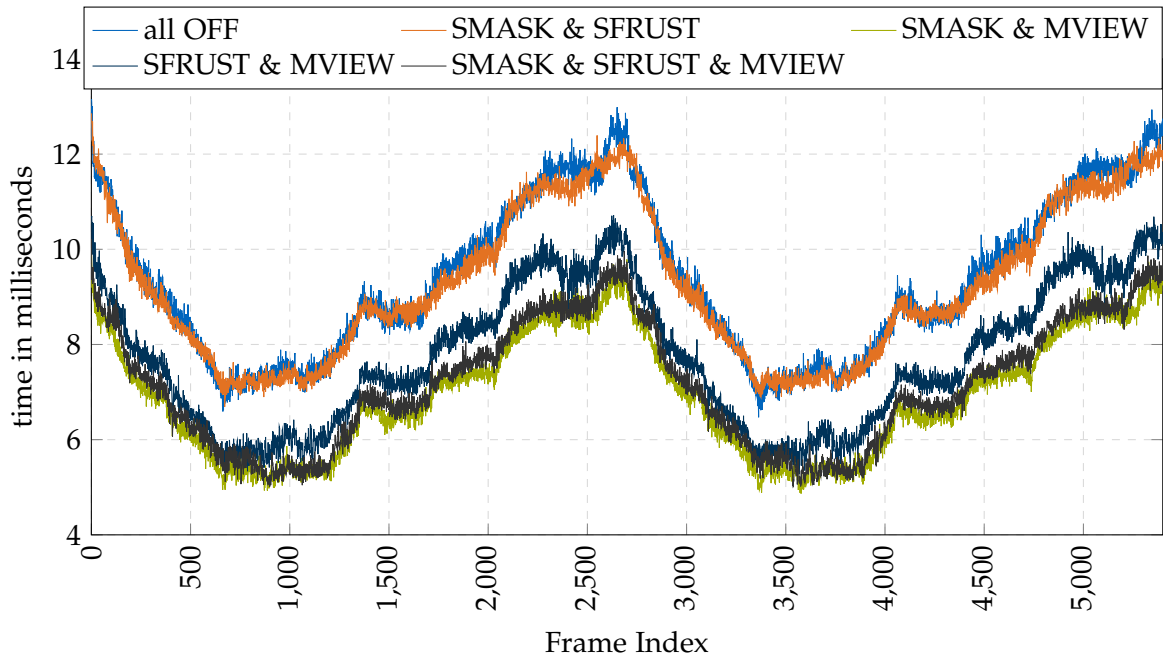


Figure 6.20: comparison (GPU time)

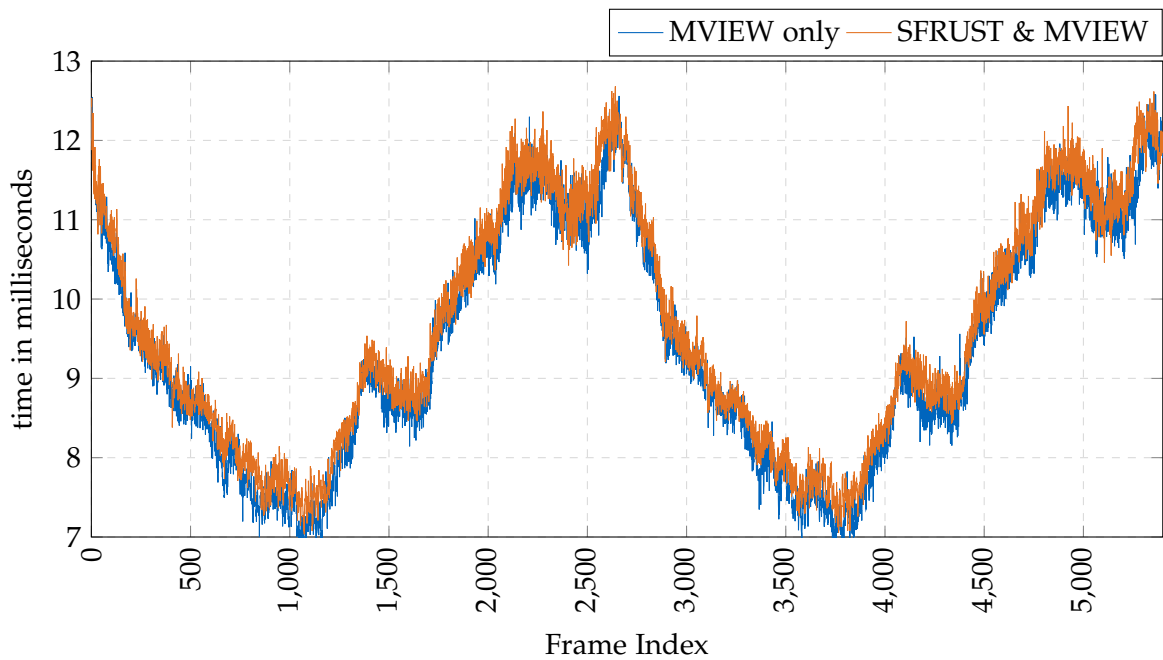


Figure 6.21: MVVIEW only vs SFRUST & MVVIEW (Whole frame time)

### 6.3 Viable Combinations Comparison

#### 6 Performance benchmark results

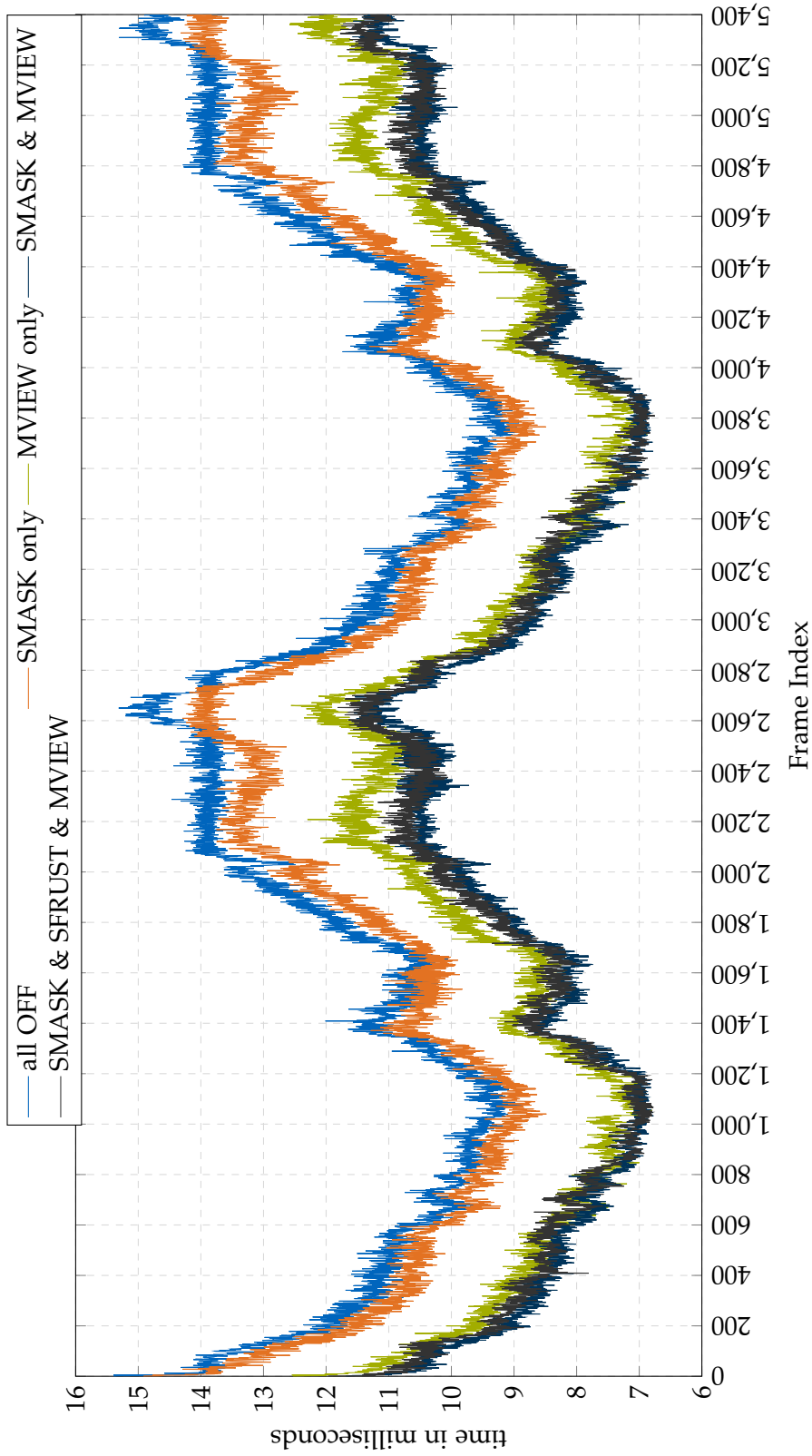


Figure 6.22: Best candidates comparison (Whole frame time, excluding MFRR and most SFRUST configurations due to their negative scaling)

## 6.4 Memory Usage

Previously in this thesis for examination of various frame-internal buffers, layers and matrices, Nvidia's Nsight (Visual Studio Edition) allows detailed inspection of almost all runtime information related to a frame's command composition over time and the settings and buffers involved in each command or *event*, as the tool calls it. Nsight was used to read out and briefly discuss the effect of the various optimizations on video memory usage (Figure 6.23). It is, after all, of interest whether any one optimization may easily overflow the VRAM capacity of a particular graphics card. For the baseline (all *OFF*) configuration, the following resources are allocated:

Table 6.3: VRAM usage of baseline (all *OFF*) test configuration

Resource (No. units)	memory	
	footprint	type
Color Buffer	137.81 MB	(RGBA8 4xSample, 2 layers of 2016x2240)
Depth Buffer	139.58 MB	(D32, 2 layers of 2016x2240)
Resolve Image (2x)	17.72MB	(RGBA8, 1 layer of 2016x2240)
Asset Textures (11x)	21.33MB	(RGBA8, 1 layer of 2048x2048)
Env. Textures	16.03MB	(RGBA16, 6 layers of 512x512)
Env. Textures	528.0 KB	(RGBA32, 6 layers of 64x64)
PBR Reference	1024.0 KB	(RG16, 1 layer of 512x512)
Index Buffer	1.77MB	(cube + high poly assets geometry)
Instance Model Matrices	678.80 MB	(64B per instance)

Another 257.41MB are used for texture and buffer staging but not used every frame thereafter. A buffer for camera matrices and positions takes up 288B. Additionally 1025 small (about 200-220KB) buffers are used at startup, declared as index buffers, but only about 30 are regularly reused in a frame. For each of the listed buffers, textures and images, a `DEVICE_LOCAL` memory pool of the corresponding size resides in the GPU onboard memory, model matrices and staging buffers are created as `HOST_VISIBLE` & `HOST_COHERENT` memory to be synchronized between the CPU RAM and GPU VRAM when changed. Such changes may include object transformation via the respective model matrix or upload of new textures to the GPU.

Upon activation of any optimizations, only one distinct change is observed. When Stencil Masking is enabled, the depth buffer is created with not only the depth bit set but also the stencil bit and its format is changed from a 32bit SFLOAT to a 32bit SFLOAT along with a layer of 8bit UINT. The effect of this change in resource usage is a size increase of the depth buffer from 139.58MB to a combined depth and stencil buffer with a size of 277.39MB. Apart from this, the other three optimizations have negligible effect on video memory utilization. For each frustum afforded or saved by MFFR or the Superfrustum, the camera

## 6 Performance benchmark results

---

parameter buffer is expanded or shrunk by 144B. And for each additional frustum the command buffer increases in size, but the change is not easily measurable as the changed frustum sizes and changing draw lists in each frame lead to more fluctuation in the buffer size.

The preliminary consensus from these limited measurements is that the implemented optimizations have significant impact only on framebuffer size where the worst - and only different - case means a 49% footprint increase for Stencil Masking. The total video memory usage change can thus be considered insignificant as scene resources and assets make up the majority of resources.

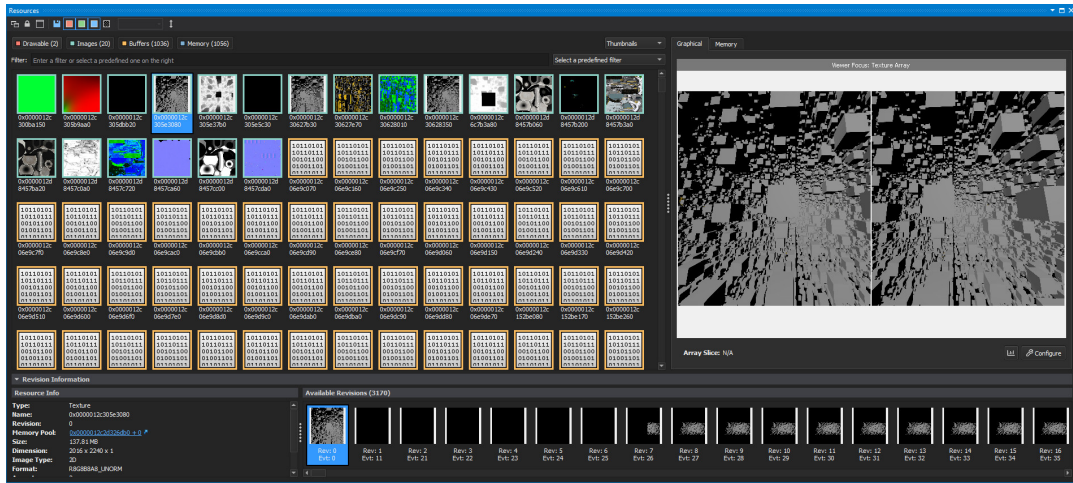


Figure 6.23: Resources tab of a live Nsight VS frame capture for the baseline test configuration

## 7 Outlook

In summary, the goal of this thesis was to gather a selection of optimization methods specifically tailored to VR. Of these methods, a subset was to be implemented in an industrial real-time visualization rendering engine. Finally, these implementations were to be benchmarked in a high stress scenario to asses the performance of each optimization by itself and in conjunction with the remaining methods. This goal sprung from the hope to collect useful information and tangible numbers about ways to speed up VR rendering by a significant margin.

While the list of presented optimization approaches is not exhaustive or complete, as new or more advanced methods are constantly being developed in this field, this thesis does in fact contain an overview of information and elaboration on key avenues. Chapters 3 through 6 cover multiple angles such as GPU versus CPU performance gains, pipeline speedups and varying hardware architectures and their intricacies. The implemented optimizations, while promising, did not all pan out as expected. Stencil Masking and Multiview Rendering show clear and tangible improvements in frametimes and were considered a success. Superfrustum Culling provided a tradeoff to alleviate stress and provide headroom on the CPU in exchange for higher GPU workloads and required fitting circumstances to pay off in a target scenario. Finally, Monoscopic Far-Field Rendering was the most interesting of the concepts presented, but in the practical implementation delivered incorrect and disappointing results.

In the end, valuable insight for deployment of these four optimizations was gained and even MFFR still shows promise given additional iteration and care to iron out the observed issues. It is my hope that the presented approaches and demonstrated results are of similar value to other efforts in the field. After all, every millisecond shaved off is precious in real-time graphics.

# List of Figures

1.1	Comparison of common HMD resolutions (from [Vei19], V. Mäkelä. 2019) . . . . .	2
2.1	VKRenderer's Update() . . . . .	6
2.2	VKRenderer's RenderFrame() . . . . .	6
2.3	VR render target's RecordCommandBuffers(...) . . . . .	7
2.4	VR render target's RenderFrame() . . . . .	7
3.1	SceneChunk's FrustumCull() . . . . .	9
3.2	Sample scene with high object density, far draw distance and high degree of overdraw when rendered without per-frame Z ordering, screenshot taken of Tachyon's desktop viewport . . . . .	10
3.3	Overlap of stereo view frusta (overlap area hatched in red) . . . . .	11
3.4	Symmetric Superfrustum (cropped to geometric construction) (from [Eve15a], C. Everitt. 2015) . . . . .	12
3.5	Non-mirrored superfrustum recession (from [Odd17], V. Oddou. 2017) . . . . .	13
3.6	Point-cone intersection illustration by Hale (from [Hal18], p. 21, J. Hale. 2018)	15
4.1	Simplified graphics pipeline of a modern GPU (from [Ove], A. Overvoorde) .	17
4.2	Simplified flow of standard stereo versus multiview render loops . . . . .	19
4.3	Comparison of rendered rectangular right eye frame after warp versus pixels wasted by lens distortion (from [Vla15], pp. 52-54, A. Vlachos. 2015) . . . . .	22
4.4	Nsight VS capture of stencil buffer as rendered for Valve Index HMD . . . . .	23
4.5	HMD stencil mask query and render flow in rtvklib . . . . .	24
4.6	Material pipeline stencil operation flags . . . . .	24
4.7	Comparison of stencil mask availability (while running SteamVR home) . . . . .	25
4.8	Stencil pipeline stencil operation flags . . . . .	26
4.9	Per-frame render pass flow of far-first MFFR; Each row represents one image buffer, each column represents the process steps the respective buffer is subjected to . . . . .	26
4.10	Per-frame render pass flow of near-first MFFR; Each row represents one image buffer, each column represents the process steps the respective buffer is subjected to . . . . .	28
4.11	Draw submission and render pass binding timeline of a typical rtvklib MFFR frame, captured in Nsight VS. (Split after far-field render pass and stacked vertically for better page fit) On the "Render Pass" row, the blue pass denotes the far-field pass, orange is the left eye and green is the right eye. Far and near are each synchronized by a VkSemaphore. . . . .	30

4.12	Incorrect monoscopic far field distortion (notice the thin center line of distant geometry shifted up and left in the Left Eye image, but shifted down and right in the Right Eye image) . . . . .	31
4.13	Foveated rendering examples . . . . .	34
4.14	Radial Density Masking (2x2 px checkerboard) (from [Vla16], p. 22, A. Vlachos. 2016) . . . . .	35
4.15	Traditional immediate-mode rendering versus tile-based rendering at Nvidia GDC 2017 Editors Day presentation (from [Ngo17], A. Ngo, 2017) . . . . .	36
5.1	Sample scene with high object density, far draw distance and high degree of overdraw when rendered without per-frame Z ordering, screenshot taken of Tachyon’s desktop viewport (repetition of Figure 3.2) . . . . .	38
5.2	Virtual Reality Pipeline as imagined by Nvidia (from [Cle17], p. 35, S. Cleveland. 2017) . . . . .	40
6.1	draw call count per frame . . . . .	43
6.2	baseline/all OFF performance (10 run average) . . . . .	43
6.3	SMASK ON performance (10 run average) . . . . .	45
6.4	SFRUST ON performance (10 run average) . . . . .	46
6.5	MVIEW ON performance (10 run average) . . . . .	46
6.6	MFFR ON performance (10 run average) . . . . .	47
6.7	MFFR ON whole frame vs draw call count . . . . .	47
6.8	comparison (Whole frame time) . . . . .	49
6.9	comparison (CPU time) . . . . .	50
6.10	comparison (Cull time) . . . . .	50
6.11	comparison (GPU time) . . . . .	51
6.12	baseline vs MVIEW (CPU sans cull time) . . . . .	51
6.13	SMASK & SFRUST ON performance (10 run average) . . . . .	52
6.14	SMASK & MVIEW ON performance (10 run average) . . . . .	53
6.15	SFRUST & MVIEW ON performance (10 run average) . . . . .	53
6.16	SMASK & SFRUST & MVIEW ON performance (10 run average) . . . . .	54
6.17	comparison (Whole frame time) . . . . .	56
6.18	comparison (CPU time) . . . . .	57
6.19	comparison (Cull time) . . . . .	57
6.20	comparison (GPU time) . . . . .	58
6.21	MVIEW only vs SFRUST & MVIEW (Whole frame time) . . . . .	58
6.22	Best candidates comparison (Whole frame time, excluding MFFR and most SFRUST configurations due to their negative scaling) . . . . .	59
6.23	<i>Resources</i> tab of a live Nsight VS frame capture for the baseline test configuration	61

# List of Tables

6.1	Median/avg timings for frame/gpu/cull for baseline and individual optimizations . . . . .	49
6.2	Median/avg timings for frame/gpu/cull for baseline and combined optimizations . . . . .	56
6.3	VRAM usage of baseline test configuration . . . . .	60

# Glossary

**HMD** head mounted display; a display headset for mixed reality applications. 1, 5, 7, 23, 25, 30, 32, 37, 62

**MFFR** Monoscopic Far-Field Rendering (see section 4.3). vii, 24–28, 30–32, 44, 45, 47, 55, 62, 63

**Nsight VS** NVIDIA Nsight Visual Studio Edition, a graphics debugging plugin for Microsoft Visual Studio[13]. 22, 23, 30, 62

**Nvidia VRS** Variable Rate Shading, a technology by Nvidia Corporation to decouple raster resolution and shading resolution for geometry[18c]. 33

**OpenVR** VR abstraction API developed by Valve Software. 4–6

**RTG** RTG Echtzeitgraphik GmbH. vi, 3–7, 65

**rtvklib** Vulkan-based rendering library in development at RTG Echtzeitgraphik GmbH, **RTG Vulkan library**. vii, 4, 6, 22, 24, 29–31, 42, 44, 48, 62

**SDE** screen door effect; the observed pixel grid/pitch of a display panel at close distance. 1

**Tachyon** (working title) Real-time visualization engine in development at RTG Echtzeitgraphik GmbH. vi, 3–8, 10, 12–14, 20–23, 27, 29, 30, 62

**VR** virtual reality; a realtime digital simulation mapping the user's movements to immerse them in the virtual environment. 1–7, 14, 20–23, 26, 28, 29, 32, 65

**WMR** Windows Mixed Reality; a moniker for VR headset specifications introduced by Microsoft Corporation. 14

# Bibliography

- [Íñi17] Íñigo Quílez. "Efficient Stereo and VR Rendering". In: *GPU Zen*. Ed. by W. F. Engel. Vol. 1. Encinitas, CA: Black Cat Publishing Inc, 2017, pp. 241–251. ISBN: 9780998822891.
- [Vei19] Veikko Mäkelä. *VR headset resolution per eye comparison (CC BY-SA 4.0)*. 2019. URL: <https://commons.wikimedia.org/w/index.php?curid=82765161>.
- [Vol20] H. Vollmer. *RTG Echtzeitgraphik GmbH Homepage*. 2020. URL: <http://www.echtzeitgraphik.de/>.
- [The16] The Khronos® Group Inc. *Khronos Releases Vulkan 1.0 Specification*. 2016. URL: <https://www.khronos.org/news/press/khronos-releases-vulkan-1-0-specification>.
- [Ant18] Antony Vitillo. *What is Standalone Virtual Reality, and Why Are Enterprises Betting On It?* 2018. URL: <https://www.isaca.org/resources/news-and-trends/isaca-now-blog/2018/what-is-standalone-virtual-reality-and-why-are-enterprises-betting-on-it>.
- [20] IDC - AR & VR Headsets Market Share. 2020. URL: <https://www.idc.com/promo/arvr>.
- [Gri19] L. Gritz. *OpenImageIO*. 2019. URL: <https://github.com/OpenImageIO/oio>.
- [Vla15] A. Vlachos. "GDC2015: Advanced VR Rendering". In: (2015), pp. 51–65. URL: [http://media.steampowered.com/apps/valve/2015/Alex\\_Vlachos\\_Advanced\\_VR\\_Rendering\\_GDC2015.pdf](http://media.steampowered.com/apps/valve/2015/Alex_Vlachos_Advanced_VR_Rendering_GDC2015.pdf).
- [Por17] T. Porter. *VR Optimization Tips from Underminer Studios*. 2017. URL: <https://software.intel.com/en-us/articles/vr-optimization-tips-from-underminer-studios>.
- [Car16] J. Carmack. *Avoiding aliasing in VR*. 2016. URL: [https://www.facebook.com/permalink.php?story\\_fbid=1818885715012604&id=100006735798590](https://www.facebook.com/permalink.php?story_fbid=1818885715012604&id=100006735798590).
- [18a] Was Sie über VR Performance-Guides für Unity-Projekte wissen sollten. | 3D Konfigurator 3D Animationen 3D Renderings. 2018. URL: <https://viscircle.de/was-sie ueber-vr-performance-guides-fuer-unity-projekte-wissen-sollten/>.
- [Pet17] N. Pettit. *VR Performance Guidelines for New Unity Projects*. 2017. URL: <https://blog.teamtreehouse.com/vr-performance-guidelines-new-unity-projects>.
- [GJ+10] G. Guennebaud, B. Jacob, et al. *Eigen v3: a C++ template library for linear algebra*. 2010. URL: <http://eigen.tuxfamily.org>.

---

## Bibliography

---

- [HA15] U. Haar and S. Aaltonen. "SIGGRAPH 2015: Advances in Real-Time Rendering in Games: GPU-Driven Rendering Pipelines". In: (2015), pp. 10–25. URL: [http://advances.realtimerendering.com/s2015/aaltonenhaar\\_siggraph2015\\_combined\\_final\\_footer\\_220dpi.pdf](http://advances.realtimerendering.com/s2015/aaltonenhaar_siggraph2015_combined_final_footer_220dpi.pdf).
- [Eve15a] C. Everitt. *single combined camera matrix*. 2015. URL: [https://scontent-dus1-1.xx.fbcdn.net/v/t31.0-8/11334168\\_10154006919426632\\_2185539868454578065\\_o.jpg?\\_nc\\_cat=107&\\_nc\\_ohc=QEbgUUs7xiIAx\\_q3hjC&\\_nc\\_ht=scontent-dus1-1.xx&oh=4c8cb329ef851d5ab51161943910fed9&oe=5ECFE2F1](https://scontent-dus1-1.xx.fbcdn.net/v/t31.0-8/11334168_10154006919426632_2185539868454578065_o.jpg?_nc_cat=107&_nc_ohc=QEbgUUs7xiIAx_q3hjC&_nc_ht=scontent-dus1-1.xx&oh=4c8cb329ef851d5ab51161943910fed9&oe=5ECFE2F1).
- [Whi17] N. Whiting. *Oculus Connect 4 | The Road to Shipping: Technical Postmortem for Robo Recall: Superfrustum culling*. 2017. URL: [https://www.youtube.com/watch?v=BZh0UGG45\\_o&feature=youtu.be&t=46m12s](https://www.youtube.com/watch?v=BZh0UGG45_o&feature=youtu.be&t=46m12s).
- [Odd17] V. Oddou. *VR and frustum culling - Computer Graphics Stack Exchange*. 2017. URL: <https://computergraphics.stackexchange.com/a/4765>.
- [Eve15b] C. Everitt. *asymmetric eye matrix normalization*. 2015. URL: [https://scontent-dus1-1.xx.fbcdn.net/v/t31.0-8/10460839\\_10154007978676632\\_3794989256420316318\\_o.jpg?\\_nc\\_cat=110&\\_nc\\_ohc=JuTLkrDwfTOAX\\_uUssk&\\_nc\\_ht=scontent-dus1-1.xx&oh=a3837266309d26af90584470482a1fea&oe=5EC2AD91](https://scontent-dus1-1.xx.fbcdn.net/v/t31.0-8/10460839_10154007978676632_3794989256420316318_o.jpg?_nc_cat=110&_nc_ohc=JuTLkrDwfTOAX_uUssk&_nc_ht=scontent-dus1-1.xx&oh=a3837266309d26af90584470482a1fea&oe=5EC2AD91).
- [BHP16] D. Beeler, E. Hutchins, and P. Pedriana. *Asynchronous Spacewarp | Oculus Developer Blog*. 2016. URL: <https://developer.oculus.com/blog/asynchronous-spacewarp/>.
- [18b] Steam :: SteamVR :: Introducing SteamVR Motion Smoothing. 2018. URL: <https://steamcommunity.com/games/250820/announcements/detail/1705071932992003492>.
- [Hal18] J. Hale. "Dual-Cone View Culling for Virtual Reality Applications". Bachelor's Thesis. Squareys, 10.04.2018. URL: <https://squareys.de/downloads/bachelors-thesis-dual-cone-view-culling-for-vr.pdf>.
- [Von19] V. Vondruš. *Magnum Engine*. 30.10.2019. URL: <https://magnum.graphics/>.
- [Vhi20] Vhite Rabbit. *Vhite Rabbit Website*. 8.01.2020. URL: <https://vhiterabbit.org/#about>.
- [Ove] A. Overvoorde. *Vulkan Tutorial: Introduction*. URL: [https://vulkan-tutorial.com/Drawing\\_a\\_triangle/Graphics\\_pipeline\\_basics/Introduction](https://vulkan-tutorial.com/Drawing_a_triangle/Graphics_pipeline_basics/Introduction).
- [Lin+08] E. Lindholm, J. Nickolls, S. Oberman, and J. Montrym. "NVIDIA Tesla: A Unified Graphics and Computing Architecture". In: *IEEE Micro* 28.2 (2008), pp. 39–55. ISSN: 0272-1732. DOI: 10.1109/MM.2008.31.
- [Som07] R. Sommefeldt. *AMD R600 Architecture and GPU Analysis*. 2007. URL: <https://www.beyond3d.com/content/reviews/16/5>.
- [Can16] I. Cantlay. *Pascal VR Tech*. 2016. URL: <https://developer.nvidia.com/pascal-vr-tech>.

---

## Bibliography

---

- [Smi16] R. Smith. *The NVIDIA GeForce GTX 1080 & GTX 1070 Founders Editions Review: Kicking Off the FinFET Generation.* 2016. URL: <https://www.anandtech.com/show/10325/the-nvidia-geforce-gtx-1080-and-1070-founders-edition-review/11>.
- [BS18] S. Bhonde and M. Shanmugam. *Turing Multi-View Rendering in VRWorks | NVIDIA Developer Blog.* 2018. URL: <https://devblogs.nvidia.com/turing-multi-view-rendering-vrworks/>.
- [Gal16] L. Gallagher. “Radeon Software Crimson ReLive”. In: (2016), p. 19. URL: [https://awesome.nwgat.ninja/crimson/Radeon\\_Software\\_Crimson\\_ReLive\\_%5BNDAL\\_Only\\_-\\_Confidential%5D\\_v4.pdf](https://awesome.nwgat.ninja/crimson/Radeon_Software_Crimson_ReLive_%5BNDAL_Only_-_Confidential%5D_v4.pdf).
- [Jez17] K. Jez. *GPUOpen: AMD LiquidVR MultiView Rendering in Serious Sam VR.* 2017. URL: <https://gpuopen.com/amd-liquidvr-multiview-rendering-in-serious-sam-vr/>.
- [Wil20] S. Willems. *Vulkan Hardware Database by Sascha Willems: Reports (extension feature multiview).* 2020. URL: <http://vulkan.gpuinfo.org/listreports.php?extensionfeature=multiview>.
- [Wil19] S. Willems. *Getting a Vulkan application up and running on a low-spec device with buggy drivers.* 2019. URL: <https://www.saschawillems.de/blog/2019/03/08/getting-a-vulkan-application-up-and-running-on-a-low-spec-device-with-buggy-drivers/>.
- [JMC18] JMC47. *The Current State of Dolphin on Android: Running Dolphin on Android in 2018.* 2018. URL: <https://dolphin-emu.org/blog/2018/08/14/state-of-android/>.
- [And16] W. Andermahr. *Nvidia Pascal: 21 Prozent mehr Leistung in iRacing durch SMP.* 2016. URL: <https://www.computerbase.de/2016-09/pascal-smp-iracing-benchmark/>.
- [Ser19] F. Serrano. *Multiview on WebXR.* 2019. URL: <https://blog.mozvr.com/multiview-on-webxr/>.
- [de 14] J. de Vries. *Learn OpenGL: Stencil testing.* 2014. URL: <https://learnopengl.com/index.php?p=Advanced-OpenGL/Stencil-testing>.
- [DPV17] D. Di Donato, R. Palandri, and R. Vance. *High quality mobile VR with Unreal Engine and Oculus.* 1.03.2017.
- [PG16] R. Palandri and S. Green. *Oculus Developer Blog: Hybrid Mono Rendering in UE4 and Unity.* 2016. URL: <https://developer.oculus.com/blog/hybrid-mono-rendering-in-ue4-and-unity/>.
- [16a] *Monoscopic Far Field Rendering.* 2016. URL: <https://docs.unrealengine.com/en-US/Platforms/VR/DevelopVR/MonoFarFieldRendering/index.html>.
- [Lap17] P. Lapinski. *Vulkan cookbook: Work through recipes to unlock the full potential of the next generation graphics API—Vulkan / Paweł Łapinski.* Birmingham, UK: Packt Publishing, 2017. ISBN: 9781786468154.

## Bibliography

---

- [PGP18] R. Palandri, S. Gosselin, and C. Pruett. *Oculus Developer Blog: Optimizing Oculus Go for Performance*. 2018. URL: <https://developer.oculus.com/blog/optimizing-oculus-go-for-performance/>.
- [19] *Foveated Rendering on the VIVE PRO Eye*. 2019. URL: <https://zerelight.com/news/tech/foveated-rendering-on-the-vive-pro-eye>.
- [Vla16] A. Vlachos. “GDC2016: Advanced VR Rendering Performance”. In: (2016), pp. 18–24. URL: [https://alex.vlachos.com/graphics/Alex\\_Vlachos\\_Advanced\\_VR\\_Rendering\\_Performance\\_GDC2016.pdf](https://alex.vlachos.com/graphics/Alex_Vlachos_Advanced_VR_Rendering_Performance_GDC2016.pdf).
- [Kan16] D. Kanter. *Tile-based Rasterization in Nvidia GPUs*. 2016. URL: <https://www.realworldtech.com/tile-based-rasterization-nvidia-gpus/>.
- [16b] *VRWorks - Multi-Res Shading*. 2016. URL: <https://developer.nvidia.com/vrworks/graphics/multiresshading>.
- [Ngo17] A. Ngo. *GDC 2017: Nvidia GTX 1080 Ti promises 35 percent performance boost over GTX 1080*. 2017. URL: <https://www.notebookcheck.net/Nvidia-GTX-1080-Ti-promises-35-percent-performance-boost-over-GTX-1080.199804.0.html>.
- [Cle17] S. Cleveland. “NVIDIA FCAT VR Reviewer’s Guide”. In: (2017), p. 35. URL: [https://international.download.nvidia.com/geforce-com/international/pdfs/NVIDIA\\_FCAT\\_VR\\_Reviewer’s\\_Guide\\_Public.pdf](https://international.download.nvidia.com/geforce-com/international/pdfs/NVIDIA_FCAT_VR_Reviewer’s_Guide_Public.pdf).
- [13] *NVIDIA Nsight Visual Studio Edition*. 2013. URL: <https://developer.nvidia.com/nsight-visual-studio-edition>.
- [18c] *VRWorks - Variable Rate Shading (VRS)*. 2018. URL: <https://developer.nvidia.com/vrworks/graphics/variablerateshading>.